UNIVERSITY
OF TRENTO - Italy
Department of Materials Engineering
and Industrial Technologies

Doctoral School in Materials Engineering - XXIV cycle

Numerical simulation of fumes evacuation in steelmaking plants

László Lábiscsák

Supervisors:
Prof. Giovanni Straffelini
Prof. Filippo Trivellato

April 2012

Abstract

Evacuation systems in steelmaking plants contribute to the security of the operators around the furnace and help to gain the emission levels stated in the environmental regulations, furthermore play a major role in the mass and heat balance of the factory. The aim of the dissertation is to study both primary and secondary emission capture systems of an electric arc furnace steelmaking plant by means of 3D computational thermal fluid dynamics calculations.

The overall performance of the post-combustion chamber, and consequently the primary line, is controlled by the size of the gap downstream the fourth hole of an electric are furnace. The impact of the opening coefficient (ratio between the gap area and the total area) on the post-combustion chamber performance has been investigated by means of a comprehensive 3D steady CFD simulation comprising radiative heat exchanges and detailed chemical reactions. It was found that there is not a unique value of the opening coefficient capable of optimizing all the relevant quantities of the evacuation process. A value of the opening coefficient in the range $0.40 - 0.52$ appears advisable. The impact of the (mostly unknown) boundary conditions was also assessed and inefficiencies of the assumed post-combustion geometry have been highlighted.

The secondary line's capturing efficiency during the charging phase was simulated with both transient and steady-state solvers with different turbulent models, namely the standard κ-ε and the Large Eddy Simulation models. The results revealed that steady-state simulations provide sufficient information for designing and optimizing the geometry of the secondary capture system. The simulations also pointed out several geometries, which cause significant pressure drop and ,as a result, diminish capturing ability of the canopy hood and the additional evacuation system. The boundary conditions were imposed with the help of experimental measurements in the simulated steelmaking factory.

Acknowledgments

I wish to express my gratitude to my supervisor, Professor Giovanni Straffelini. I am heartily grateful to my co-advisor, Professor Filippo Trivellato, whose expertise, wide knowledge and logical thinking have been of great value for me and provided a good basis for the present dissertation. I am grateful to Stg Group Spa for the financial support of my PhD studies.

I am grateful to all my friends who have always stood by me and my colleagues in The Metallurgical Laboratory - University of Trento who helped to make my everyday PhD life more funny.

This thesis would not have been possible without the caring support of my family and their faith in me. I owe my thanks to my loving wife and my adorable son for making every moments special and delightful.

Contents

List of Figures

List of Tables

Main notation

A	= pre-exponential factor $[mol/(1/s\,K)]$	μ_T	= turbulent dynamic viscosity $[kg/(ms)]$
A_{gap}	= gap area $[m^2]$	ν	= kinematic viscosity $[m^2/s]$
A_{inlet}	= inlet area $[m^2]$	ρ	= mass density $[kg/m^3]$
E_a	= activation energy $[cal/mol]$	φ	= conversion of chemical substances $[-]$
H_{in}	= total enthalpy of entering gases $[J/kg]$		
H_{react}	= reaction heat $[J/kg]$	CFD	= Computational Fluid Dynamics
H_{wall}	= total exchanged heat through walls $[J/kg]$	Da	= Damköhler number $[-]$
k	= reaction rate constant	DES	= Direct Evacuation System
k_{cr}	$= c_p/c_v$ $[-]$	DO	= Discrete Ordinates
$\dot{m}$	= mass flow rate $[kg/s]$	EAF	= Electric Arc Furnace
Q_{AIR}	= volume flow rate of ambient air $[m^3/s]$	ED/FR	= Eddy-Dissipation/Finite-Rate
Q_{EAF}	= volume flow rate of EAF $[m^3/s]$	EDC	= Eddy Dissipation Concept

r	= rate of reaction $[mol/(m^3 s)]$	FVM	= Finite Volume Method
T	= temperature $[K]$	GCI	= fine-grid convergence index
u_T	= friction velocity $[m/s]$	LES	= Large Eddy Simulation
Δp	$= p_{inlet} - p_{outlet}\,[Pa]$	LS	= liquid steel
		PCC	= post-combustion chamber
ε	= turbulent dissipation rate $[m^2/s^3]$	$RANS$	= Reynolds Averaged Navier Stokes
ζ	= opening coefficient $[-]$	$WSGGM$	= Weighted-Sum-of-Gray-Gas model
η	= thermal recovery $[-]$	$2D$	= 2 Dimensional
η_K	= Kolmogorov scale $[m]$	$3D$	= 3 Dimensional
κ	= turbulent kinetic energy $[m^2/s^2]$		

Chapter 1

Steelmaking by electric arc furnace

Steel has most probably the widest applicability due to its versatile nature. The variation of alloy components allows using it in wide range of every day life. Steel sector plays a dominant role in Europe's economy. The EU-27 produced the 15 % of the world's steel in 2008 [1].

The production of the steel is carried out in more process stages and can be made from either raw materials (e.g. direct reduced iron (DRI)) or recycled scrap metals. Raw materials and scrap metals contain high amount of carbon and the concentration of other elements (Si, P, S etc.) are also elevated, which is unsought in many fields of steel application. Steelmaking could be roughly defined as: removing of undesirable impurities produced in blast furnace or smelting and refining of scrap (and other forms of) iron in a melting furnace.

Steelmaking with electric arc furnace (EAF) became an extensively used method in the last forty years due to its efficiency and technical advances. In 2005, the 33 % of global steel production was melted in EAFs. This percentage is even higher in the EU, where 41.8 % of steel is produced in

EAFs.

The operation of the EAF is a batch process, which can be divided into six main stages, namely the *charging*, the *melting*, the *refining*, the *deslagging*, the *tapping* and the *furnace turnaround*. The whole operating cycle is called as *tap-to-tap* cycle.

The *tap-to-tap* cycle is initiated with the *charging* period, when the roof of the EAF is opened and the crane lifts a filled basket over the furnace. The basket is filled with scrap metal and additives (lime, dolomitic lime) for enhancing slag formation. When the operator opens the basket, the scrap and the additives fall into the furnace, which contains liquid steel (this is also called hot heel). The organic content of the scrap burns immediately and resulting fire plume that is released into the factory's ambient. The charging period may be repeated within one production cycle, depending on the furnace dimensions and the density of the scrap.

After the crane is moved away and the furnace is closed the *melting* period is started with the immersion of the graphite electrodes. The electrodes are slowly moving downwards as the solid scrap is being melted by the heat of the electric arcs. The applied voltage is lower at the beginning of the meltdown, to prevent the furnace's roof and sidewalls from electric strikes. To accelerate the melting process, new furnaces are set up with oxy-fuel burners and oxygen lances. Therefore the required energy for the melting is supplied by electrical and chemical energy as well. The oxidation of the organic and inorganic components in the scrap and the activated burners lead to high gas load inside the furnace. After the melting is accomplished a second *charging* may start.

When the amount of the molten steel meets the requirements, the *refining* period begins. This period can be roughly defined as the fine tuning of steel's component. This is achieved by the removal of carbon and further inorganic impurities, such as phosphorus, sulfur, silicon, manganese, alu-

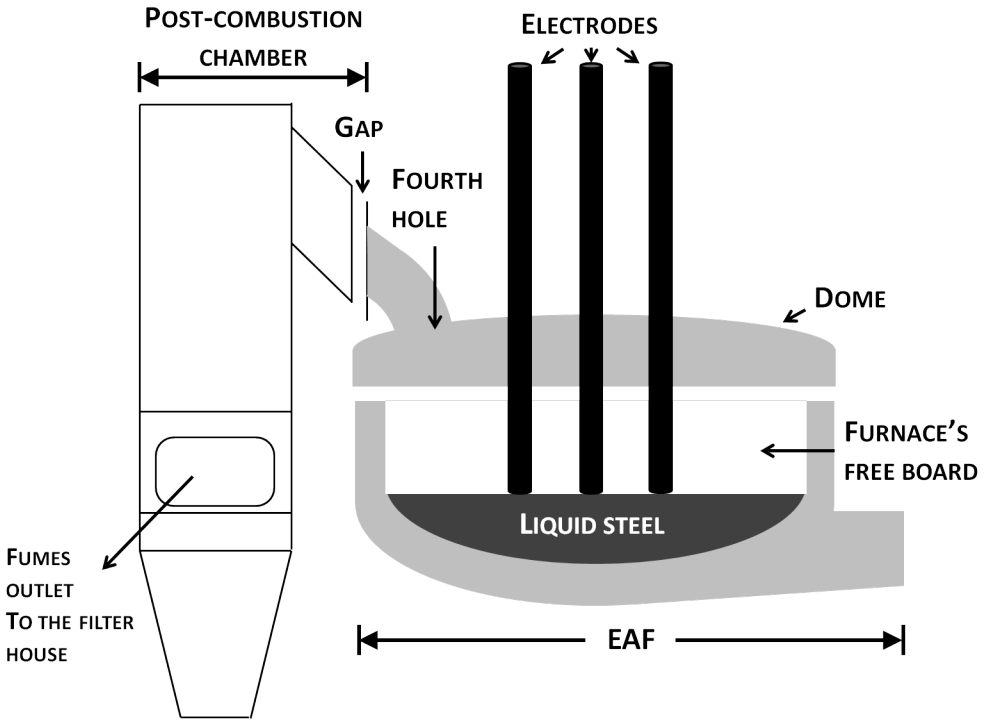

Figure 1.1: Simplified EAF geometry

minum, chromium etc. The oxidation of these elements is carried out by the oxygen lances. The oxidized elements are risen and enter the *slag* phase, which floats on the surface of the molten steel. This phase consists of the oxides of the impurities and slag former materials (CaO, MgO).

Once the impurities are removed from the steel, their separation is carried out during the *deslagging* phase, when the furnace is tilted and the slag is poured out through the slag door.

If the composition of the steel and its temperature reach the desired level, the furnace is tilted and the molten steel is poured into the preheated ladle through the tapping hole. Until the next *charging* is being started, the roof of the furnace is opened and the necessary repairs of the refractory line

and water-cooled panels are made. This period is referred as the *furnace turnaround*.
As it can be seen, during each step of the steel production gas and fume generation are always presented. To enhance the overall efficiency of the production and maintain safe working environment the capture and withdrawn of these gases are substantial. In the next section, the sources of the emissions and evacuation systems are presented in detail.

1.1 Emissions and evacuation systems

Apparently, during each phases of normal EAF operation emission of fumes and gases is presented and can be divided into *primary* and *secondary* emissions.
Primary emissions are related to the melting and refining periods and represent 95 % of total emission [2], while *secondary emissions* are those that are emitted during charging and tapping period. The escaped fumes from the EAF (from the electrode ports and from the roof ring due to the imperfect sealing) also contribute for the secondary emissions. The primary and secondary emissions contain metal particles, organic materials and the oxides of nitrogen and sulfur. The composition and the quantity highly depend on the scrap's quality [3], which cannot be strictly known.
Early EAFs were operated without any emission system. As the ambient work environment around the furnace became essential for controlling the processes, the evacuation system went through a remarkable development.
Nowadays, the most popular evacuation system (42 % of the EAF in the EU [4]) consists of fourth hole evacuation and canopy hood. The following chapters are dedicated to show the evolution of the evacuation systems for both primary and secondary emissions.

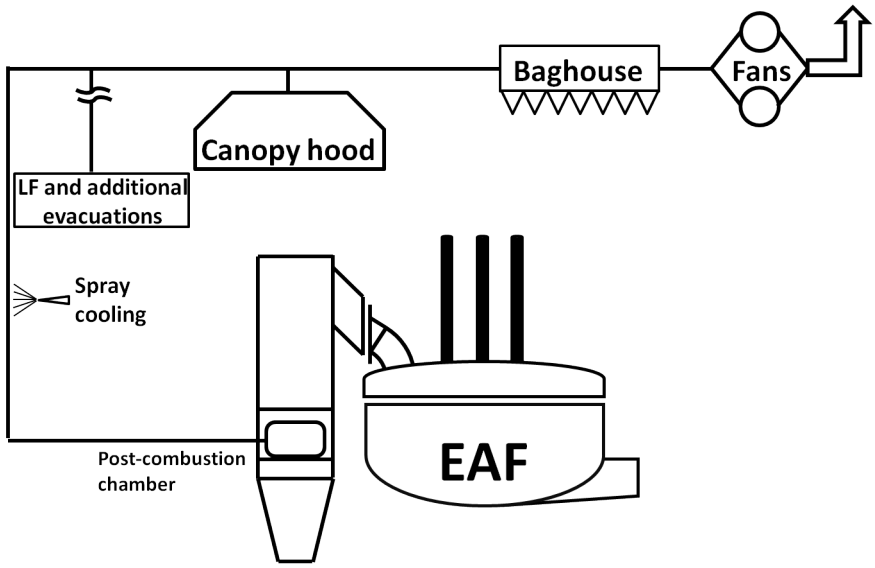

Figure 1.2: Flow sheet of the evacuation system in Electric Arc Furnace steelmaking plant.

1.1.1 Primary line

As it has been mentioned, emission control systems went through remarkable progress, which was catalyzed by the rigorous environmental regulations. Consequently, the aim of the emission control became not only to capture solid particles but also collect toxic gases and recover heat. The development was started with roof mounted type furnace hoods, which could be mounted for stationary furnace hoods. However, in case of larger diameter (>5 metres) this could not be established.

The different configurations of hood evacuation system are depicted in Figure 1.3. The side draft hood (a) collects the fume that exits on the electrodes ports and occasionally from slag door. However, it can be operated at low discharge; fumes can escape from the roof ring. This can be handled with the help of full roof type hoods (b,c) which are less expensive, however suf-

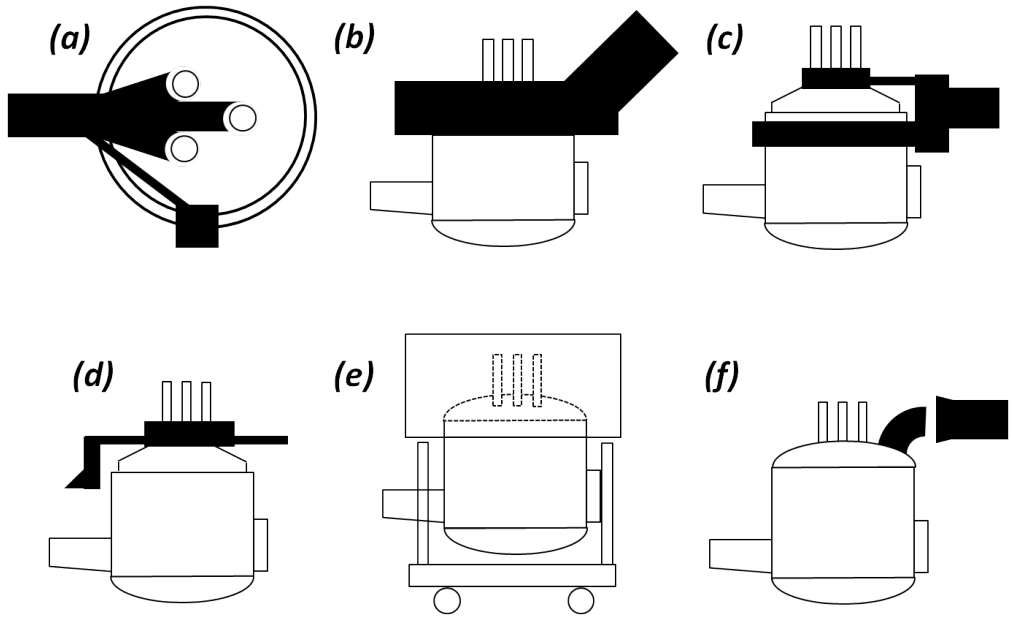

Figure 1.3: Hood configurations: (a) side draft, (b) full roof, (c) Pangborn modified full roof, (d) close fitting, (e) mobile canopy, (f) snorkel system.

fer from several disadvantages. The close fitting hood (d) provides excellent evacuation, however it makes hard to access the roof and can be applied only for small furnaces. Mobile canopy hood can be mounted in case of very small furnaces (< 10 tons capacity).

The snorkel system (f) evacuates the furnace through a water-cooled elbow, which is connected to the fourth hole that is placed on the furnace's roof. There is a gap between the snorkel and the elbow, which allows mixing ambient air into the system. The oxygen content of the air oxidizes the combustible gases.This system is also called *Direct Evacuation System* (DES) or fourth hole system and is the most commonly used configuration for modern emission control.

1.1.1.1 Direct Evacuation System

The typical DES composed by the fourth hole, post-combustion chamber (PCC), cooling apparatus, the system ducts, baghouse and the fans. The purposes of the off-gas handling are the collection of particles, the oxidation of combustible components and the cooling of the gases.
However, the 96 % of the dust particles is PM_{10}, the distribution of the particles' diameter spans three orders of magnitude [5], therefore the collection of solid particles is usually carried out in more steps. First, the larger particles are collected by sedimentation in the PCC, which forces the off-gases for abrupt change of direction. The finer particles are collected by plastic filters, which are placed in the baghouse (Figure 1.2) or by electro-static sedimentation. The main advantages of the DES are the high efficiency, the lowest off-take volume, the minimal space requirement and it also deals with the issues of CO, H_2 and VOC combustion.

1.1.1.1.1 Post-combustion chamber

In the EAF carbon monoxide and hydrogen are both presented at each step of the production, however the generation rate of these combustible gases during the melting phase is the highest, since the main source is the organic compounds of the charged material and the oxygen lances. Despite the modern oxygen injection system, oxygen deficiency occurs in the furnace [6] that inhibits the complete oxidation of carbon to carbon dioxide.
The combustion of carbon monoxide and hydrogen are highly exothermic ($\Delta H_{CO} = -283\,kJ/mol$, $\Delta H_{H2} = -286\,kJ/mol$ [7]), therefore the oxidation of these gases can enhance the overall efficiency [8]. If it was mainly burnt in the furnace free-board the heat could be recovered within the furnace which is desirable. Although the efficiency was very high (the surface of the scrap metal is high, hence the heat transfer is outstanding) the carbon

monoxide content in the exiting gases could diminish below the flammability limit and the rest could not be burnt at the combustion gap. Furthermore, if the temperature remains high, the generated carbon dioxide would dissociate to carbon monoxide and oxygen, which would form dioxins in the downstream of the off-gas system. Consequently, the carbon monoxide and dioxin content of the off-gases were high.
To solve these issues, a combustion chamber is connected to the furnace (Figure 1.1), which is followed by a water spray cooler (Figure 1.2). These devices ensure the low concentration of carbon monoxide and the low temperature of the off-gases.

1.1.2 Secondary line

Initially, rudimentary and insufficient canopy hoods captured the secondary emissions. Nowadays, modern and sophisticated systems are designed to provide sufficient discharge, which is typically four, six times larger than the discharge of the DES. The goal of the secondary evacuation system is to maintain the safety of the working ambient by capturing and withdrawing the secondary emissions efficiently. The main load arises for the secondary evacuation system during those processes, when the furnace is opened and/or the filled ladle is presented.
Information about the secondary emissions is limited but the charging definitely provides the largest load. The evacuation of the fire plume, which is generated during the charging (see section 1), calls for large discharge and high capturing efficiency. The secondary emissions contain $0.3 - 1\,kg/t$ liquid steel (LS) and $0.2 - 0.3\,kg/t$ LS solid particles during charging and tapping [2], respectively. The dust load during melting and refining is also considerable due to the leakage of fumes from the furnace and varies between $0.5\,kg/t$ LS and $2\,kg/t$ LS [9]. The exact composition and amount are hard to be evaluated, since the primary and the secondary line are always

connected and the emissions are after-treated together [10].
There are three main type of secondary capture systems. These are the *canopy hood*, the *furnace enclosure (doghouse)* and the *enclosed melt shop*.

1.1.2.1 Canopy hood

Originally, canopy hoods were mounted on the roof level for capturing primary emissions. As the productivity of the EAFs were increased, the need for collecting the secondary emissions during charging and tapping was arisen. The application of the canopy hood for this purpose is convenient, since it does not detain the operation of the furnace and the movement of the crane. The efficiency and capturing ability of the canopy hoods are highly influenced by the design of the canopy and the involved surroundings, i.e., crane and basket dimensions and positions. Errant drafts have also great impact on the capturing efficiency; i.e., the presence of cross drafts in the factory due to opened doors and natural convection generated by heat sources (filled ladle) diminishes the efficiency and capability of the canopy hood to capture the secondary emissions.
The early canopy hood designs were only capable to collect the generated fie plume during the charging at an enormous high price of discharge. Therefore, the so-called deep storage canopy hood was applied to deal with the sudden heat and fume release (Figure 1.4).

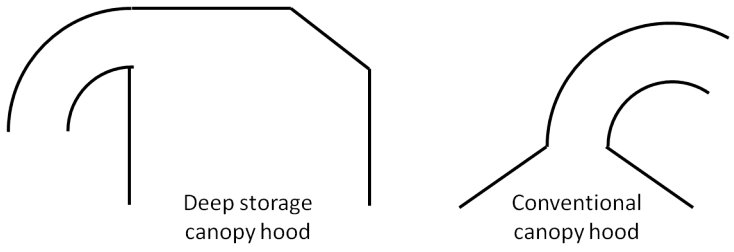

Figure 1.4: Deep storage and conventional canopy hood layouts.

The success of this design lies in the temporary storage of the fume. This type of canopy hood has five to ten times larger volume than the conventional, which gives the opportunity to store the emitted fumes temporary and the extraction time can be extended. The temporary storage gives the opportunity to apply lower discharge with higher efficiency.
The risk that arises when deep storage canopy hood is applied that the rising warm fumes' residence time is too long in the canopy hood and cool down. This leads to the recirculation of the fumes and the fine particles descend to the working area. This is usually avoided with necessarily large discharge and with deflection walls inside the canopy hood. Nowadays, 22 factories out of the 51 in the EU apply canopy hood for withdrawing secondary emissions [4].

1.1.2.2 Enclosed furnace

This type of capture system is a closed volume placed on the operating floor surrounding the EAF. It is usually referred as *doghouse* (Figure 1.5), which provides excellent fume collection. The required discharge for sufficient capture is significantly lower than used for other configurations and it can results $10 - 15\,kWh/t$ of saving [11]. Furthermore, due to the isolation of the furnace, considerable $10 - 25\,dB$ [12] reduce in noise level can be measured. Modern enclosed furnaces are also evacuated through the fourth hole.
The main disadvantages concern the accessibility of the furnace, which leads to longer charging period and lower productivity. In the EU, 9 plants apply this type of evacuation system[4].

1.1.2.3 Enclosed meltshop

The enclosed meltshop is an alternative furnace enclosure when the whole meltshop is closed and evacuated. Evidently, in this case the evacuation

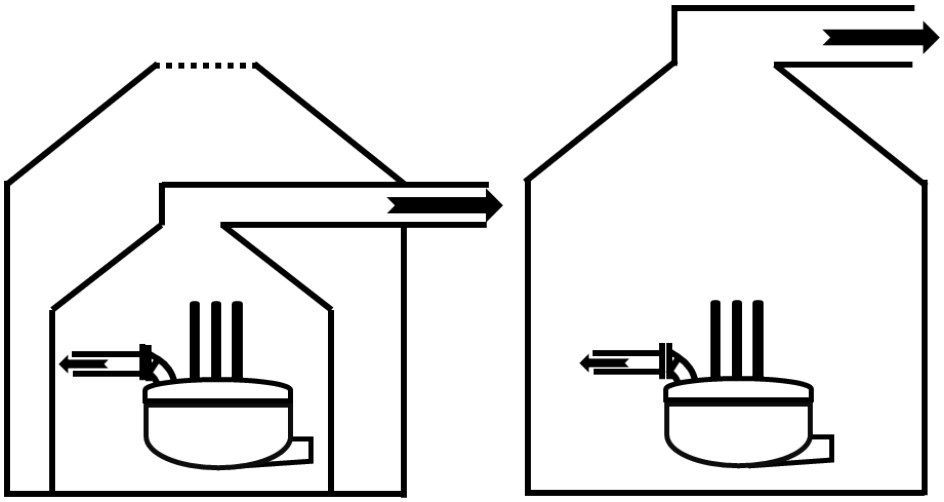

Figure 1.5: Schematic layout of the enclosed furnace (left) and the enclosed meltshop (right).

discharge must be much larger than for a canopy/DES configuration. Furthermore, the risk of inadequate extraction is the high ambient temperature and solid particles' sedimentation that makes the working conditions unacceptable. To prevent this event, the meltshop is planned to be compact sized, which gives just enough space for the EAF to be served. This resulting an isolated furnace and every other operations are separated; i.e., scrap baskets are transported into the enclosed volume by transferring trains, ladle is moved away under the furnace by a transfer car, slag is collected in slag pots which are removed using pot haulers through a dedicated doorway. In the EU, 13 EAFs are supplied by this kind of dust collection system [4] and providing improved fume control for EAF operation.

Chapter 2

Literature review

2.1 Simulation of steelmaking processes

The energy and exergy consumption of steelmaking is demanding and the amount of the emitted materials is also enormous. The iron and steel industry is the largest industrial energy consumer and the average specific energy consumption is $1.8\,GJ/t$ LS [4], which resulting the second highest cost element after employee costs. Consequently, tiny enhancement of the efficiency can benefit large energy and material savings. For this reason, steelmaking has been frequently improved and optimized. This has been done both by experimental and theoretical investigations.

Experimental investigations in the steel industry can be very expensive (because of the possible factory's outage) and hard to carry out (or even impossible) with reliable accuracy due to the harsh environment (high temperature, toxic gases etc.). However several experiments were done to enhance productivity, the spectrum of theoretical studies is very broad in many field of steelmaking.

One of the main field of simulations is to have a complete mass and heat balance of the EAF [13, 14] to predict the necessary amount of additives and

the energy requirement. The thermodynamics and kinetics of the reactions have key importance in the final compound of the molten steel. More phases are presented, therefore, to assist chemical reactions more agitating mixing is required, while the mixing is less effective compared to oxygen steelmaking [15]. Consequently, the reactions are far from equilibrium, which makes the calculations even more difficult.

There can be also found several examples for both analytical and numerical studies, which were created for studying the primary and secondary emissions and capture systems. J. H. Flux [16] presented the designing and the sizing of canopy hoods in four melting shops that are based on measurement trials and laboratory scaled experimental models. The importance of auxiliary evacuation system is highlighted by the Author. Bekker et al. [17] proposed a comprehensive predictive control of EAF off-gas release, which is based on the analytical simulation of the time dependent heat and mass balance of the electric arc furnace. Kirschen et al. [18] proposed an analytical model of the EAF dedusting system that was used to investigate the influence of the dedusting system on the EAF operation and to minimize the energy consumption. Their model's results compared favorably with their experimental measurements. Their studies were focused on the primary line and it was shown by the Authors that the maximum efficiency of post-combustion is in the range $0.5 - 2$ of the ratio of the fresh air volume (Q_{AIR}) over the hot fumes volume (Q_{EAF}); in addition, the maximum thermal efficiency was obtained at near stoichiometric combustion of the EAF hot fumes, that is $Q_{AIR}/Q_{EAF} = 1.4$ for the studied furnace.

Analytical model was proposed by Camdali et al. [19] to predict the heat loss of liquid steel in ladles by various heat transport mechanisms. The heat loss was calculated in terms of conduction, convection and radiation from the outer surfaces of an industrial ladle furnace with a capacity of $55 - 57\,t$ LS. They also proposed solutions to reduce the heat loss.

Bisio et al. [20] presented a case study about the heat transfer in an ultra high power EAF and examined the exergy and energy flows. In their studies, they pointed out the importance of the heat recovery; i.e. when the enthalpy of the slag and the cooling water was recovered the energy efficiency reached 81 %, whereas without recover it was only 73 %.

Camdali et al. (2001) [21] proposed the thermodynamic analysis of a ladle furnace. The exergy efficiency of the studied ladle was found to be 50 %.

Computational fluid dynamics (CFD) calculations are being increasingly used in the development of the steelmaking processes [22], since the capabilities of commercial codes and computers have developed dramatically and the simulation of complex fluid flows became attainable. Recently, Mazumdar and Evans [23] published a book which is dedicated to the modelling strategies in the field of steelmaking, while a chapter presents the capabilities of CFD applications in steelmaking processes.

One of the main focus of the CFD simulations in the field of steelmaking is the stirring of the molten steel in the furnace and in the ladle. Gittler et al. [22] showed a 3D liquid steel flow in a vessel in which bottom and side blowing is applied. The configurations of the nozzles were optimized and a shorter process time was achieved. In their paper the secondary evacuation system and the off-gas mixing device were also simulated by means of CFD to enhance the withdraw efficiency. The RANS turbulence models were closed by κ-ε equations (both standard and RNG) and ideal gas law was used to treat the buoyant forces, however the radiation heat transfer was neglected.

Laux et al. [24] studied the alloying process during steel tapping from EAF by CFD calculations. The results of 3D and 2D axisymmetric simulations were compared favorably. The optimization of the process was carried out and some idea was given to improve the performance of the alloying process.

Pirker and co-workers [25] simulated numerically a nitrogen stirred vessel in

3D and studied a new desulfurization technology. To enhance the reaction, which is controlled by transport mechanisms, the position of the stirring plugs and the gas flow rate were optimized.
S. T. Johansen [26] provided examples about the numerical simulations of multiphase flows in metallurgical processes. One of his interest was the bottom supersonic gas injector in ladles for metal treatment. The 2D numerical simulation is focused on the expansion of the bubbles immediately after the detachment from the nozzle, which causes refractory erosion. The gas entrainment during the tapping of steel into ladles was also simulated in 2D to evaluate the quantity of the dissolved nitrogen and the flow pattern. The Author highlighted that for more reasonable results 3D simulation is required. The tapping was also successfully simulated in a 2D manner and gave a possible solution to prevent the "blows-out" which is a potential risk for the operators.
Magneto-hydrodynamics simulation of an electro-slag remelting ladle was proposed by Kharicha et al. [27]. The effect of the imposed DC current and the mould diameter on the interface was studied and the Authors observed that the slag/steel interface is far to be flat except in special circumstances. The fluid flow and heat transfer in the tundish and mould during continuous casting has been frequently investigated in the last decade. Chattopadhyay et al. [28, 29] reviewed a variety of CFD simulation in the field of steelmaking. Different turbulence models were compared to simulate the flow field in tundish and mould. They concluded, that even though the difference between the predicted velocity fields by standard κ-ε and RNG κ-ε is vanishing, the turbulent quantities differ significantly. For simulating swirling motions, the RNG κ-ε found to be more appropriate [30]. A. Marcandalli et. al [31] proposed a numerical model to investigate the crucial parameters during continuous casting. The model is validated by experimental measurements and gives prediction about the optimal casting parameters. On the

base of this thermo-mechanical model Mapelli et al. [32] proposed a novel mould geometry to improve the heat transfer, and as a result, the quality of square cast billets is improved by a significant decrease of crack number and size.

Y. Li and R. J. Fruehan [33] was simulated the post-combustion within the furnace free board by 3D CFD calculations to get a deep insight on the process. During their simulations, the radiative heat transfer and the de-post combustion was also taken into account. In their model the de-post combustion was the gas/solid interfacial reaction between carbon dioxide and carbon ($C^s + CO_2^g = 2CO$) that always present in the liquid steel, in the scrap piles and in the electrodes. The radiation was found to be the main heat transfer mechanism. Their studies also proved, that the heat is mainly transferred to the furnace wall by radiation when flat-bath was assumed. The heat transfer efficiency was significantly improved, when low-temperature scrap pile existed on the bath's surface. Their studies also revealed that the heat transfer efficiency and the post-combustion rate were reduced by false air ingress from the slag door.

The NO_x formation within the furnace's free board was numerically simulated by Chan et al. [34]. The simulations involved the models of turbulence, radiation, combustion reactions and NO_x formation. The turbulence was modeled by standard κ-ε and the Eddy Dissipation Concept (see section 3.1.4) was applied to implement the reactions into turbulent fluid flow. The chemical model was relied on seven species and four, reduced reaction mechanisms to investigate the combustion of methane and carbon monoxide. The radiative heat transfer was estimated with the P-1 model and the absorbencies were predicted by the weighted-sum-of-gray-gases model (WSGGM). The Authors deduced, that higher exhaust flow rate leads to lower carbon monoxide content in the off-gas, meanwhile the NO_x content increases in the withdrawn off-gases.

The CFD simulation of each steelmaking processes is demanding, due to the complex nature of the presenting fluid flow. The simulated domains can rarely simplified to axisymmetric 2D models that leads to higher computational cost. The temperature differences are high, therefore buoyant flows are presented and the heat transport by radiation is also remarkable. Therefore appropriate turbulence and radiation models must be applied.

2.2 Computational Fluid Dynamics

CFD is a powerful numerical approach that is becoming widely used to simulate many processes in the field of steel and iron making. Recent progressions in the rate of the computer processors and the reduction of the costs of commercial CFD codes made the CFD as a possible technique to provide effective and efficient design solutions.
The CFD was developed from the accomplishments of the pioneers' [35, 36] efforts invested into the study of the fluid motions in order to develop numerical techniques for various fluid flows. The evolution of CFD has been so intensive that nowadays it is used as commonly as experimental and analytical modelling approaches. Moreover, CFD overshadows experimental measurements due to the high cost and time consumption to achieve fine detailed results.
The simulation of the fumes evacuation (both primary and secondary line) is thermal fluid study. 3D CFD calculation was applied, which provides the numerical solution of the Navier-Stokes equations that convey the conservation of mass, momentum and energy for both laminar and turbulent flows. For turbulent fluid flow, this can be done by direct numerical simulation (DNS), Large Eddy simulation (LES) and Reynolds-averaged Navier-Stokes simulation (RANS).

The simulation of the primary line (section 1.1.1) involves chemical reactions; i.e. the combustion of the carbon monoxide and hydrogen. The mixture of these gases are called the synthesis gas (syngas), and the simulation of its combustion has been investigated by several researchers. Due to the exothermic reactions, the temperature in the PCC is high, therefore radiative heat transfer dominates.

2.2.1 Turbulence simulation

Turbulent flows consist of eddies with wide range of length and times scales. The DNS solves the Navier-Stokes equations for the whole spectrum of turbulent scales. Although, it provides the most accurate results, its applicability is limited to the low-Reynolds number flows and simple geometry, since the computational cost growth with the Re number to the power of three over four. Consequently, engineering problems cannot be solved by DNS.
To overcome this problem, the LES approach filters the time-dependent Navier-Stokes equations, i.e. the large eddies are solved directly, meanwhile the small eddies are modeled. Unfortunately, the filtering operation introduces sub-grid scales, which are unknown quantities and require modelling to accomplish closure.
Computationally least expensive, consequently the most widely used approach for industrial problems, solution for the Navier-Stokes equations is the RANS models. These equations apply time and spatial averaging operators that also imply new unknown quantities. To obtain the closure, plenty turbulence models were developed from the simple algebraic models to the sophisticated two-equations models. The main advantage of the RANS models is the exceptionally great ratio of accuracy and CPU time in case of high-Reynolds number flows. Unfortunately, the averaging (in both time and space) poses the uncertainty for unsteady simulations, therefore it is limited for steady problems.

The fire plume, generated by the charging, is clearly turbulent and there has been many published paper about its numerical simulation. The structure of the fire, that generated during charging, can be divided into well-defined zones [37]. These are listed vertical order started form the down-most:
- the fuel itself;
- above the fuel a conical zone, which is formed by the unburned fuel vapors;
- luminous flame;
- a further combustion region, which is turbulent;
- the non-reacting buoyant plume.

Several studies [38, 39] are based on the standard κ-ε (see section 3.1.2) turbulence model or its modified version, the κ-ε-g model [40, 41].
It has been shown that standard κ-ε model overestimates the temperature in the middle of the fire plume and consequently underestimates the width of the plume [42]. There also have been researchers [43], who modified the turbulent viscosity coefficient c_t and the effective Prandtl number σ_h of the standard κ-ε, which lead to 2 % improvement. In their studies they simulated pure thermal plume, without any chemistry/combustion model involved.
The uncertainty of the standard κ-ε for simulating the fire plume is caused by one of its biggest drawback ; i.e., it assumes isotropic turbulence field and the anisotropic nature of the buoyant fire plume is clear. Therefore, several studies were also applied the LES turbulence model.
Wang et al. [44] applied the LES model to simulate pure buoyant fire plumes with heat release rates from 14 to 58 kW and compared their results to experimental data based on the measurements of McCaffrey [45]. The Authors found good agreement between the numerical and experimental results for mean temperature and velocity, flame height and entrainment rates. Strict energy conservation was also found, which shows that the model performs well for small-scale fire plumes. It is also denoted, that in case of large-scale fires the sub-grid scale kinetic energy modelling is essential for reliable pre-

diction.
Stockwell et al. [46] simulated non-premixed combustion in a regenerative furnace. Thirteen cases were employed with different models and compared the results against experimental measurements. Two κ-ε model, the standard and the RNG, and the Reynold stress model was applied for modelling turbulence. It was shown, that the different turbulence models do not influence the results significantly. In their studies, the effect of the standard and the non-equilibrium wall functions on the results were compared and found to be vanishing. The influence of different radiation models was also investigated by the Authors and will be shown in section 2.2.3.

2.2.2 Turbulent combustion in CFD

After the gained successes in the application of different turbulence models for engineering problems, the hunger to solve turbulent combustion arose, which led to several upcoming problem that must be solved. The simulation of turbulent combustion was catalyzed by the wish to use the fossil fuels more and more efficiently and environmentally acceptable.
It is well known that combustion requires the molecular mixing of fuel and oxidizer, which depends on the turbulent mixing processes. During eddy break-up process, the large eddies decompose to form smaller eddies, while the strain and shear increase thus the concentration gradients become steeper that enhances the molecular interdiffusion.
The accurate simulation of non-premixed turbulent combustion calls for the simultaneous modelling of both mixing and the relevant chemical reactions [55]. In turbulent combusting flow, the temperature, the density and the concentration of each chemical species vary spatially, furthermore the strong non-linearity of the chemical kinetics leads to inaccuracies when the reaction rates are based on mean temperature and average species concentration. The effect of turbulence on the chemical reactions is important to be known

and several approaches have been proposed for turbulence-chemistry interactions. These approaches can be divided into three main categories, namely the Probability Density Functions (PDF), the Laminar Flamelet and the Eddy Break Up based methods.

The PDF method is a statistical approach and has the great advantage, that treats the chemical source term exactly and shifts the closure problem to mixing and molecular mixing due to velocity and pressure variation. The accuracy of the PDF method highly depends on the unclosed terms [47], which can be solved computationally least expensively by pre-assumed shaped PDF's. This can be carried out by β-function or Gaussian function [48]. If the chemical equilibrium and the Lewis number is $Le_x = 1$ (Le_x=thermal diffusivity/mass diffusivity of species x)) are supposed to be valid, the thermo chemistry can be defined by a conserved scalar quantity, that is the mixture fraction. This approach gives accurate results for fast chemistry simulations with low computational cost, if the above-mentioned assumptions are satisfied.

The Laminar Flamelet approach based on the spatial analysis of the flame [49]. All the reactions within the flame are assumed to be so fast that the length scale of the reaction is smaller than the Kolmogorov scale. This assumption leads to a set of isotropic, one-dimensional laminar flame structures, which are the so-called flamelets.

The Eddy Break Up methods [50] are based on the comparison of reaction rates and turbulent mixing levels. Since the model gives fast and robust calculations, this is the most widely used model to handle chemistry-turbulence interactions. The model valid for fast chemical reactions (Da$\gg$ 1). The enhanced version of the model is the Eddy-Dissipation Concept (EDC) [51] model was developed to be able to incorporate detailed, finite rate chemistry. The model's other main advantage is that it can be both applied for premixed and non-premixed combustion systems. The inventors found good

agreement between the simulated and the experimental results.
In the literature several numerical studies can be found, which are based on the EDC model. It has been applied for hydrogen/air scram-jet combustor [52]. NO_x reduction methods were simulated [53] in coal-fired furnace successfully. Giacomazzi et al. [54] simulated a propane/air bluff body flame with single step reaction mechanism with both RANS and LES turbulence models.
The importance of detailed reaction kinetics was underlined for methane/ hydrogen/oxygen flame's simulation in stream cracking furnace [55]. The study compared the results obtained by detailed reaction mechanism implemented with EDC model and the simplified reaction kinetic implemented with Finite-Rate/Eddy Dissipation model. It was found that simplified reaction kinetic model predicts faster fuel oxidation and smaller flame volume. It was also concluded that the over estimation of the overall burning rate highly affects the temperature distribution.
Several researchers [56, 57, 58] have illustrated the mechanism of the H_2/CO mixture's oxidation; Frassoldati et al. [56] presented the detailed mechanism of 37 reactions and 12 species, and revised the relevant kinetic parameters of the formation reactions of carbon dioxide; the accuracy of the predicted final gas compounds with the applied modifications was proved successfully by experimental measurements.

2.2.3 Radiative heat transfer

The heat transfer by radiation is an electromagnetic radiation mainly in the infrared region of the light spectrum and it is a unique method of heat transfer since it does not require medium for energy transport and all the bodies, which have higher than absolute zero temperature, emit thermal radiation. The wavelength (or frequency) characterize the emitted electro-

magnetic waves. The wavelength depends on the temperature of the matter and in industrial combustion, the most important type of radiation is infrared. The intensity is also the function of the temperature and grows with the fourth power of the body's temperature, therefore it is clear that the simulation of combustion (primary line) or the presence of liquid steel (secondary line) calls for the modelling of radiative heat transport, since this heat exchange method is predominant.

Uncertainty arises in the radiation modelling due to the strong dependence on the material's properties. Four possible things can happen to radiation incident on a medium: absorption, reflection, transmission or the combination of these three. These properties mainly determine how much of the radiation is transferred to and from a medium. This is furtherly complicated by the fact that these radiative properties also vary with pressure, with temperature, with frequency, with the involved surfaces' distance and their inclinations and with the quality of the surfaces.

Several models have been employed describing radiation phenomena in CFD calculations. Each radiation models has both advantages and disadvantages that limit their application. The importance of radiation model's existence in combustion simulations has been underlined by many researchers [34, 60, 61] with the comparison of the results achieved with different radiation models against adiabatic flame. Ilbas [60] proposed a study of non-premixed hydrogen and hydro-carbon flames. The used radiation models were the P-1 and Discrete Ordinates (DO) models. The temperatures and the structures of the flames were compared to adiabatic flames. The average temperature difference between adiabatic and non-adiabatic flames was $\sim 1100\,K$, however close to the burner the difference was vanishing.

The impact of radiation models (DO, P-1 and Rosseland models) was outlined by Habibi et al. [61]. In their study, the 3D CFD simulation of a cracking furnace is performed, resulting in the supremacy of the DO model.

During our studies the DO [62] and the Rosseland [63] model was applied for the simulation of the primary line and the secondary line, respectively.
As it has been mentioned, the accuracy of the results depends not only on the radiation model but the properties of the radiating media and the surrounding walls. The radiation heat transfer analysis for industrial application is often carried out in an enclosure. In the enclosure, the presenting gas can be essentially transparent for radiation (e.g. air), which is referred as *non-participating* media, which means that the absorbency is zero. This assumption is not valid in cases, when radiatively absorbing gases (e.g. CO_2, H_2O) are presented in the medium; this is referred as *participating* media. During the combustion of fossil fuels, the gas contains considerable amount of CO_2 and H_2O, therefore the gas mixture must be treated as a participating media.
Absorbency, and consequently the emissivity, of gases (and also other matters) is not constant but is the function of the wavelength. When participating media is modelled for industrial applications, the absorbencies at each wavelengths cannot be rigorously used, since the simulation would require demanding computational efforts. Therefore narrow and wide-band methods were developed, in which the absorption lines are fused into a shape that contain several frequencies. Another possible method is the property correlation, in which the radiative properties of interest are generated and fitted with polynomial expressions that give the total property as a function of weighting factor.
Carbon dioxide and water vapor present in the combustion products in the PCC, which are known as highly selective absorbers and emitters. For the simulation of the primary line the weighted-sum-of-gray-gases model (WSGGM) was applied to handle the gas mixture's absorbencies, which assumes that only the mentioned molecules absorb (and emit) radiative heat. For the simulation of the secondary line non-participating media was as-

sumed. The simplification is valid since the participating gases' concentrations are low enough due to the dilution by nitrogen hence the factory's volume can be assumed to be non-participating to simplify the analysis.
G. Krishnamoorthy [65] proposed a novel WSGGM for $CO_2 - H_2O$ gas mixtures recently. Decoupled radiative transfer calculations were performed of a methane/air flame employing the DO method. New parameters for the WSGGM were computed from total emissivity correlations. The results were compared favorably against spectral-line-based WSGGM and existing benchmarks. Kim [66] applied finite-volume method (FVM) to investigate the heat transfer and temperature distribution of a steel slab during reheating in a continuous furnace. The absorbencies of the gas phase were predicted with the WSGGM, while parametric study was carried out on the absorbencies of furnace's inner walls and steel slab. The Author found, that even though the temperature distribution well differs within the furnace, the outlet temperature at the exit barely changes.
Stockwell et al. [46] pointed out that the difference between the results obtained with P-1 and discrete-transfer radiation model (DTRM) is negligible, however the path length of the radiation beam do affect the result significantly when non-premixed combustion is simulated in a furnace. The better match with measured data was observed when the radiation beam length was given by the cell size.
It must be also denoted that some studies revealed vanishing difference between adiabatic and non-adiabatic flames in special cases. Hewson and Kerstein [67] studied CO/H_2 flames using a RANS approach and they found that the radiation do not play a major role since the time scales for radiative heat losses are longer than the flame evolution time. Cuoci et al. [57] also found that the difference between the adiabatic and non-adiabatic flame's peak temperature is only $30 - 40\,K$.

Chapter 3

Calculations and methods

3.1 Primary line

3.1.1 Numerical method

The non linear governing equations for the conservation of mass, momentum, energy, turbulence, chemical species and radiation are solved sequentially (i.e. segregated from one another) by a control volume method.
The governing equations are implicitly discretized by a second-order upwind scheme and linearized to produce a system of equations for the dependent variables in every computational cell. The resulting linear system is a sparse coefficient matrix whose solution gives the updated flow field.
The code is based on a Gauss-Seidel solver in conjunction with an algebraic multigrid method to solve the resultant set of equations in each cell.
Since the resulting velocities in this step will not satisfy the continuity equation in local sense, the pressure correction equation (a "Poisson-type" differential equation) is solved to find suitable corrections such that mass conservation be satisfied.
Finally, the equations for turbulence, energy, chemical species and radiation

are solved using the previously updated values of the other flow variables. Appropriate under relaxation factors (0.3 for pressure, 0.7 for momentum, 0.8 for turbulent kinetic energy and turbulent dissipation rate and 1 for density, for body forces, for turbulent viscosity, for energy, for radiation variable and for each chemical species) are required to avoid instability in the solution.

3.1.2 Turbulence closure

Understanding how the gas flow turbulence affects the chemical reaction rates is one of the key issues in combustion modelling. The Eddy Dissipation Concept model [69] was used to implement the detailed kinetic mechanism into turbulent flows; this model assumes that reactions take place in regions where the highest molecular fluxes arise. Chattopadhyay et al. [28, 29] reviewed a variety of turbulence models; their review, however, is confined to tundish flows only. RANS equations have been closed in this study by a two-equation model, the standard κ-ε model. This model is often used for industrial and environmental applications due to the wide range of applicability, reasonable accuracy and low computational cost. The model comprises two equations for the turbulent kinetic energy, κ, and the turbulent dissipation energy, ε:

$$\frac{\partial}{\partial x_i}(\rho k U_i) = \frac{\partial}{\partial x_j}\left[\left(\mu + \frac{\mu_t}{\sigma_k}\right)\frac{\partial k}{\partial x_j}\right] + G_k - \rho\varepsilon - Y_M + S_k,$$

$$\frac{\partial}{\partial x_i}(\rho \varepsilon U_i) = \frac{\partial}{\partial x_j}\left[\left(\mu + \frac{\mu_t}{\sigma_\varepsilon}\right)\frac{\partial \varepsilon}{\partial x_j}\right] + c_{1\varepsilon}\frac{\varepsilon}{k}(G_k + c_{3\varepsilon}G_b) - c_{2\varepsilon}\rho\frac{\varepsilon^2}{k} + S_\varepsilon,$$

where μ_t is the gas turbulent dynamic viscosity. The term G_k describes the generation of turbulent kinetic energy due to the base flow gradients and is given by:

$$G_k = \mu_t S^2, \qquad S^2 = 2S_{ij}S_{ij} = \frac{\partial U_i}{\partial x_j}\frac{\partial U_i}{\partial x_j} + \frac{\partial^2 U_i U_j}{\partial x_i x_j},$$

where S is the modulus of the mean rate of strain tensor S_{ij}; S_k and S_ε are source terms. The constants of the κ-ε model that were used in the present study are the universally adopted values:

$$c_{1\varepsilon} = 1.44, \quad c_{2\varepsilon} = 1.92, \quad c_\mu = 0.09, \quad \sigma_k = 1.0, \quad \text{and} \quad \sigma_\varepsilon = 1.3.$$

The term Y_M stands for the contribution of compressible turbulence to the energy dissipation rate. The constant $c_{3\varepsilon}$ is calculated as: $c_{3\varepsilon} = tanh|v/u|$, where v is the velocity along the gravity direction and u is the velocity normal to v ($c_{3\varepsilon} = 0$ for buoyant layers normal to gravity; $c_{3\varepsilon} = 1$ for buoyant layers aligned with gravity).

One of the κ-ε model's main assumption is that the turbulence field is isotropic; however, the PCC has a complicated pattern of walls and the isotropy hypothesis is not fully met at the wall boundary layers. Hence the κ-ε turbulence model is valid in regions far from walls. The no-slip boundary condition for the gas velocity at the walls was applied; since velocity gradients at walls are steep, particularly in turbulent flow regime, an extremely fine mesh should be adopted in the wall region. This is, however, an unusefully complicated approach that can be avoided by assuming the logarithmic profile for the velocity near the wall.

As a result, to account for wall-bounded flows, the standard wall functions are used as boundary conditions. These functions handle the mean velocity, the turbulent kinetic energy and the turbulent dissipation rate without the need to refine the mesh close to the walls.

A wall-function boundary condition typically requires that the first cell confining with a wall must be in the log-layer, which starts at $y_+ \sim 20$ ($= yu_T/\nu$,

where u_T is the friction velocity, y is the distance to the closest wall and ν is the kinematic viscosity of the fumes) and, depending on the Reynolds number, extends up to $y_+ \sim 200$. In the log-layer, there is equilibrium between production and dissipation of the turbulent kinetic energy. Therefore the parameter y_+ calculated in every cell confining with a wall must be always greater than 20.
The standard κ-ε model assumes a high Reynolds number, which in the present simulations was always greater than 10^6.
As a matter of fact, buoyancy effects were not included in the turbulence model because our preliminary tests showed that only a small region of the PCC had a turbulence production due to buoyancy on the same order of turbulent production due to shear stresses; the net global effect is not important (anticipating the results, the ratio $Gr/Re^2 \sim 0.3$, being Gr the Grashof number).

3.1.3 Radiation model

The spatial scale of radiation is very broad; i.e. from the molecular scale to astronomical distances. For this reason, the energy balance must be fulfilled in the whole control volume instead of infinitesimal volumes. Due to this fact, integral equations must be applied instead of differential equations.
Since the DO model is particularly suitable for simulating radiative heat transfer in combustion process, it has been adopted in this work. The DO model is based on the radiative heat equation, which is here solved for a discrete number of directions and integral over the control volume:

$$\nabla \cdot (I(\vec{r}, \vec{s})\vec{s}) + aI(\vec{r}, \vec{s}) = an^2 \frac{\sigma T^4}{\pi},$$

where I is the radiation intensity; $\vec{r}$ and $\vec{s}$ are the position and direction vectors respectively; a is the absorption coefficient; n is the refractive index; σ is the Stefan-Boltzmann constant and T is the temperature.
The path length of the radiation beams was taken identical to the actual local cell size. The effect of the number of angular discretizations was also studied during our preliminary investigations. The number of directions was varied between 32 and 200; since almost no differences were found, only 32 directions were actually used.
Gas absorbencies have a significant influence on the radiative heat transfer; it is known that the radiative properties of reacting gas flows do vary with the local composition and wave length; it is also well known that the produced carbon dioxide and water vapor are highly selective absorbers and emitters. The gray gas model (which assumes constant absorption coefficient along the electromagnetic spectrum) is oversimplified and gives a poor approximation because off-gases are a mixture of reacting gases and some of them has specific absorption coefficients. In addition, the composition of the mixture changes rapidly along the PCC due to the involved chemical reactions. The weighted-sum-of-gray-gases model [65] was thus applied in this study to calculate the absorption (or emission) coefficient of the gas mixture; this model should be viewed as a trade-off between the oversimplified gray gas model and the enormously expensive full model that takes care of different gas absorption bands.
This model substitutes the non-gray gas with a finite number of gray gases and the total heat flux is obtained by summation of the gray gases after multiplication with proper weight factors.

3.1.4 Chemical models

The study of the PCC is a reactive thermal fluid dynamics study and the results are affected by the chemical reactions and the interaction of reactions

and turbulence. Therefore, at the early stage of our studies, the turbulence-chemistry interactions were implemented with two different method to assure the reliability of the chemical models; namely the Finite-Rate/Eddy-Dissipation (FR/ED) and the Eddy-Dissipation Concept (EDC) models.
The further three chemical reactions were implemented to simulate the oxidation of hydrogen and carbon monoxide:

$$(i)\ 2H_2 + O_2 \longrightarrow 2H_2O,$$

$$(ii)\ 2CO + O_2 \longrightarrow 2CO_2,$$

$$(iii)\ 2CO_2 \longrightarrow 2CO + O_2.$$

The reaction rates (r) and the constants (A, E_a) of the Arrhenius expressions ($k = Ae^{-E_a/(RT)}$) are summarized in Table 3.1.

Table 3.1: Reaction rates and rate constants of the simulated reactions. The x_i denotes the mass fraction of the $i-$th molecule.

Reaction	r	Pre-exponential factor (A)	Activation energy (E_a)
(i)	$k_1 x_{CO} x_{O_2}^{0.25}$	$2.239 \cdot 10^{12}$ [−]	$1.700 \cdot 10^{8}$ $[J/(kgmol)]$
(ii)	$k_2 x_{CO_2}$	$5.000 \cdot 10^{8}$ [−]	$1.700 \cdot 10^{8}$ $[J/(kgmol)]$
(iii)	$k_3 x_{H_2} 0.5 x_{O_2}$	$9.870 \cdot 10^{8}$ [−]	$3.100 \cdot 10^{7}$ $[J/(kgmol)]$

When FR/ED model is applied, the solver calculates the reaction rates both by Arrhenius expression (finite rate) and by the ED model. The smaller one of these two rates is used as the net reaction rate. Consequently, the solver calculates whether the reaction is kinetic or mixing controlled.
The molar rate of generation or decomposition of the i-th species for laminar flame is written as:

$$\hat{R}_{i,r} = \Gamma\left(\nu_{i,r}^{b} - \nu_{i,r}^{f}\right)\left(k_{f,r}\prod_{j=1}^{N_r}[C_{j,r}]^{\eta_{j,r}^{f}} - k_{b,r}\prod_{j=1}^{N_r}[C_{j,r}]^{\eta_{j,r}^{b}}\right),$$

where N_r is the number species in reaction r; $C_{j,r}$ is the molar concentration of each reactant and product species j in reaction r; $\eta^f_{j,r}$ is the forward rate exponent for each reactant and product species j in reaction r; $\eta^b_{j,r}$ is the backward rate exponent for each reactant and product species j in reaction r and Γ is the net third body effect on the reaction rate [68]. The forward rate constant $k_{f,r}$ is defined by the Arrhenius equation, while the backward rate constant is computed by the following expression:

$$k_{b,r} = \frac{k_{f,r}}{K_r}, \tag{3.1}$$

where K_r is the equilibrium constant for r-th reaction and defined as:

$$K_r = exp\left(\frac{\Delta S^0_r}{R} - \frac{\Delta H^0_r}{RT}\right)\left(\frac{p_{atm}}{RT}\right)^{\sum_{r=1}^{N_R}(\nu^b_{j,r}-\nu^f_{j,r})},$$

where p_{atm} is the atmospheric pressure and ΔS^0_r and ΔH^0_r are respectively the standard state entropy and standard state enthalpy, and the used thermodynamic values can be found in the Appendix, Table A.2.
In the ED model, the net rate of production is defined by the smaller one of the two following expressions:

$$r_{i,r} = \nu^f_{i,r} M_{w,i} A\rho \frac{\epsilon}{\kappa} \min\left(\frac{Y_R}{\nu^f_{R,r} M_{w,r}}\right)$$

$$r_{i,r} = \nu^f_{i,r} M_{w,i} AB\rho \frac{\epsilon}{\kappa} \frac{\sum_P Y_P}{\sum_j^N \nu^b_{j,r} M_{w,j}},$$

where Y_P is the mass fraction of product species; Y_R is the mass fraction of any reactant and A and B are empirical constants that are equal to 4.0 and 0.5, respectively [69].
The other applied approach during the studies was the EDC model, which also let us to implement the detailed kinetic mechanisms (Appendix Table

A.1) into turbulent flows. The reaction scheme consists of 37 reactions and 12 species. The reverse rate constants were calculated via the forward rates and the equilibrium constants (Equation 3.1).
The pressure dependence of the reaction was taken into account by the Troe method [70]. This approach estimates the net reaction rate by the combination of two Arrhenius rate parameters; i.e., the low-pressure limit and high-pressure limit:

$$k_{low} = A_{low} T_{low}^{\beta} e^{-E_a^{low}/(RT)},$$
$$k_{high} = A_{high} T_{high}^{\beta} e^{-E_a^{high}/(RT)}.$$

The net reaction rate is composed by the following expression:

$$k_{net} = k_{high} \left(\frac{p_r}{1 + p_r} \right) F,$$

where p_r is:

$$p_r = \frac{k_{low}[M]}{k_{high}},$$

where $[M]$ is the mass fraction of the bath gas. F is defined as:

$$log\, F = \left\{ 1 + \left[\frac{log\, p_r + c}{n - d(log\, p_r + c)} \right]^2 \right\}^{-1} log\, F_{cent},$$

where F_{cent} is given by input parameters (α, T_1, T_2 and T_3) with the following equation:

$$F_{cent} = (1 - \alpha) e^{-T/T_3} + \alpha e^{-T/T_1} + e^{-T_2/T},$$

and

$$c = -0.4 - 0.67\, log\, F_{cent}, \qquad n = 0.75 - 1.27\, log\, F_{cent}, \qquad d = 0.14.$$

The EDC model assumes that reactions take place in those regions where the highest molecular fluxes arise. These are the so-called fine scales, where the reactants are assumed to be perfectly mixed, and reactions can be simulated as in a stirred batch reactor; hence the kinetic of the reactions determines the speed of the process inside the fine-scales.
These theoretical stirred batch reactors form a cascade system. Two main parameters characterize the smallest turbulence structures: the length factor (ξ) and the time scale (τ):

$$\xi = C_\xi \left(\frac{\nu\varepsilon}{\kappa^2}\right)^{1/4}, \qquad \tau = C_\tau \left(\frac{\nu}{\varepsilon}\right)^{1/2},$$

where $C_\xi = 2.1377$ is the volume fraction constant; $C_\tau = 0.4082$ is the time scale constant.

3.1.5 Geometry

The FVM method is always begun with the creation of the simulated geometry. It also implies the simplification of the real geometry. During the simplification those objects and shapes, which do not affect the thermal fluid flow and the heat distribution, have to be eliminated. In addition, the relevant "openings" must be created, which will provide the inlet and outlet boundary conditions.
The geometry of the simulated domain (the PCC) is illustrated in (Figure 3.1). The walls of the chamber are water-cooled. The hot off-gases enter the domain through the inlet; atmospheric oxygen enters the gap and reacts instantaneously with the combustible off-gases; the chamber is then evacuated through the outlet. The size of the gap controls the ratio between the fumes discharge and the ambient air discharge.

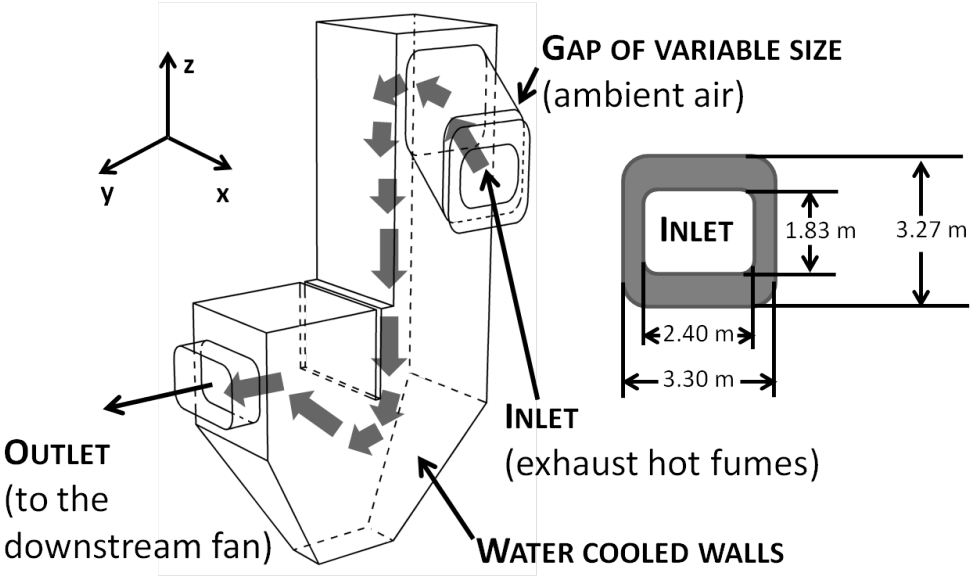

Figure 3.1: The simulated post-combustion chamber.

3.1.6 3D computational mesh

It is well known that the quality of the computational mesh is of vital importance to obtain trustworthy numerical solutions. The domain was discretized by tetrahedral elements (Figure 3.2); local refinements were carried out in regions where fast reactions occur and steep gradients of the dependent variables are expected.

Figure 3.2 shows a cross section of the 3D mesh, where the local refinement in the reaction zone and at the wall is seen: the minimum and the maximum volume of the cells varied from $10^{-7}\,m^3$ through $0.158\,m^3$. The total number of cells varied depending on the simulation and it was typically on the order $6 \cdot 10^5$, with skewness always lower than 0.85.

At the walls, the mesh was inflated to have a sufficient number of nodes lying within the viscous sublayer; the resulting $y_+ (= u_T y/\nu$ where u_T is the friction velocity; y is the distance to the closest wall and ν is the kinematic

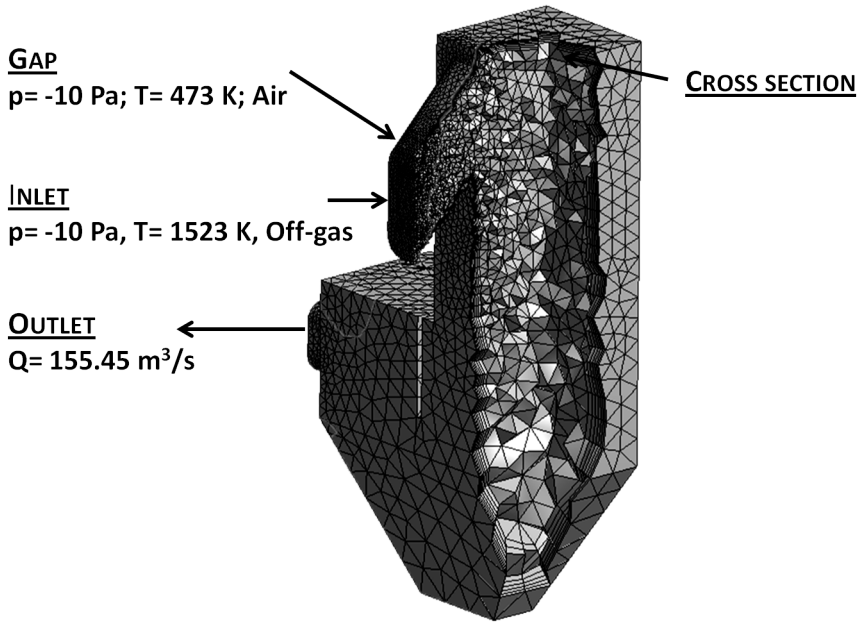

Figure 3.2: The 3D computational unstructured and conformal grid is made of tetrahedral elements; the imposed boundary conditions are also summarized.

viscosity of the fumes) is between 30 and 300, which is admittedly a bit high but not to a point to invalidate the present numerical simulation, whose accuracy will be established in section 4.1.1.

3.1.7 Boundary conditions

The results of the simulations are clearly also based on the imposed boundary conditions and therefore must be handled carefully. The evaluation of these data is not an easy task for the PCC. Accurate measurements can be barely prepared due to the harsh environment: high temperature, harmful gases and toxic fumes with metallic and non-metallic particles.
During our investigations, the data for boundary conditions were estimated

Table 3.2: Imposed boundary condition at the *inlet*.

Temperature	[K]	1523
Static pressure	[Pa]	-10
Chemical compounds	$CO\, m/m\,\%$	30
	$H_2\, m/m\,\%$	10
Turbulence intensity	$[-]$	10

from experimental data, which were provided by the Stg Group Spa and was found in the literature [17, 18], however these data cannot be handled as an actual and precise data for the studied PCC. Therefore, during the studies the effects of the boundary conditions on the results were also investigated (section 4.1).

3.1.7.1 Inlet

During the simulations, peak load was assumed which corresponds to the melting phase. During this step, the scrap metal melts down and the organic compounds burn. The exhaust fumes' temperature, chemical energy content and quantity highly depend on the quality of scrap metal, which is never exactly known and burners are also active during this phase, which also elevates the emission from the furnace and the temperature of the exiting (from the furnace) gases.
Consequently, the CO and H_2 content of the off-gases during the melting phase reaches $30\,\%$ and $10\,\%$ respectively, and the temperature reaches $1923\,K$ [22]. The applied values for the simulations are summarized in Table 3.2.

3.1.7.2 Gap

As it has been mentioned, the boundary conditions cannot be known exactly and this is particularly true for the variables on the gap's surface. Since the furnace cannot be sealed-off perfectly, the escaping fume and warm gas can reach the gap. For this reason the temperature of the air at the gap was imposed at $473\,K$ and the pressure was $-10\,Pa$. The composition of the entering gas at the gap was assumed to be pure air. The effect of these boundary conditions' alteration were also studied and are described in details in section 4.1.
The size of the gap was varied between $4\,cm$ to $50\,cm$ (the opening coefficient ζ varied between $0.13 - 0.64$).

3.1.7.3 Walls

The walls of the chamber are water-cooled and play important role in the radiative heat exchange with the warm gases. The walls are assumed to be gray-body surfaces, hence the absorption (and emissivity) is constant as a function of wavelength.
Unfortunately, it is difficult to imply the absorption of the surfaces within the PCC accurately as a design variable. It not only depends on the wall's material but it is expected to be highly altered by the contaminated particles that presents in the off-gas [59].
During the simulations, the absorption coefficient was set to 0.85 and the imposed temperature was $353\,K$.

3.1.7.4 Outlet

The PCC is evacuated through the outlet (Figure 3.2) that is connected to the secondary line system. The flow rate was set to $155.45\,m^3/s$, which

corresponds to $559620\,m^3/h$.

3.2 Secondary line

3.2.1 Numerical method

The simulation of the secondary line was carried out in both steady-state and time-dependent cases. The applied control-volume-based discretization of the governing equations for the steady-state simulation was the same as in case of the primary line's simulation (section 3.1.1).
For transient simulations, the governing equations must be discretized in both space and time. The spatial discretization is equal to the steady-state discretization method while the temporal discretization is the integral of each term in the governing equations over the time Δt. Any spatially discretized governing equation was calculated for the next time level implicitly with the following expression:

$$\frac{\phi^{n+1} - \phi^n}{\Delta t} = F(\phi^{n+1}),$$

where ϕ is a scalar quantity; $n+1$ is the value at the next time level; n is the value at the current time; Δt is the time step and F is any spatial discretization.
The main advantage of the fully implicit scheme is that the calculation is stable at any time step size.

3.2.2 Turbulence closure

The secondary line was simulated in both transient and steady cases. For transient case, the turbulence was both simulated with the standard κ-ε (section 3.1.2) and the LES models, while for steady simulations the standard κ-ε was applied.

As it has been mentioned (section 2.2.1) the LES filters the Navier-Stokes equation with a low-pass filter and the filtering variable is defined as:

$$\bar{\phi}(x) = \int_D \phi(x')G(x,x')dx',$$

where D is the fluid domain and G is the filter function which specifies the scale of the resolved eddies. The FVM implicitly provides the filtering by the volumes of the computational cells:

$$\bar{\phi}(x) = \frac{1}{V}\int_\nu \phi(x')dx', \qquad x' \in \nu,$$

where V is the volume of the computational cell. Therefore the filter function $G(x,x')$ becomes:

$$G(x,x') = \begin{cases} 1/V, & x' \in \nu \\ 0, & x' \text{ otherwise.} \end{cases}$$

The Favre-filtered equation for compressible flows is:

$$\frac{\partial \bar{\rho}\tilde{u}_i}{\partial t} + \frac{\partial \bar{\rho}\tilde{u}_i\tilde{u}_j}{\partial x_j} + \frac{\partial \bar{p}}{\partial x_i} - \frac{\partial \bar{\sigma}_{ij}}{\partial x_j} = -\frac{\partial \bar{\rho}\tau^r_{ij}}{\partial x_j} + \frac{\partial}{\partial x_j}\left(\bar{\sigma}_{ij} - \tilde{\sigma}_{ij}\right),$$

where τ^r_{ij} is the subgrid-scale stress tensor for Favre-filtered momentum field and σ_{ij} is the shear stress tensor.
Subgrid-scale turbulent stress is calculated employing the Boussinesq hypothesis:

$$\tau_{ij} = -\bar{\rho}\widetilde{u_i u}_j + \bar{\rho}\tilde{u}_i\tilde{u}_j = 2\mu_t\tilde{S}_{ij} - \frac{1}{2}\bar{\rho}q_2\sigma_{ij},$$

where $1/2\bar{\rho}q^2$ is the subgrid scale kinetic energy and,

$$\tilde{S}_{ij} = \frac{1}{2}\left(\tilde{u}_{i,j} + \tilde{u}_{j,i}\right) - \frac{1}{3}\sigma_{ij}\tilde{u}_{k,k}.$$

In the present study, the turbulent viscosity is given by the Smagorinsky-Lilly model:

$$\mu_t = \rho L_s^2 |\bar{S}|, \quad \text{where} \quad |\bar{S}| = \sqrt{\tilde{S}_{ij}\tilde{S}_{ij}}.$$

and L_s is the mixing length of subgrid scales and defined as:

$$L_s = min\Big(Kd, c_s V^{1/3}\Big),$$

where K is the Kármán constant; d is the distance to the closest wall and c_s is the Smagorinsky constant (0.1).

3.2.3 Radiation

In a non-scattering, semi-transparent media, the radiative transfer equation (RTE) can be written as:

$$\frac{dI(\vec{r},\vec{s})}{ds} + aI(\vec{r},\vec{s}) = an^2\frac{\sigma T^4}{\pi},$$

where $\vec{r}$ is the position; $\vec{s}$ is the direction; s is the length scale; a is the absorption coefficient; n is the refractive index, I is the intensity; σ is the Stefan-Boltzmann constant and T is the gas temperature.
In the elephant house the optical thickness is greater than 3, therefore the Rosseland [63] radiation model can be applied. The radiative heat flux vector ($\vec{q_r}$) in the gray medium is written as in the P-1 radiation model:

$$\vec{q_r} = -(1/3a)\nabla G,$$

where G is the incident radiation.
The Rosseland approach assumes that the intensity is equal to the black-body intensity and therefore the incident radiation becomes:

$$G = 4\sigma n^2 T^4.$$

At the end, the radiative heat flux is:

$$q_r = -16\sigma\Gamma n^2 T^3 \nabla T,$$

which is similar to the Fourier conduction law. For this reason, the Rosseland model is also known as *diffusion approximation*.
The air inside the factory was assumed to be non-participating media, hence the absorbency and scattering were both 0. The radiative heat flux at the walls ($q_{r,w}$) were defined by the slip coefficient:

$$q_{r,w} = -\frac{\sigma\left(T_w^4 - T_g^4\right)}{\psi},$$

where T_w is the wall temperature; T_g is the gas temperature and ψ is the slip coefficient. In the present study, the slip coefficient was calculated by the following [64] fitted curve:

$$\psi = \begin{cases} 1/2, & N_w < 0.01 \\ \frac{2x^3+3x^2-12x+7}{54}, & 0.01 \leq N_w \leq 10 \\ 0, & N_w > 10, \end{cases}$$

where $x = log_{10} N_w$ and N_w is the conduction to radiation parameter at the wall, and defined as:

$$N_w = \frac{k(a+\sigma_s)}{4\sigma T_w^3}.$$

3.2.4 Geometry

The large volume of the factory calls for the simplification of the geometry and the reduction of the volume. The simplifications were carried out in

two steps. During the preliminary studies, the stagnate and irrelevant zones were found and dismissed in further simulations, nevertheless new openings were also imposed. These simplifications let us reduce the number of the computational elements, which was the bottle neck of the numerical simulation.

In Figure 3.3 the simplified geometry for the first calculations can be seen. The position of the basket and the crane represents the charging phase, which is the most crucial phase of the steel production in the evacuation point of view (see section 1.1.2).

Above the crane, the deep storage canopy hood can be seen. It is divided into three sections and each section is evacuated. The size of the outlet openings are $5\,m \times 5\,m$ in the lateral sections and $5\,m \times 6\,m$ in the central section. The canopy hood contains a deflection wall (Figure 3.5) to avoid the recirculation of the rising hot fumes (section 1.1.2.1).

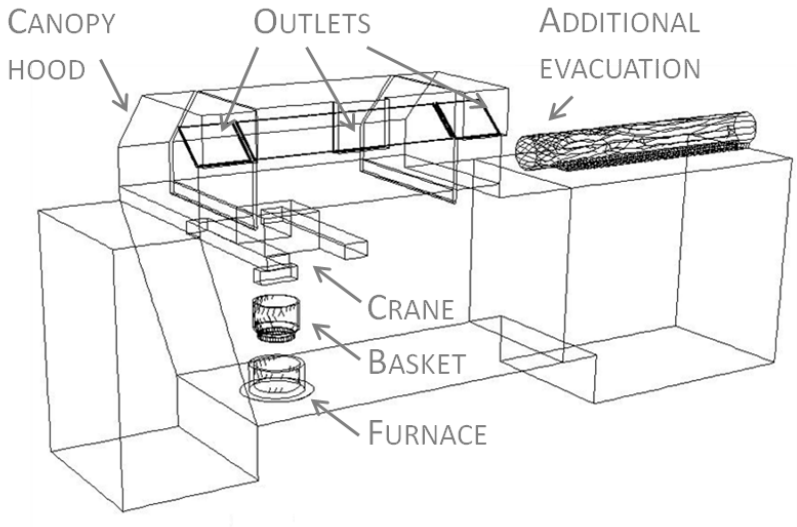

Figure 3.3: 3D structure of the simulated domain (ladle is not presented).

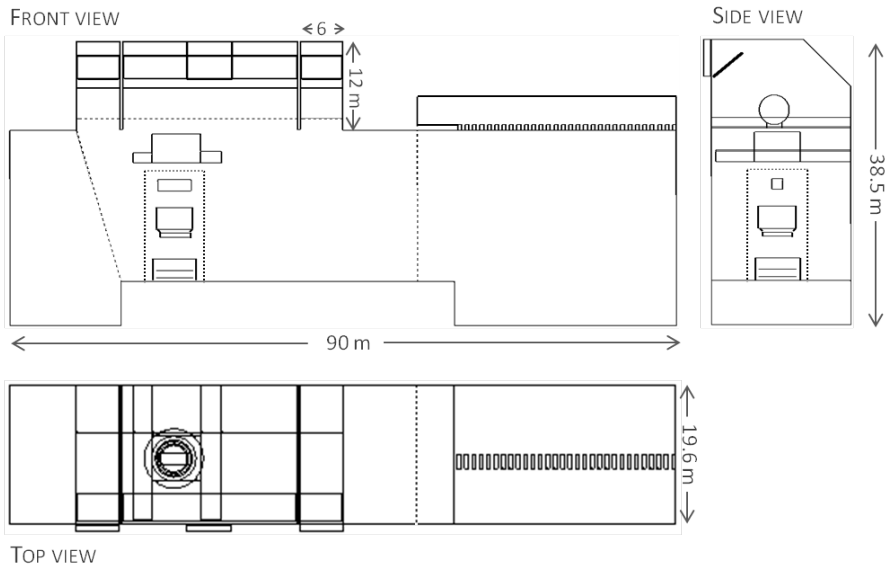

Figure 3.4: Layout of the simplified factory geometry. Dotted lines denote the volume boundaries with different mesh morphology (section 3.2.5).

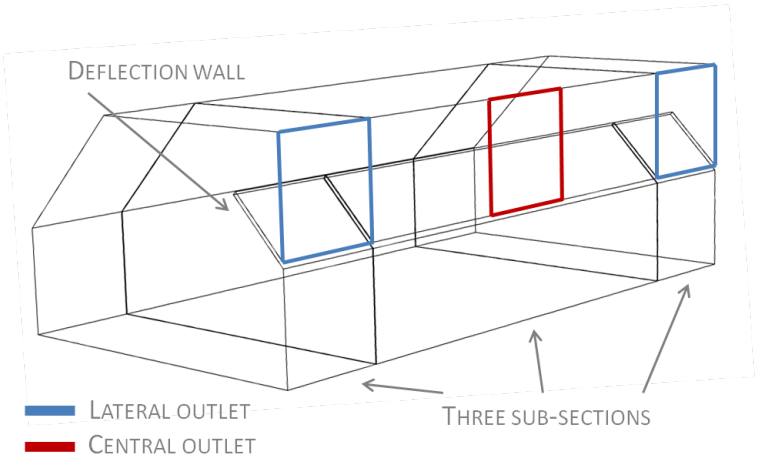

Figure 3.5: 3D layout of the deep storage canopy hood of the simulated factory.

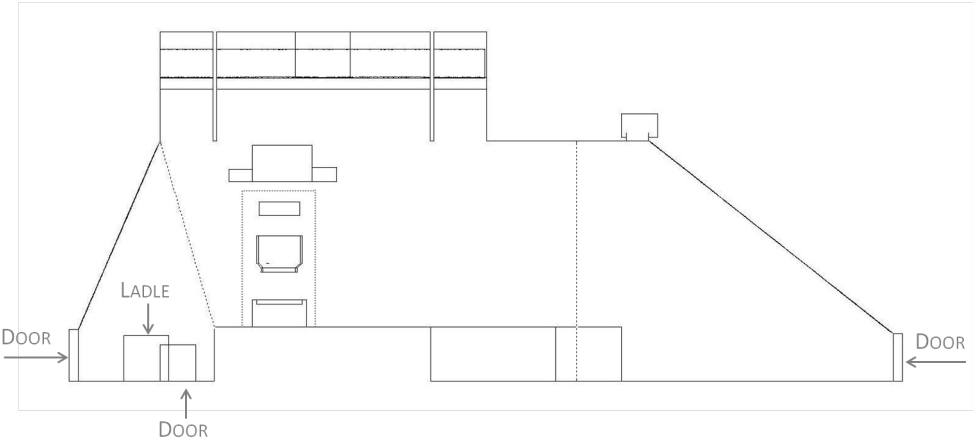

Figure 3.6: Simplified layout of the factory geometry. Dotted lines denote the volume boundaries. Each volume contains meshes with different sizes and specifications (section 3.2.5).

After the first simulations and observations in the factory, further simplifications and modifications were carried out (Figure 3.6). One of the main simplifications was to simulate the doors and windows of the factory. However, these openings supposed to be closed during production to reduce the harmful effect of wind drafts on the collection, in reality they are remained open. Consequently, cross ventilation and side flows appear in the factory which influence the fluid motions.

Another major modification concerned the additional evacuation system. The simulations revealed that only the first part of the system works and the region below the non-functioning part is a stagnate zone (see section 4.2.1).

Further modifications were imposed on the boundary conditions of the canopy hood; i.e. tubes that connects the canopy's outlets and the additional evacuation's outlet was simulated (Figure 3.7, 3.8) and the results of these simulations were then implemented as the canopy hood's boundary conditions.

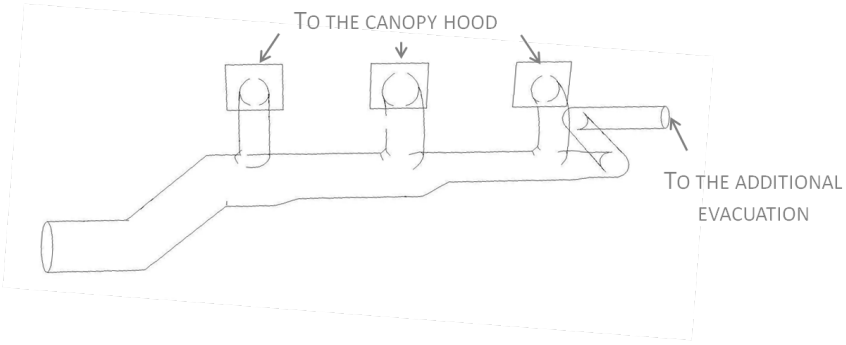

Figure 3.7: 3D layout of the evacuation tube system.

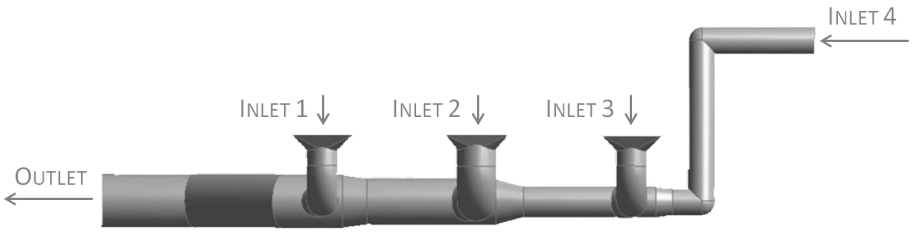

Figure 3.8: Outer tube system.

3.2.5 Computational mesh

After the geometry is created the domain was discretized by small elements, which gives the computational mesh. All the computational meshes, applied in the studies, contain tetrahedral elements.

During the mesh generation the expected flows and gradients must be taken into account. Therefore the size of the elements and the growth rates vary in a wide range in the factory. The factory was divided into smaller sections which allowed great variation of the mesh configuration. Different colors represent the separated volumes (Figure 3.9).

The separated conformal meshes were linked together through their inter-

faces. The size of the elements on the linking surfaces was the same to reduce computational errors. The relevant parameters of the generated meshes can be seen in Table 3.3.
The simulation of the natural flow generated by the liquid steel requires refined mesh close to the ladle that significantly raises the number of elements (Table 3.4).

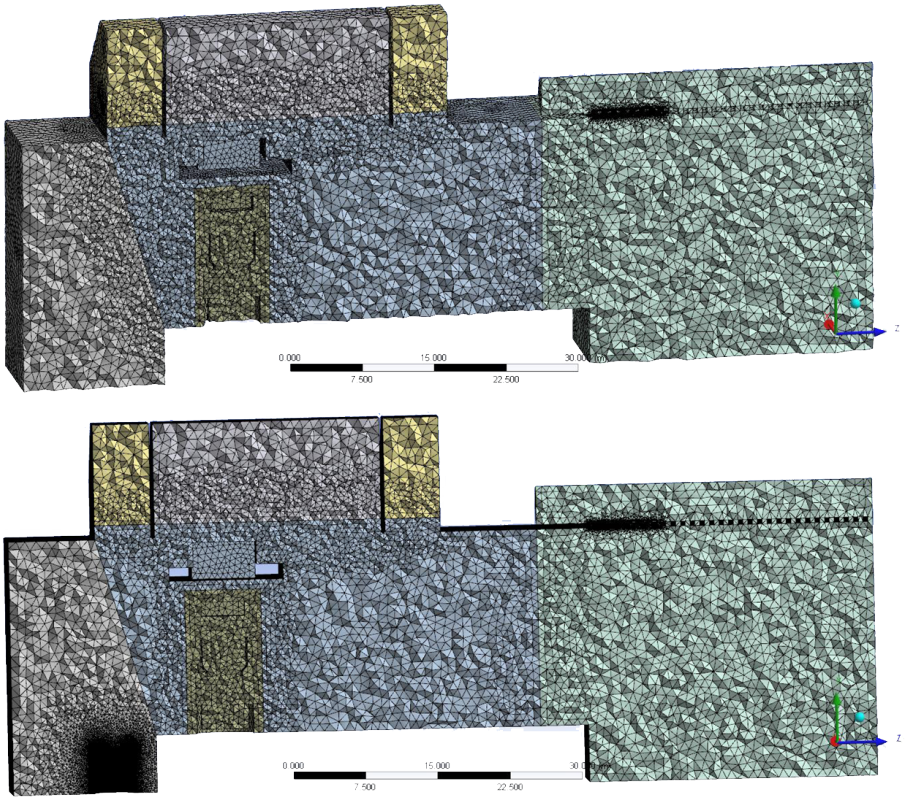

Figure 3.9: Cross sections of the computational meshes without (upper) and with ladle (bottom) presented. The different colors denote different volumes and meshes.

Table 3.3: Specifications of the computational mesh.

Surface	Minimum size [cm]	Growth rate
Furnace	20	1.4
Crane	20	1.4
Ladle	8	1.1
Deflection wall	8	1.6
Canopy hood separators	10	1.6
Additional evacuation	10	1.8

Table 3.4: Number of elements.

Configuration	Number of elements
Without ladle	1966204
With ladle	2810929

The observations in the factory let us reduce the number of elements: there is a large space in the middle of the factory, where the gases' motion is slow and gradients are vanishing, therefore coarser mesh can be constructed in this zone (Figure 3.10).
After the modifications, the number of elements was reduced to 702203 (less than the half compare to the first trial) due to the reduced volume and the coarser mesh.

Table 3.5: Specifications of the computational mesh.

Surface	Minimum size [cm]	Growth rate
Furnace and crane	30	1.2
Doors	50	1.2
Ladle (upper surface)	30	1.1
Ladle (lateral surface)	50	1.6
Deflection wall	30	1.4
Canopy hood separators	30	2
Additional evacuation	25	1.2
Canopy hood's outlets	50	1.5

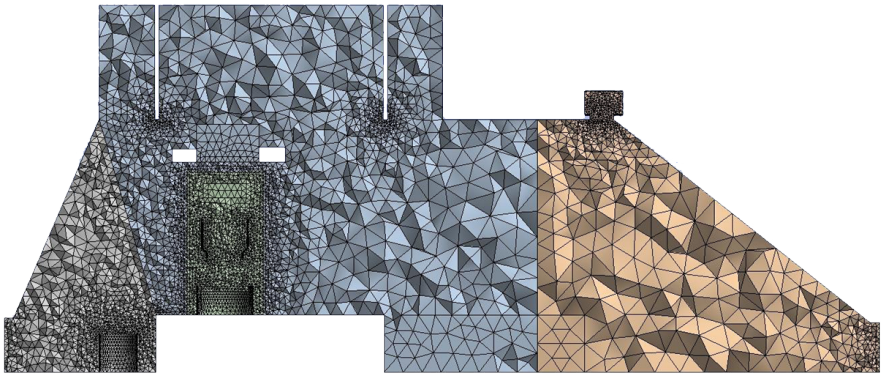

Figure 3.10: Cross section of the computational mesh generated in the modified geometry.

The generated computational mesh for the outer tubes also consists of tetrahedral elements (Figure 3.11). The mesh requires extra care close to the walls to have sufficient number of nodes that lies within the viscous sublayer (Figure 3.12). With the help of the refined mesh y_+ is in the order of 1. The total number of elements is 222835. Further grid specifications are summarized in Table 3.6.

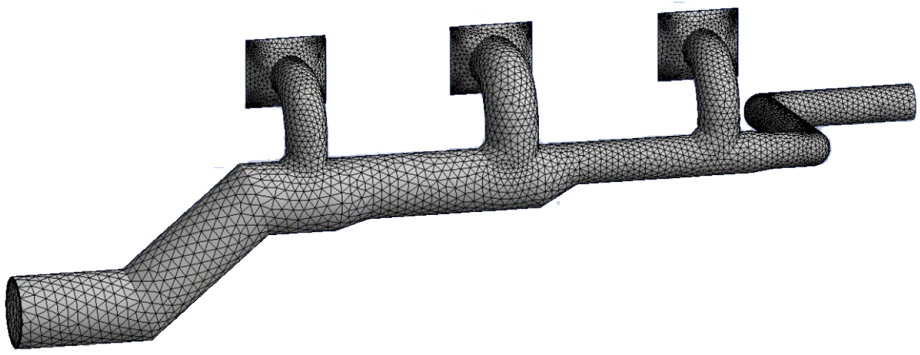

Figure 3.11: The generated computational mesh for the outer tube system.

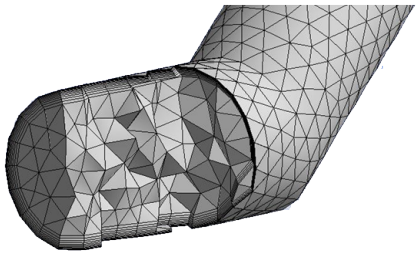

Figure 3.12: Inflated mesh close the the wall that provides sufficient number of nodes in the wall region.

Table 3.6: Specifications of the computational mesh of the outer tubes.

Geometry	Meshing control	Applied values
Walls	Inflation	Maximum thickness= $0.5\,m$
		Number of layers= 10
		Growth rate= 1.2
Internal volume	Body size function	Maximum size= $0.5\,m$
		Growth rate= 1.2

3.2.6 Boundary conditions

3.2.6.1 Preliminary study

During the first simulations, the boundary conditions were set up according to the provided data by the Stg company. In early stages, the simulations had to rely on these data, since the factory was under construction and measurements could not be carried out.

Due to the provided data the outlet velocity for the central section of the canopy hood was set to $16.8\,m/s$ and for the lateral sections $8.4\,m/s$ was used.

The generated heat by charging was assumed to be $97.5\,MW$. This value is based on the Stg company's experiences. However it cannot be strictly

known, since the organic compound is not well defined and it varies from basket to basket. The reactions are not included in our simulations, pure air was assumed. This assumption is valid, since the main interest (the capturing ability of the canopy hood) is far from the reacting zone [71]. Furthermore, this simplification significantly reduces the computational time.
The estimated temperature of the fire can be found in the literature for organic materials [72]. Since the organic amount and compound of the scrap metal vary, an average value was chosen $T = 920\,K$. The charging was assumed to be $20\,s$ long, therefore the mass-flow rate became $\dot{m} = 140\,kg/s$.
The heat loss of the filled ladle was predicted by the analytical model proposed by Camdali et al. [19]. Their model provides the analytical solution about the distribution of the exchanged heat by different heat transfer mechanisms. The calculated values for the simulated ladle can be seen in Figure 3.13.

Due to the calculations, the ladle releases heat mainly via the top (liquid steel surface) by radiation. The calculated heat and the area of the ladle's surfaces (top and lateral wall) define the imposed boundary conditions for

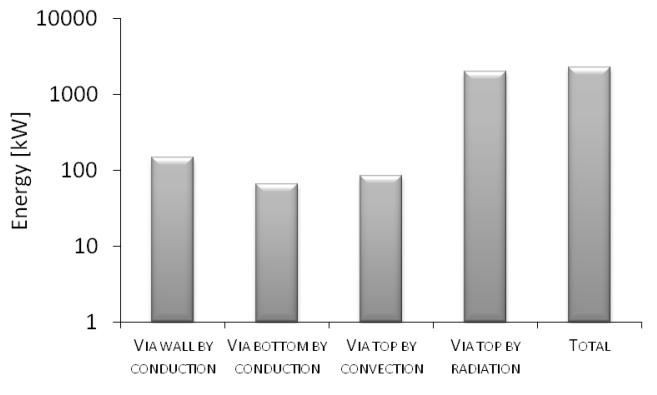

Figure 3.13: Distribution of the exchanged heat from filled ladle by various mechanisms. The total heat loss is $2.299\,MW$.

the ladle that are $50000\,W/m^2$ and $12500\,W/m^2$ for the top and side wall, respectively.

3.2.6.2 Case study

After the observations and measurements in the factory not only the geometry but also the boundary conditions were modified.
In the outer tube system the flow rate was determined by the help of a Pitot tube, which was connected to a differential pressure gage (Magnehelic Gage Dwyer Instruments Inc.) The dynamic pressure was measured in six position along the main tube's intersection to determine the velocity profile (Figure 3.14).
The measurements were carried out during the charging phase, when the applied fan power and flow rate in the tube was the maximum. This period let us carry out two measurement sequences.

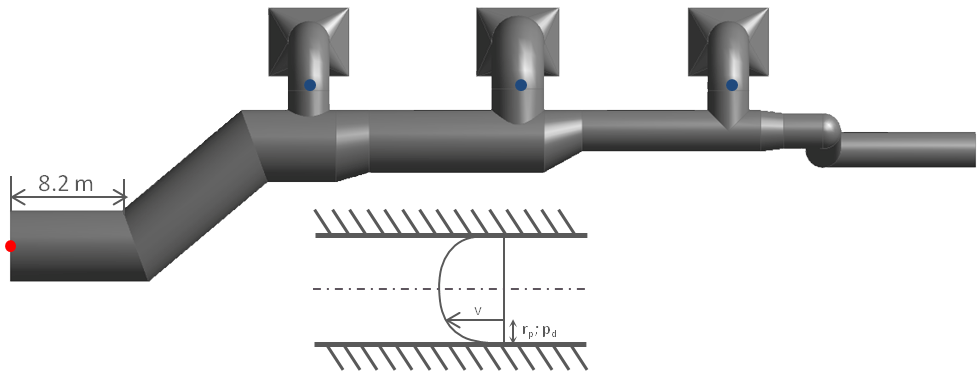

Figure 3.14: Pressure and temperature measurement points in the main tube. The red point denotes where dynamic pressure and temperature were measured and blue points denot where static pressure and temperature were measured.

Table 3.7: Measured dynamic pressure along the main tube's section on 05.08.2010.

Distance from the wall [mm]	Dynamic pressure (1) [mmH_2O]	Dynamic pressure (2) [mmH_2O]
0	3	5
250	5	8
500	7	8
750	8	10
1000	8	9
1250	8	10

From the dynamic pressure, the velocity can be calculated with the following expression:

$$v = \sqrt{\frac{2p_d}{\rho}},$$

where v is the gas velocity; p_d is the dynamic pressure and ρ is the density of the fluid.
The measured temperature was $120\,°C$, hence the used density for the calculations was $\rho = 0.898\,kg/m^3$.

The average velocities in the main tube became $12.62\,m/s$ and $14.2\,m/s$ for the first and second measurements, respectively. From the average velocities and the area of the tube's cross section ($5.2\,m$), the volume flow rate can be

Table 3.8: Calculated velocities along the main tube's section.

Distance from the wall [mm]	Gas velocity (1) [m/s]	Gas velocity (2) [m/s]
0	8.08	10.45
250	10.36	13.22
500	12.37	13.22
750	13.22	14.78
1000	13.22	14.02
1250	13.21	14.78

Table 3.9: The measured temperature and static pressure values in the collateral tubes.

Tube	Static pressure [Pa]	Temperature [K]
Inlet1	19.62	418
Inlet2	−58.86	479
Inlet3	39.24	423

calculated: $Q_1 = 965022\,m^3/h$ and $Q_2 = 1085644\,m^3/h$. These values are in a good agreement with the value, measured by the installed flow meter in the baghouse.

Due to the new openings (doors) further boundary conditions were required. These data were based on experimental measurements in the factory. The measurements were carried out with a commercial vane thermo-anemometer (Dwyer Model 8901) on 05.08.2010. The measured values are summarized in Table 3.10. However these measured data cannot be handled as precise, exact values they are still a good indicator of the main flow's velocities and directions. Negative values denote exiting flow from the factory.

Table 3.10: Boundary conditions after the measurements on 05.08.2010 in the factory and the simulation of the outer tubes of the evacuation system (section 4.2.2), where *vel. inlet* denotes velocity inlet and *m. f. inlet* denotes mass flow inlet.

Surface	Flux	Velocity	Temperature	Material
Door_{east} (vel. inlet)		$-0.9\,m/s$	$297\,K$	Air
Door_{north} (vel. inlet)		$1.75\,m/s$	$294.1\,K$	Air
Door_{south} (vel. inlet)		$1.08\,m/s$	$296.3\,K$	Air
Door_{west} (vel. inlet)		$1.23\,m/s$	$296.6\,K$	Air
Furnace (m. f. inlet)	$140\,kg/s$		$920\,K$	Air
Inlet_1 (vel. inlet)		$-3.96\,m/s$	$418\,K$	Air
Inlet_2 (vel. inlet)		$-1.71\,m/s$	$478\,K$	Air
Inlet_3 (vel. inlet)		$-3.37\,m/s$	$423\,K$	Air
Canopy hood (wall)			$480\,K$	Steel
Ladle's wall (wall)	$12500\,W/m^2$			Steel
Ladle's top (wall)	$50000\,W/m^2$			Steel

Chapter 4

Results and discussion

4.1 Primary line

4.1.1 Numerical accuracy

The procedure herein followed to estimate the numerical errors, generated by the present simulation, is strictly based on the valuable ASME guideline [73]. The underlying perspective here is to understand whether the present numerical study is capable of predicting with trustworthy accuracy the outcome of reacting flows' numerical simulations when the measure of experimental quantities is not an easy task, as in the present case.
The method here followed for the evaluation of discretization errors is the Grid Convergence Index (GCI). The first step of the procedure is the definition of the representative grid size h:

$$h = \left[\frac{1}{N} \sum_{i=1}^{N} \Delta V_i \right]^{1/3},$$

where ΔV_i is the i-th cell volume and N is the total number of cells used for the computations. Three significantly different grids were constructured,

where the grid refinement factor $r = h_{coarse}/h_{fine}$ was always greater than 1.3 (a value based on experience [73]). Roughly similar cells were always used. The apparent order p of the method was calculated by the following expression:

$$p = \Big| \ln \mid \theta_{32}/\theta_{21} \mid + q(p) \Big| \ / \ \ln(r_{21}), \tag{4.1}$$

$$q(p) = \ln\Big(\frac{r_{21}^p - s}{r_{32}^p - s}\Big),$$

$$s = 1 \cdot \text{sgn}\ (\varepsilon_{32}/\varepsilon_{21}),$$

where $h_1 < h_2 < h_3$, $r_{21} = h_2/h_1$, $r_{32} = h_3/h_2$, $\theta_{32} = \phi_3 - \phi_2$, $\theta_{21} = \phi_2 - \phi_1$, ϕ_k stands for any dependent variable derived by means of the k-th grid ($k = 1, 2, 3$); in this study, the function ϕ has been chosen the outlet temperature (the key variable here); *sgn* is the function *signum*. The absolute value in equation (4.1) is necessary to ensure extrapolation toward $h = 0$ [74].
Negative values of the ratio θ_{32}/θ_{21} were found in the present simulations; this is an indication of oscillatory convergence, which typically occurs in case of geometrically complicated fluid domains; however, the maximum oscillation proved vanishing ($\sim 1\,\%$).
A fair agreement was observed between the apparent order of the scheme and the formal order actually used: this is an indication of grids being in the asymptotic range. The extrapolated values ϕ_{ext}^{21} were then calculated along with the relative error e_a^{21}:

$$\phi_{ext}^{21} = \frac{r_{21}^p \phi_1 - \phi_2}{r_{21}^p - 1},$$

$$e_a^{21} = \Big| \frac{\phi_1 - \phi_2}{\phi_1} \Big|.$$

The fine–grid convergence index GCI_{fine}^{21} is given by:

$$GCI^{21}_{fine} = \frac{1.25e^{21}_a}{r^p_{21} - 1}.$$

The local order of accuracy p calculated from equation (4.1) was between 9.3 and 21.5, with an average value $p_{ave} = 12.9$.
The convergence (or iteration) error occurs when the iterative solvers of the discretized equations are not converged sufficiently; following [75], the iteration error was estimated by:

$$\epsilon^n_{iter,i} \sim \frac{\phi^{n+1}_i - \phi^n_i}{\lambda_i - 1},$$

where n is the iteration number and λ_i is the principal eigenvalue of the solution matrix of the linear system, which can be approximated as:

$$\lambda_i \sim \frac{\parallel \phi^{n+1}_i - \phi^n_i \parallel}{\parallel \phi^n_i - \phi^{n-1}_i \parallel},$$

where $\parallel \cdot \parallel$ is any appropriate norm (e.g., the infinity norm L_∞). The uncertainty δ_{iter} in iteration convergence can then be estimated as:

$$\delta_{iter} \sim \frac{\parallel \epsilon^n_{iter,i} \parallel}{\lambda_{ave} - 1},$$

where λ_{ave} is the average value of λ_i over a reasonable number of iterations. The iteration error calculated according to the above described method was found to be one order of magnitude smaller than the discretization error; so there are reasons to trust the accuracy of the present numerical simulation.

4.1.2 On the simulation of the chemistry-turbulence interaction

At the first stage of the PCC simulation, different models for turbulence-chemistry interaction were tested with simplified chemical reaction mechanism to access the accuracy of ED/FR and EDC models. Applying the EDC model convergence was reached effortless, while during ED/FR calculations, instability occurred, which lead to the divergence of the solution. Reduced under-relaxation factors did not result in success for reaching converged solution.

The EDC model was both applied for implementing simplified, 3 steps skeleton reactions and detailed mechanism involving 37 reactions (Table A.1) in case of $30\,cm$ gap size ($\zeta = 0.52$). However the estimated hydrogen conversions do not show significant difference, the conversion of the carbon monoxide differs with a noticeable $3.5\,\%$ and the carbon monoxide content at the outlet showed significant $1765\,ppm$ discrepancy. For studying the role of the gap size, the detailed reaction mechanism was used.

Table 4.1: Comparison of different chemical models.

Model	Reaction	CO conversion	H_2 conversion	CO [ppm]	H_2 [ppm]
EDC	3 steps	0.936	0.993	3240	123
EDC	37 steps	0.971	0.990	1475	163

All the present simulations were performed in steady-state and are thus confined to the melting phase only. Due to the high temperatures in the PCC, the ideal gas law was considered definitely accurate. The calculated Prandtl number along the PCC was comprised within the range $0.46 - 1$; more specifically, 0.73 at the gap and 0.46 at the inlet (the typical value for standard air being 0.7).

Compressibility effects due to density variations proved to be negligible because the Gay-Lussac number $Ga = \alpha_0(T_w - T_0)$ (where α_0 is the volumetric

thermal expansion coefficient at constant pressure; T_w is the wall temperature and T_0 is a reference temperature) is lower than the Peclet number $Pe = Re \cdot Pr$; in fact, the calculated ratio Ga/Pe along the PCC was between $2 \cdot 10^{-6}$ and 0.5, with a spatial average on the order 10^{-4}.
The Mach number was calculated in each cell of the fluid domain; the maximum Mach local number never exceeded 0.065, hence comprimibility effects due to velocity are vanishing.
The numerical solution was considered to reach the converged solution when the residuals of energy and DO equations were less than 10^{-6}, for species quantities less than 10^{-4} and continuity and turbulence residuals less than 10^{-5}.
The present numerical simulations, which included the combustion of the hydrogen and carbon monoxide, were performed for gap sizes comprised in the range $4\,cm - 50\,cm$, therefore the *opening coefficient* ζ (Figure 4.1) tested in this study varied in the range $0.13 - 0.64$:

$$\zeta = \frac{A_{gap}}{A_{gap} + A_{inlet}}.$$

The pressure drop $\Delta p = p_{inlet} - p_{outlet}$ along the PCC was calculated for both reactive and non-reactive flows and compared to the pressure drop due to incompressible, isotherm flow (Figure 4.2). Obviously the last two cases (non-reactive, compressible flow and incompressible, isothermal flow) are idealized flows that do not exist in the real PCC; and yet they may provide an indirect confirmation of the validity of the present simulation. It is seen that the lowest pressure drop is found in case of reactive, compressible fluid flow and, most importantly, it barely varies with the opening coefficient.
The calculated streamlines demonstrated a turbulent pattern of flow (Figures 4.3-4.4-4.5), with creation of tortuous streamlines and macro-recirculating zones due to abrupt changes of direction and stagnate zones.

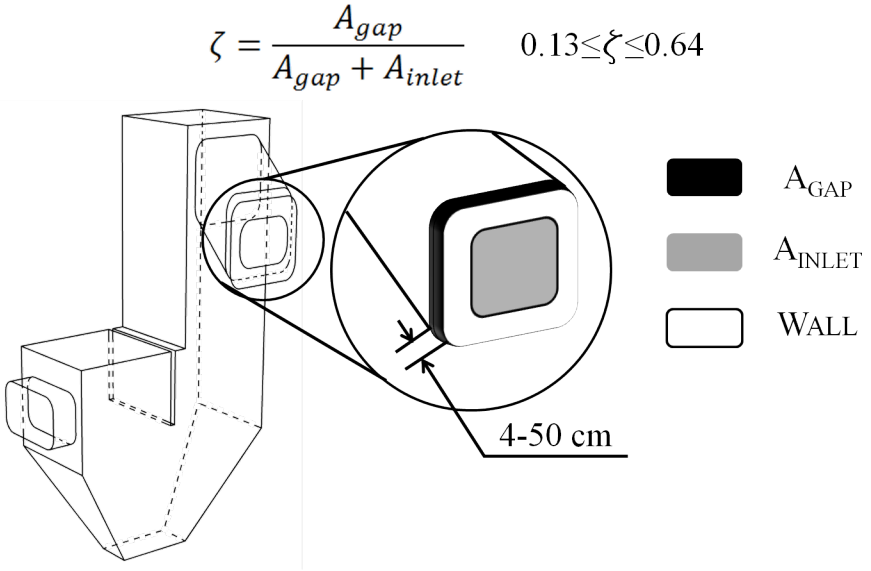

Figure 4.1: The opening coefficient ζ.

In the initial part of the PCC, the hot exhaust gases are forced to flow downwards, that is against the thermal gradient (hot gases notoriously rise due to buoyancy effects). While the above factor cannot possibly help in smoothing the flow, it may help in settling down particles, which are always detected in exhaust gases.

Tortuous streamlines also lead to longer residence times . Interestingly enough, the streamlines issuing from the gap and from the inlet have different features.

If $\zeta = 0.52$, a strong recirculating zone appears beyond the reaction area (zone A, Figure 4.4 right), which is undesirable.

If $\zeta = 0.64$, the inlet streamlines are smooth, showing a neat core flow with no recirculating zones and basically no interaction with the ambient air flow entering the PCC; the air flow from the gap is forced by the inlet flow to create two strong stagnate regions (zones A and B, Figure 4.5 left). As a

result, residence times from the inlet and the gap are very different, which translates in a poor mixing.

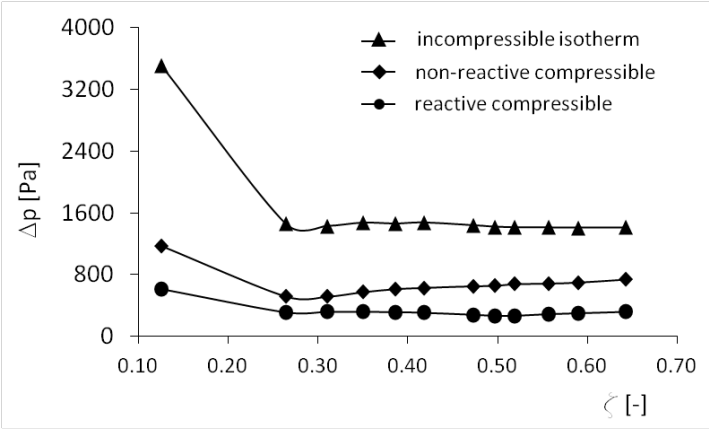

Figure 4.2: Global pressure drop through the PCC for reactive compressible flow, non-reactive compressible flow and incompressible isotherm flow.

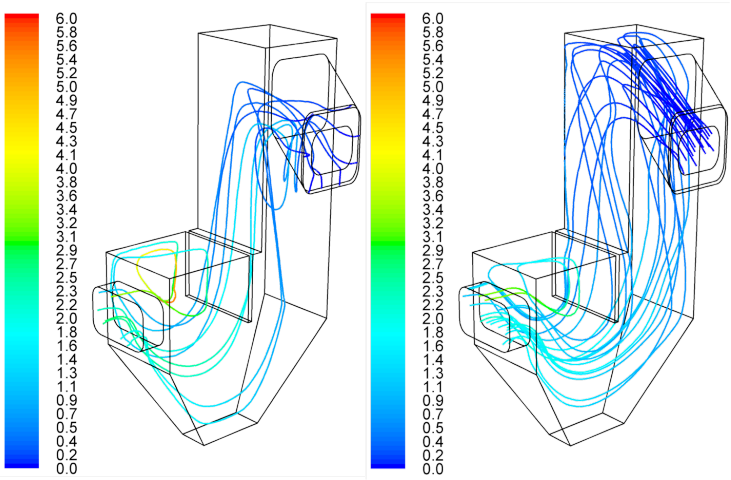

Figure 4.3: Residence times [s] for $\zeta = 0.26$ and streamlines originating at the gap (left) and at the inlet (right).

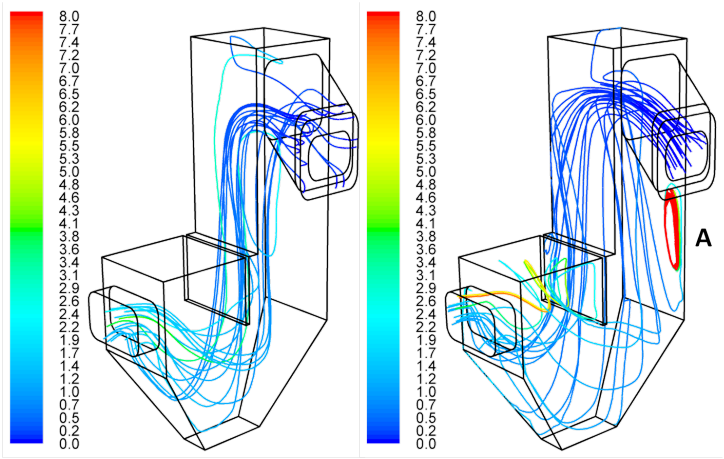

Figure 4.4: Residence times [s] for $\zeta = 0.52$ and streamlines originating at the gap (left) and at the inlet (right).

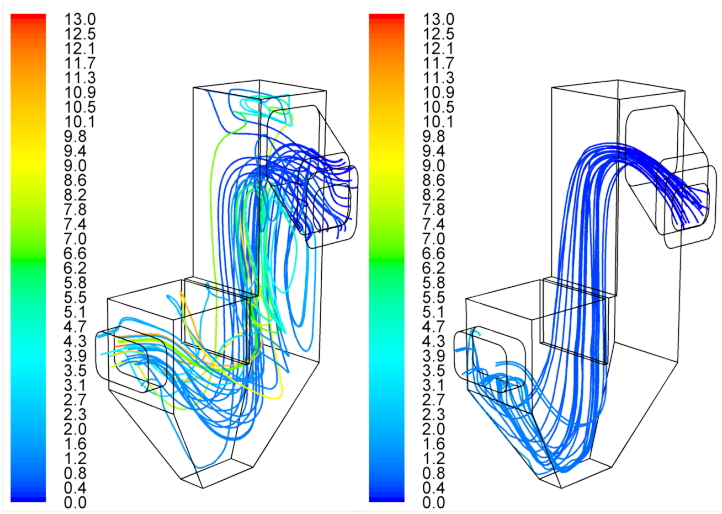

Figure 4.5: Residence times [s] for $\zeta = 0.64$ and streamlines originating at the gap (left) and at the inlet (right).

4.1.3 Mixing

The main purpose of the PCC is to combust hydrogen and carbon monoxide; the chemical reactions taking place in the PCC occur when the flowing reactants have reached a convenient level of mixing at molecular scale in a conveniently hot environment. Mixing may be qualified by the Kolmogorov scale [76], which not only shows the mixing quality but it also dictates the correct size of the discretization elements:

$$\eta_K = \left(\frac{\nu^3}{\varepsilon}\right)^{1/4}.$$

The lowest η_K-scale is found in the outer layer of the mixing zone, while the longest scale in the core inlet (Figure 4.6). In the region where the oxidation of hydrogen and carbon monoxide takes place, the η_K-scale is on the order of $10^{-3}\,m$, which is admittedly large as compared to other regions. This is due to the imposed boundary conditions at the gap-inlet; since the reaction zone is just downstream the gap-inlet, the turbulence has not had the chance to evolve to fine grain turbulence.
The Damköhler number is the ratio of the Kolmogorov time scale to the chemical reaction time scale:

$$Da = \left(\frac{\nu}{\varepsilon}\right)^{3/2} k\langle C^* \rangle,$$

where k is the reaction rate and $\langle C^* \rangle$ is the volume-averaged concentration of a given species in steady state. Since $Da \gg 1$ the reaction is fast, meaning that the chemical time scale is shorter than the turbulent time scale [77] and therefore reactions are completely driven by chemistry and not by mixing, as expected.

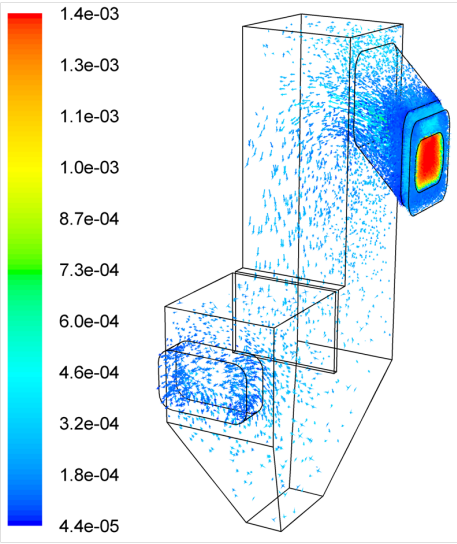

Figure 4.6: Kolmogorov length scale [m] $\zeta = 0.52$.

4.1.4 Mass flow rate

Since the outlet velocity is imposed as boundary condition, the mass flow rate is a function of the opening coefficient and of the temperature. The larger the gap, the lower the discharge exiting the furnace's free board (Figure 4.8 left).
The mass flow rate of the outlet was calculated by the well known 1D analytical expression:

$$\dot{m} = \sqrt{k}\left(\frac{p_0 A_{outlet}}{\sqrt{RT_0}}\right) M \left(1 + \frac{k-1}{2} M^2\right)^{-(k+1)/2(k-1)},$$

where $k = c_p/c_v$; p_0 is the stagnation pressure; T_0 is the stagnation temperature; A_{outlet} is the area of the outlet surface; $R = c_p - c_v$ is the gas constant and M is the Mach number. This equation is mainly used to evaluate the choked flow regime in compressible flow. The results favorably compared to the numerical results (Figure 4.8 right) and this is a solid

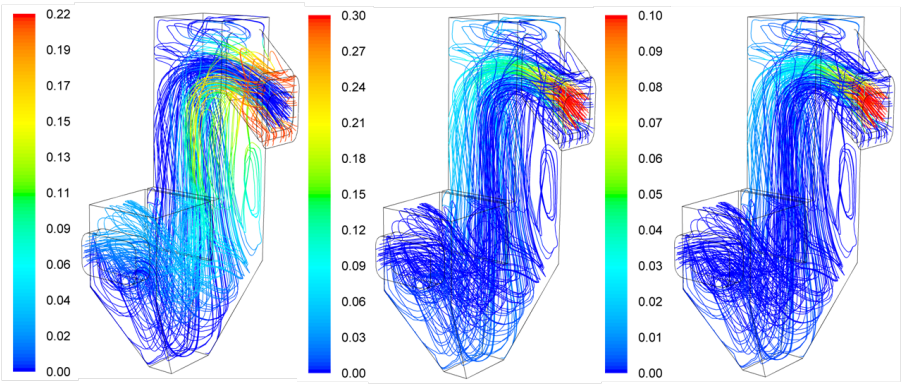

Figure 4.7: Gas streamlines originating from both inlet and gap colored by oxygen mass fraction (left), by carbon monoxide mass fraction (middle) and by hydrogen mass fraction (right) for $\zeta = 0.52$.

validation of the accuracy of the present simulation. The slight differences are only due to the 1D assumption of the analytical solution, which is not rigorously met at the 3D outlet.

The outlet discharge shows an asymptotic tendency in the range $0.4 < \zeta < 0.5$, which has no easy explanation. It is emphasized that the decreasing discharge from the furnace translates in lower discharge of combustible gases (Figure 4.11 right).

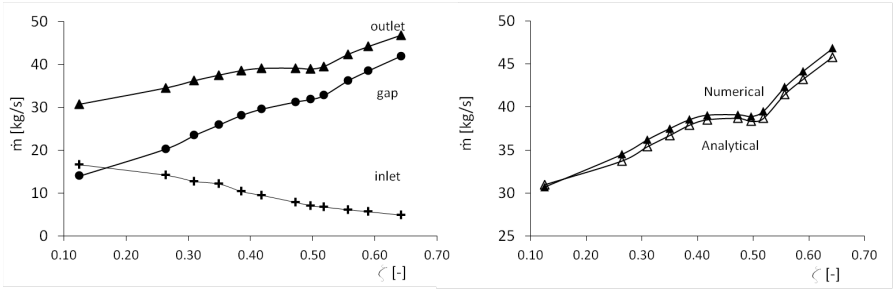

Figure 4.8: Distribution of mass flow rates (left) and outlet mass flow rates calculated numerically and analytically (right).

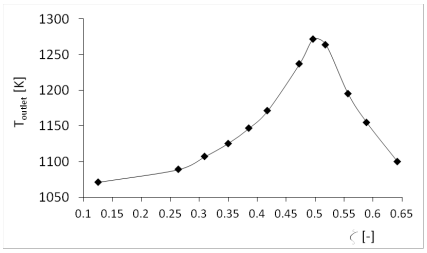

Figure 4.9: Spatially averaged temperature at the outlet section.

As the gap enlarges, more oxygen and less combustible gas enter the PCC, leading to a more thorough oxidation process, as Figure 4.9 proves. In fact, the maximum outlet temperature ($1272\,K$) occurs at $\zeta = 0.5$, where ambient oxygen mixes with the off-gas according to the stoichiometric amount and the reaction heat is released completely; for smaller opening values ($\zeta < 0.5$), the oxygen deficit leads to incomplete oxidation and the temperature remains low; larger gap sizes ($\zeta > 0.5$) result in excess oxygen and the reaction is still complete; nevertheless, the large amount of cold air drops down the temperature.

4.1.5 Conversion and thermal recovery rate

The conversion of combustible gases (φ) is calculated as:

$$\varphi = \frac{n_{in} - n_{out}}{n_{in}},$$

where n_{in} and n_{out} are respectively the entering and exiting molar flow rate of a given combustible component (H_2 or CO).
The thermal recovery rate, η, of the PCC was calculated by the following expression:

$$\eta = \frac{H_{wall}}{H_{in} + H_{react}},$$

where H_{wall} is the exchanged heat through the water-cooled walls; H_{in} is the enthalpy of the entering gases through both the gap and the inlet and H_{react} is the reaction heat released in the PCC by oxidations.
The maximum thermal recovery rate is: $\eta_{max} \sim 0.65$ at $\zeta \sim 0.4$ (Figure 4.10 left).

Since the total discharge of the furnace decreases, less combustible gas enters the PCC (Figure 4.10 right). Despite the monotone increase of the conversion rates of hydrogen and carbon monoxide (Figure 4.11 left), the released reaction heat shows a maximum at $\zeta \sim 0.48$ (Figure 4.11 right).

The conversions of hydrogen and carbon monoxide remain both low (i.e., below the required level) up to $\zeta \sim 0.5$; a further increase of the opening

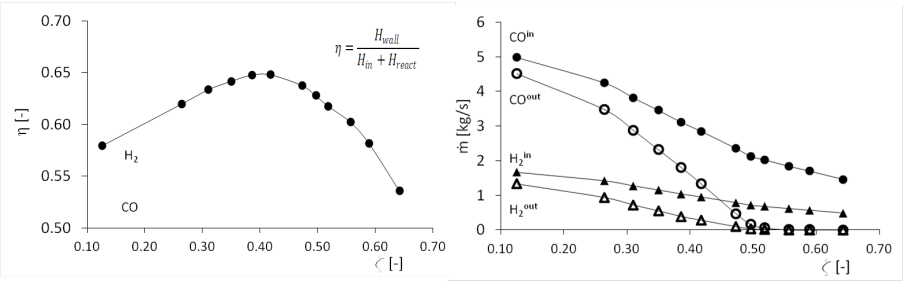

Figure 4.10: Thermal recovery (left) and mass flow rate of H_2 and CO (right).

Table 4.2: Summary of the maximum values of relevant variables.

Variable	Maximum value	ζ
$T_{outlet}\,[K]$	1272	0.50
$\eta\,[-]$	0.65	0.40
$H_{react}\,[MJ]$	1020	0.48
$\varphi\,[-]$	1	> 0.52

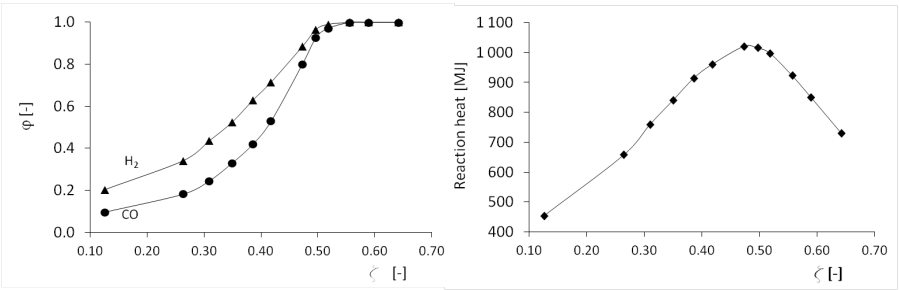

Figure 4.11: The conversion of combustible gases (left) and the reaction heat released in the PCC (right) versus the opening coefficient.

coefficient does not change the conversions and excess oxygen occurs in the PCC.

Table 4.2 has been compiled from the above data and gives a summary of the most relevant maximum values: it is seen that the value of the opening coefficient capable of maximizing all the relevant parameters is not unique, but it is a function of the relevant variable of choice.

Low outlet temperatures are advisable to protect the plastic filters of the baghouse where exhaust fumes will be treated; the typical required temperature for the gases to be admitted in the baghouse is $120\,°C$. For this reason, the opening coefficient $\zeta \sim 0.5$ would not be recommended. For smaller gap size, the reactions are not complete and the amount of harmful gases is still high. As a result, only the larger gap sizes must be used to comply with environmental requirements; however, it is emphasized that larger gap sizes produce lower discharges from the furnace, lowering the performance of the whole process. In other words, the process of fumes evacuation needs an optimization analysis to find the optimal ζ value; at the present state of knowledge, design values of the opening coefficient in the range $0.40 - 0.52$ appears to be reasonably serviceable.

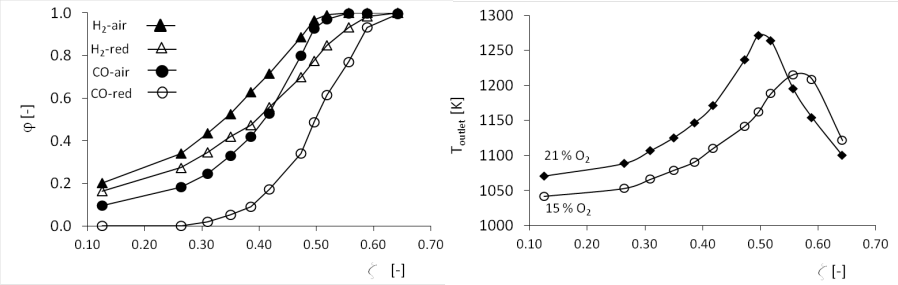

Figure 4.12: Influence of the gap oxygen content on the conversion of combustible gases (air=21 % O_2; red=15 % O_2 at the gap) (left) and on the average outlet temperature (right).

4.1.6 The influence of the boundary conditions

4.1.6.1 On the imposed oxygen content at the gap

Exhaust fumes do show appreciable differences in terms of temperature, chemical energy content and quantity, depending on the energy load contained in the scrap metal; the CO volume content during the melting phase may be as high as 25 % [22].
During the production of steel, the composition and temperature of the air surrounding the furnace might well differ from the standard atmospheric air because the gap is very close to the EAF: the imposed boundary conditions at the gap are therefore affected by this issue. For this reason, we also carried out simulations where the gas compound was different from the atmospheric air. The oxygen content at the gap was lowered to 15 % and 6 % of carbon dioxide was supposed to be in the mixture.

The less the oxygen content at the gap, the less the oxygen entering the PCC; since the mass flow rate barely differs, conversions are lower for any opening coefficient (Figure 4.12 left) and less heat is released by oxidation; the final result is that the maximum temperature at the outlet decreases (Figure 4.12 right) and, in addition, the maximum is reached for higher val-

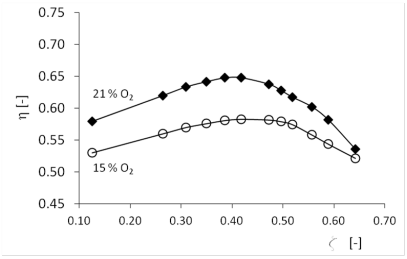

Figure 4.13: Influence of the gap oxygen content on the thermal recovery.

ues of gap openings (from $\zeta = 0.50$ to $\zeta = 0.57$). The thermal recovery is also less efficient (Figure 4.13), showing the same shift of the maximum value.

4.1.6.2 The imposed air temperature at the gap

The inlet section considered in this study is located few metres downstream the furnace's free board and the issue arises about the reasonable value to be imposed as boundary condition for the gap temperature. Li et al. (2003) [33] assumed for the temperature at the dome wall the value $1573\,K$. Kirschen et al. (2006) [18] measured variable gap temperatures oscillating from $313\,K$ to $1923\,K$ during the tap-to-tap cycle.
The temperature of the ambient air entering the gap, as mentioned in section 3.1.7, was assumed to be a reasonable $T_{Gap} = 473\,K$ due to the close proximity of the gap to the dome. To investigate the impact of this assumption on the key variables of the process, a few trials were performed by imposing the air temperature at the gap to be $300\,K$ and $700\,K$ for $\zeta = 0.52$ ($30\,cm$). As a result, the mass discharge varies appreciably (some $10\,\%$ difference, Figure 4.14, left) together with the conversions (Figure 4.14, right); the variation of the thermal recovery is almost linear (Figure 4.15, left), but the average temperature at the outlet section shows a point of alleged maximum

at $473\,K$, which could not be expected a priori.

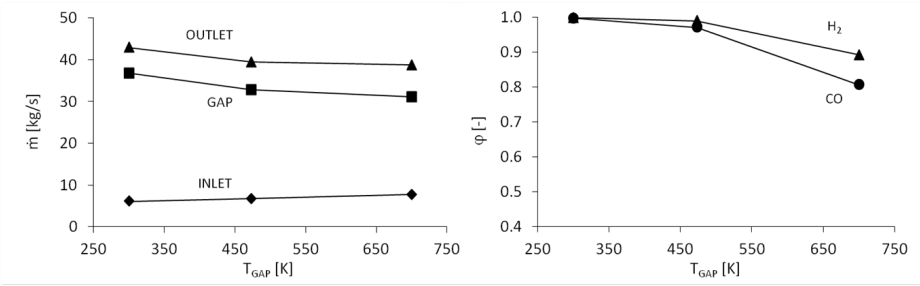

Figure 4.14: Mass flow rates (left) and conversion of hydrogen and carbon monoxide (right) as a function of the imposed gap temperature for $\zeta = 0.52$.

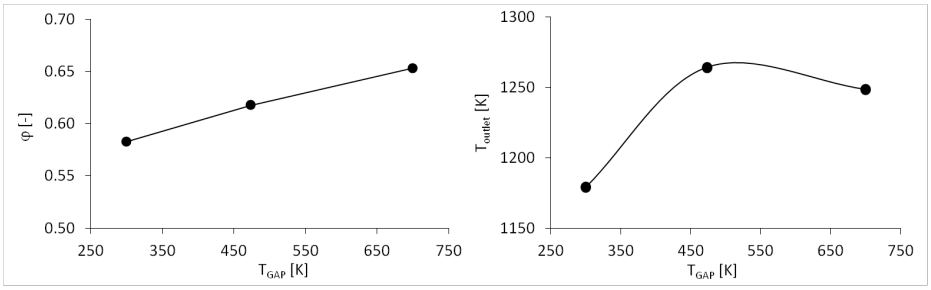

Figure 4.15: Thermal recovery (left) and spatial average outlet temperature (right) as a function of the imposed gap temperature for $\zeta = 0.52$.

The mass flow rate varies with the imposed gap temperature, leading to higher discharge from the furnace (*INLET* in Figure 4.14) and lower conversion rates for both hydrogen and carbon monoxide.

4.1.6.3 On the imposed turbulence intensity

Turbulence intensities of the off-gases entering the PCC are clearly not known and not even measurable; to evaluate the effect of the turbulence intensity, three simulations were performed by imposing at both the gap

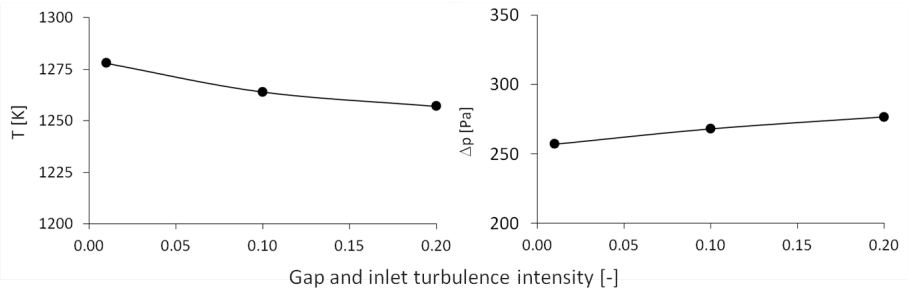

Figure 4.16: Average outlet temperature (left) and global pressure drop (right) as a function of turbulence intensity for $\zeta = 0.52$.

and the inlet the values 1 %, 10 % and 20 % for turbulent intensities for $\zeta = 0.52$.

It was found that the outlet temperature decreases as the initial turbulence intensity increases; however, the decrease is vanishing ($\sim$ 1.5 %) (Figure 4.16, left).

The effect on the pressure drop is found more evident; the larger the turbulence intensity, the higher the pressure drop ($\sim$ 7.5 %) (Figure 4.16, right).

4.1.7 Geometry enhancements

Two modified geometries were also implemented to investigate possible enhancements from the fluid dynamics point of view:

(i) the first enhancement is intended to improve the global smoothness of the flow by removing as far as feasible 3D effects; the original geometry (Figure 3.1) shows that the inlet and outlet sections are located in the plane (y-z) and (x-z) respectively; the flow must undergo a change of plane and this makes 3D effects more pronounced, at least in principle. The modified geometry (Figure 4.17 left) shows the coplanar inlet and outlet sections, both located on the same (x-z) plane, the flow evolution being only along the (y-z) plane apart from other 3D unavoidable secondary effects. It is seen

from Table 4.3 that this modification does not decrease the global pressure drop Δp; and

(ii) the second enhancement is intended to improve the local smoothness of the flow at the gap-inlet region; the original geometry (Figure 3.1) shows the gap flow that enters the PCC perpendicular to the inlet flow and this is not the efficient way to merge the two different streams. The modified geometry (Figure 4.17 right) shows the more logical (and less dissipative) merging of the two streams and Table 4.3 shows a remarkable 50 % reduction of the primitive pressure drop; this is of paramount concern to decrease the fan power of the baghouse.

The implementation of both the above enhancements does not give extra benefit (last line of Table 4.3).

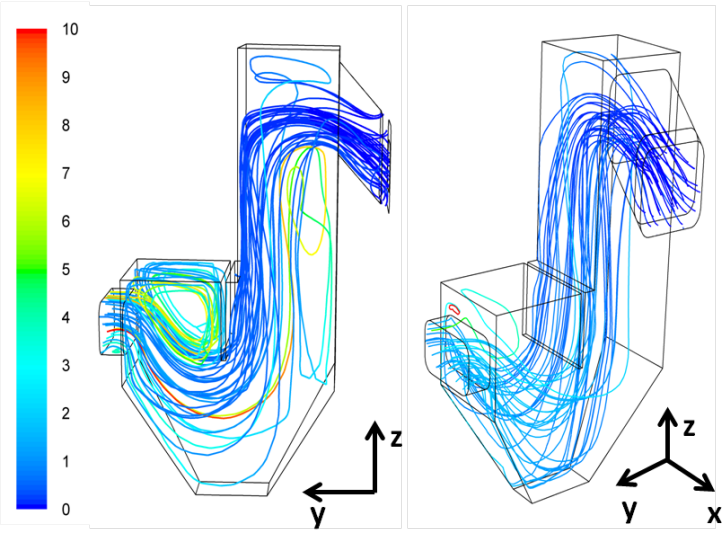

Figure 4.17: Gas streamlines when inlet and outlet are aligned (left) and inlet and gap are aligned (right). Streamlines are colored by residence time [s].

Table 4.3: Global pressure drop $\Delta p = p_{inlet} - p_{outlet}$.

Geometry	ζ	Δp [Pa]
Original (Figure 3.1)	0.59	300
Original (Figure 3.1)	0.64	319
Aligned inlet-outlet (Figure 4.17 left)	0.56	307
Aligned inlet-gap (Figure 4.17 right)	0.61	200
Aligned inlet-outlet-gap	0.61	241

4.1.8 On the accuracy of 2D simulations

The computational effort for 3D thermal fluid dynamics simulations of steady state reacting flows is huge and requires an equally huge computing resource; for example, the typical CPU time for a $6 \cdot 10^5$ element mesh is on the order of 15 hours in a 4 processor, $3\,GHz$, $16\,GB$ RAM computer.
The computational effort can thus turn out as a critical issue, capable of becoming a limiting factor for obtaining realistic simulations and trustworthy results. Hence 2D simulations are most appealing even though they provide less accuracy (which, however, can be tolerated in the pre-design stage). Table 4.4 summarizes the preliminary results obtained in terms of pressure drop for $\zeta = 0.56$.

Table 4.4: Summary of the preliminary studies ($\zeta = 0.56$).

PCC geometry	Elements #	Mesh	$\Delta p\,[Pa]$	CPU $[h]$
original (Figure 3.1)	$6.2 \cdot 10^5$	3D	289	~ 15
original (Figure 3.1)	$1.6 \cdot 10^5$	3D	264	~ 7
aligned (Figure 4.17 left)	$6.2 \cdot 10^5$	3D	307	~ 15
aligned (Figure 4.18)	$8.2 \cdot 10^3$	2D	271	~ 1

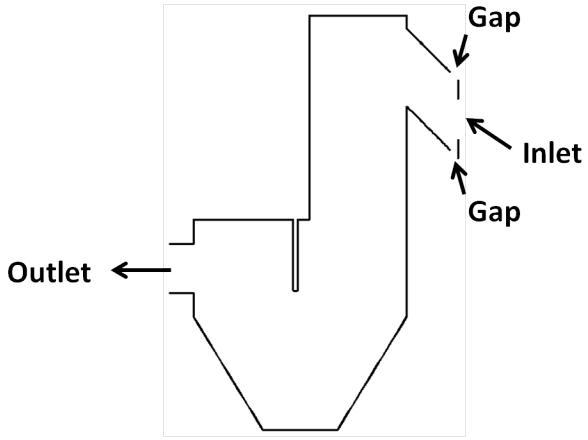

Figure 4.18: 2D PCC with opening coefficient $\zeta = 0.56$.

In the preliminary stage of PCC design, 2D simulations can thus be safely used, with the aim to apply rigorous 3D simulations to the final geometry.

4.2 Secondary line

4.2.1 Preliminary study

The boundary conditions of the preliminary studies (Section 3.2.6.1) were based on the data received from the Stg company Spa. The typical calculation time was 9 hours using a 4 processor, $3\,GHz$, $16\,GB\,RAM$ computer. The numerical solution was considered to reach the converged solution when the residual of energy was less than 10^{-6} and continuity and turbulence residuals less than 10^{-5}.
To handle density variation (due to temperature) and compressibility of the flow the Boussinesq approach and ideal gas law were both applied. The Boussinesq approximation's (Equation 4.2 left) advantage over the ideal gas law (Equation 4.2 right) is the modest computational requirement.

$$\rho = \rho_0 \beta (T - T_0) g, \qquad \rho = \frac{p_{op} - p}{\frac{R}{M} T}, \tag{4.2}$$

where ρ is the gas density; β is the thermal expansion coefficient; T is the temperature; T_0 is the operating temperature; $g = 9.81\, m/s^2$ is the gravitational acceleration; p_{op} is the operating pressure; p is the local relative pressure; R is the gas constant and M is the molecular mass of the gas.
The calculated enthalpy fields can be seen in Figure 4.19 and in Figure 4.20 in case of Boussinesq approach and ideal gas law, respectively.
The differences of the obtained results are significant between the two approaches. However both take into account the buoyancy effects, the Boussinesq model does not handle the large temperature variations accurately, which leads to the underestimation of buoyant forces. For further calculations, the ideal gas law was applied.
The presence of the filled ladle affects the spatial temperature distribution in the factory, however the temperature remains sufficiently low on the working area (Figure 4.21).
The main outcome of the preliminary studies was the evaluation of the additional system's efficiency. Figure 4.23 clearly demonstrates the low efficiency

Figure 4.19: Contours of enthalpy (colormap is scaled in J/kg) calculated with the Boussinesq approach on the longitudinal (left) and transversal (right) cross sections (without ladle).

of the system; only the leftmost nine of the thirty holes work and at farther position, the flow below the evacuation system is stagnating. Consequently, this region can be eliminated from further studies.

Figure 4.20: Contours of enthalpy (colormap is scaled in J/kg) calculated with the ideal gas law on the longitudinal (left) and transversal (right) cross sections (without ladle).

Figure 4.21: Contours of enthalpy (colormap is scaled in J/kg)in the presence of filled ladle on the longitudinal (left) and transversal (right) cross sections (without ladle).

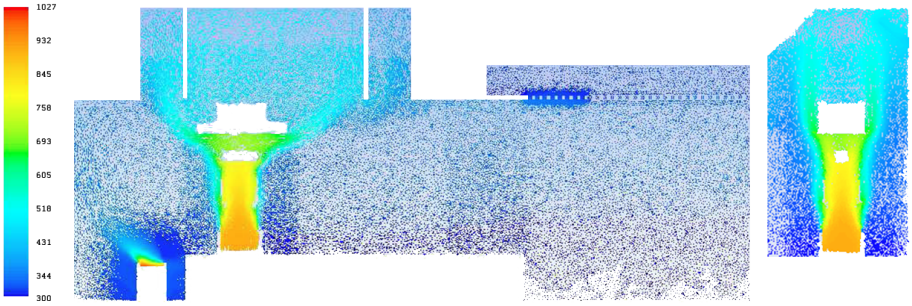

Figure 4.22: Longitudinal (left) and transversal (right) cross sections of the elephant house with ladle. (Vector sizes are proportional to the gas velocity and colored by temperature [K]).

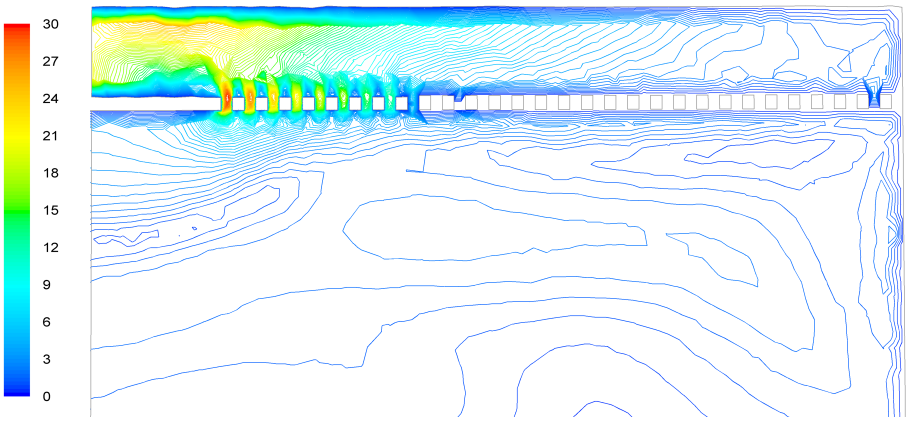

Figure 4.23: Contours of the velocity field at the additional evacuation system. The colormap is scaled in m/s.

4.2.2 Case study

After geometry and boundary condition modifications, based on the preliminary studies, experimental measurements and observations in the factory, the simulations of the elephant house were carried out with both steady-state and transient solvers.

4.2.2.1 Outer tubes

The typical calculation time of tube's simulation was 10 minutes using a $2.4\,GHz$, $4\,GB$ ram, dual-core four-way multi-task processor (Intel i5). In Figure 4.24 it can be seen that the highest discharge occurs in the leftmost tube $Q_1 = 411984\,m^3/h$, while the discharge from the central section is $Q_2 = 180576\,m^3/h$ and in the rightmost lateral section is $Q_3 = 351108\,m^3/h$. These values were implemented for the boundary conditions of the canopy hood's outlets (Table 3.10) during the simulation of the elephant house.
The T-junctions are sources of recirculations and also elevate the turbulence intensity which reduce the overall efficiency of the evacuation system. Figure 4.27 shows the recirculation that appears at the leftmost T-junction; the figure also clearly shows that the T-junction is the source of the turbulence.

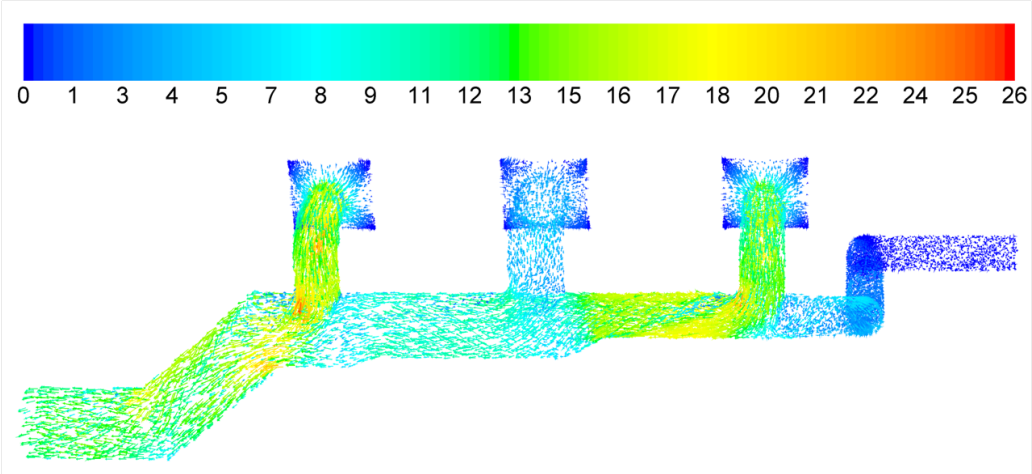

Figure 4.24: Velocity vector field in the tubes of the evacuation system. The colormap is scaled in m/s.

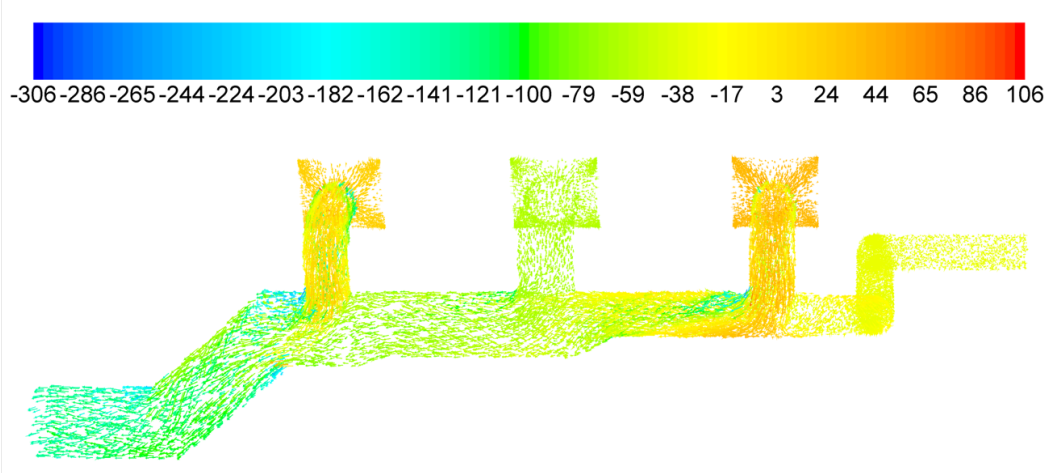

Figure 4.25: Velocity vectors colored by total pressure [Pa] in the tubes of the evacuation system.

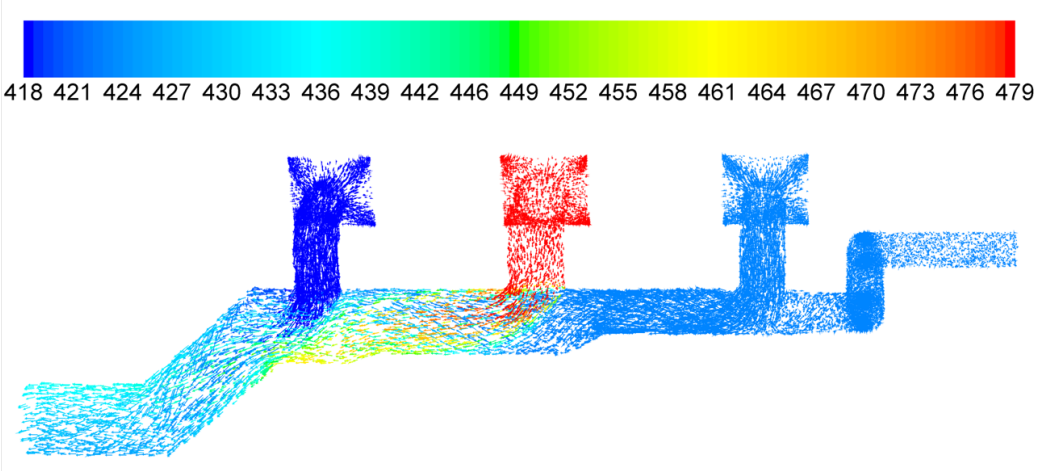

Figure 4.26: Velocity vectors colored by temperature [K] in the tubes of the evacuation system.

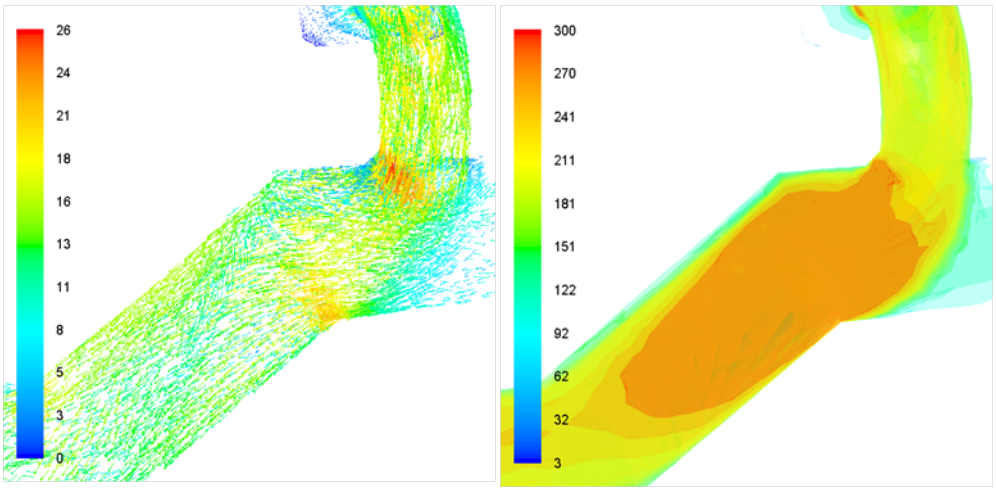

Figure 4.27: Velocity vectors colored by velocity [m/s] (left) and 3D spatial distribution of turbulence intensity [-] (right) at the leftmost T-junction of the outer tube.

4.2.2.2 Elephant house

4.2.2.2.1 Steady simulation

The steady-state simulation with the modified elephant house geometry and mesh took typically 4 hours using a 4 processor, $3\,GHz$, $16\,GB\,RAM$ computer, which is considerably shorter time compare to the computational time during the preliminary studies.

Calculations show that the fumes, originated from the furnace, partially disperse in the factory's ambient (Figure 4.28). However, the hot gases are mainly captured and withdrawn by the canopy hood, considerable amount of fume remains and accumulates in the melt shop.

The crane and its accessories do not help the smoothness of the flow and act as a barrier that must be dodged by the generated buoyant plume. The turbulence intensity also increases close to the crane's parts (Figure 4.29). The additional evacuation system does not operate during the charging phase, in order to reach the maximum discharge from the canopy hood.

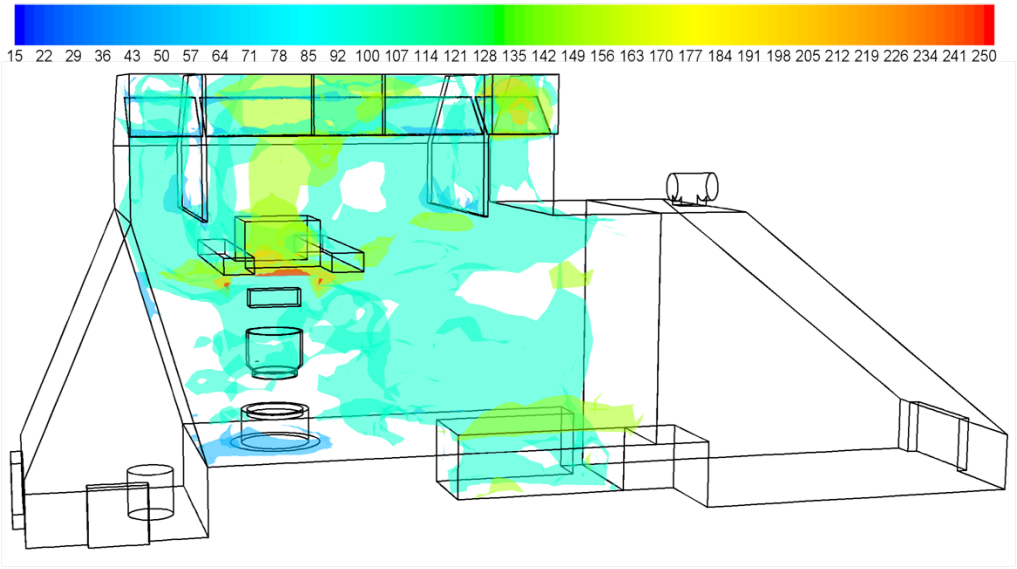

Figure 4.29: 3D spatial distribution of turbulence intensity [-] in the factory.

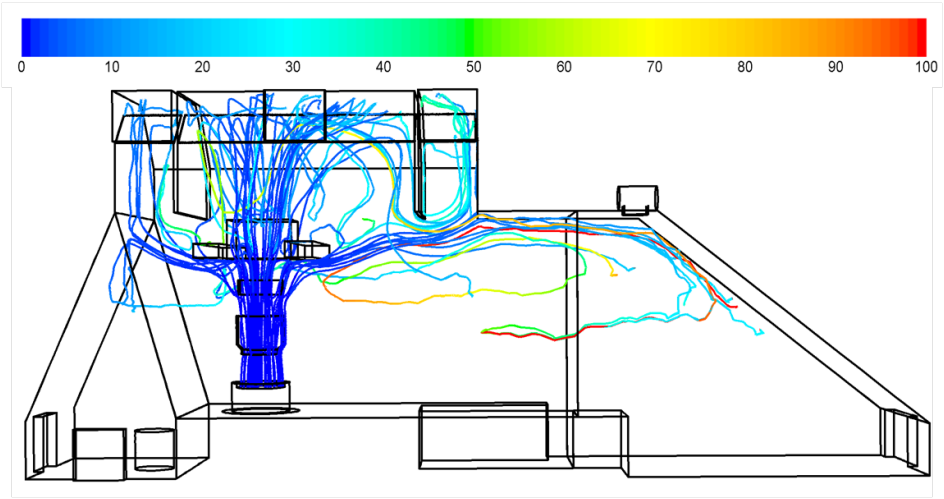

Figure 4.28: Stream lines of fumes released from the furnace. The colormap shows the residence time [s].

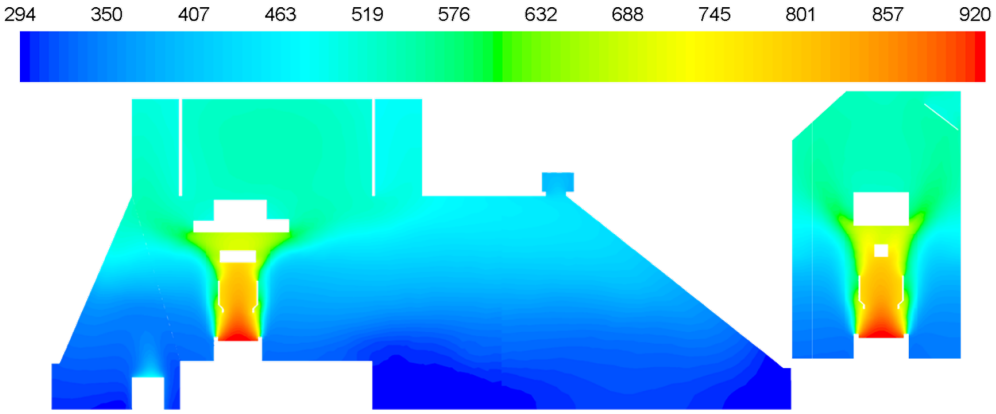

Figure 4.30: Spatial temperature distribution on the longitudinal (left) and transversal (right) cross sections of the factory. The colormap is scaled in Kelvin.

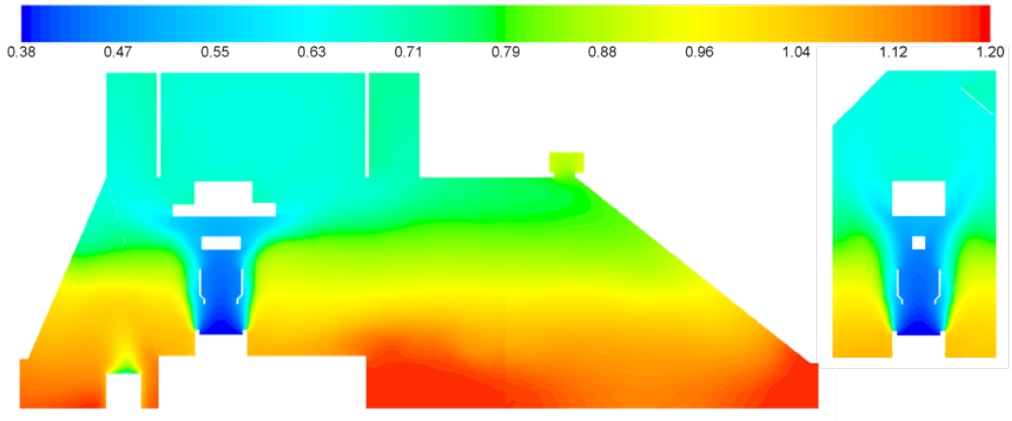

Figure 4.31: Density distribution on the longitudinal (left) and transversal (right) cross sections of the factory. The colormap is scaled in kg/m^3.

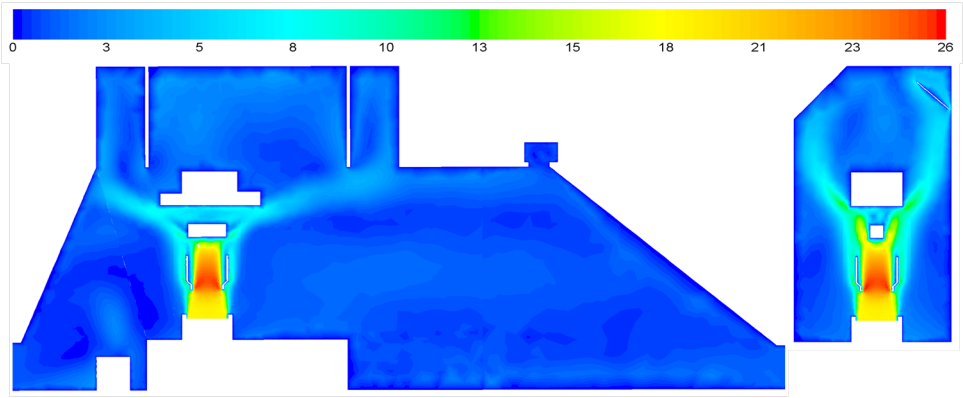

Figure 4.32: Velocity field on the longitudinal (left) and transversal (right) cross sections of the factory. The colormap is scaled in m/s.

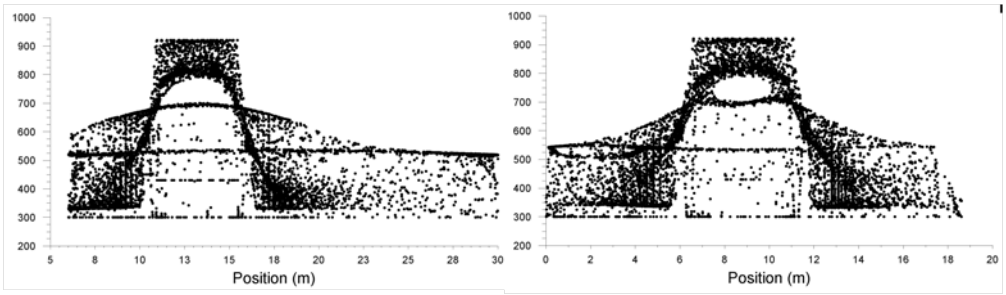

Figure 4.33: Temperature values on the longitudinal (left) and transversal (right) cross sections of the factory. The y-axis is scaled in Kelvin.

4.2.2.2.2 Transient simulation

For transient simulations, fully implicit solver was used therefore the proper Courant (CFL) number is not criteria of the calculation's stability and convergence, however the CFL value indicates the proper time step should be imposed to capture the transient nature of the flows. The CFL number is a dimensionless number and defined as:

$$CFL = \frac{\Delta t}{\Delta x_{cell}/v_{fluid}},$$

where Δt is the time step size, Δx_{cell} is the cell size and v_{fluid} is the velocity of the fluid flow. To ensure the appropriate time step size, the CFL number was ~ 1 at the beginning of the calculation process and never exceeded 60.

For this reason $10^{-3}\,s$ initial time step size was used that was increased gradually up to $0.1\,s$ as the calculation proceeded. The typical observed charging time in the simulated factory was between $15\,s$ and $20\,s$, therefore the transient simulations were carried out until $20\,s$.

The initial conditions for the transient simulations were provided by the steady-state simulation of the factory with closed furnace. Consequently, all the boundary conditions were the same as in the previous sets of simulation (Table 3.10) except the boundary condition that represents the furnace; the mass-flow rate was set to zero. When the boundary condition, which represents the charging of the furnace, was imposed a pressure blast wave occurred. The propagation of the wave can be seen in Figure 4.34. The velocity of the wave's propagation is the speed sound and the lower pressure zone after the blast can also be seen.

The calculated pressure distributions by the standard κ-ε and LES turbulence models are similar, however the LES model calculated considerably higher pressure value in the core of the shock wave ($4.4\,kPa$ against $3.0\,kPa$). While the propagation velocities are the same, the predicted pressure distributions are different; the LES model estimates significantly sharper pressure wave and the lower pressure region inside the pressure sphere has different profile.

The temperature distribution in the factory was monitored after $10\,s$ and $20\,s$ in order to examine whether the steady-state is established within these

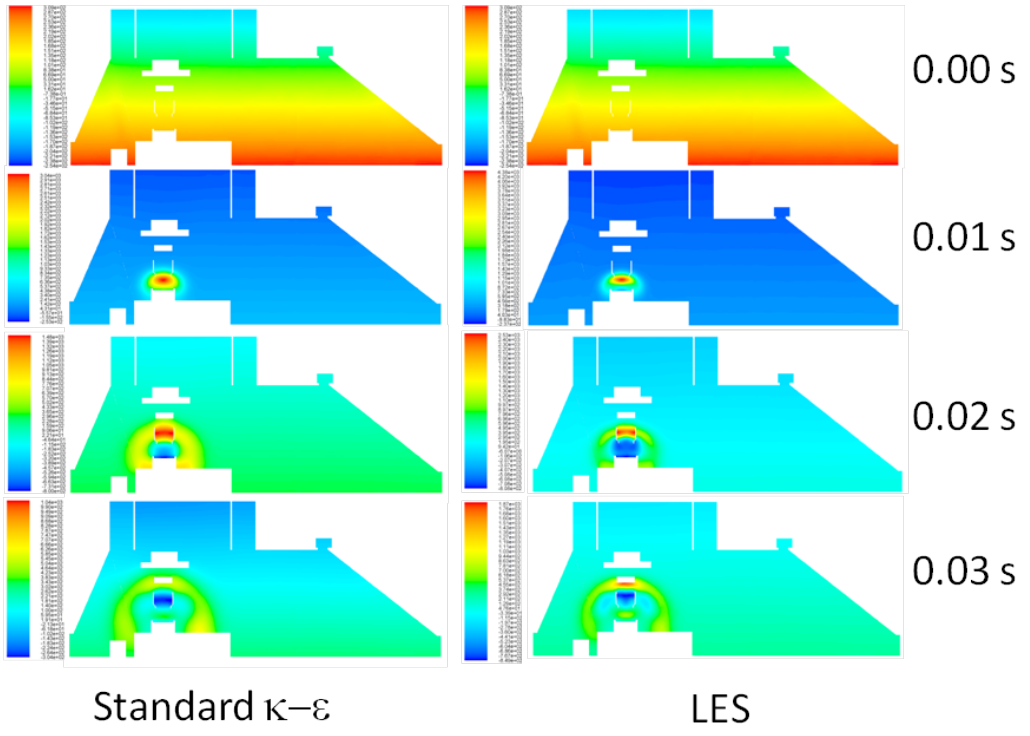

Figure 4.34: The total pressure field calculated with standard κ-ε (left) and LES (right) turbulence models on the longitudinal cross section of the factory at the beginning of the charging. The time scales are $0\,s, 0.01\,s, 0.02\,s$ and $0.03\,s$ from top to bottom. The colormaps are scaled in Pa.

time periods. In Figure 4.35 and Figure 4.36 the temperature values on both longitudinal and transversal cross section of the factory are depicted in case of steady and transient simulations. The results reveal that temperature values far from the furnace are significantly lower with transient simulations, while the temperature near by the furnace shows evanescent discrepancy.
The calculated temperature values on the transversal cross section of the factory at $1\,s$, $2\,s$, $5\,s$, $10\,s$ and $20\,s$ were compared using the standard κ-ε and the LES turbulence models (Figure 4.37). The results show vanishing discrepancy between the estimated temperature distribution by the two tur-

bulence models.

The spatial temperature distributions are shown in Figure 4.38 and Figure 4.39 calculated with the transient standard κ-ε and LES turbulence models compared to steady-state simulation results. However, differences in the predicted temperature distribution can be distinguished in local regions (above the ladle and around the crane) using different turbulent models for transient simulation, the global temperature distributions are very similar.

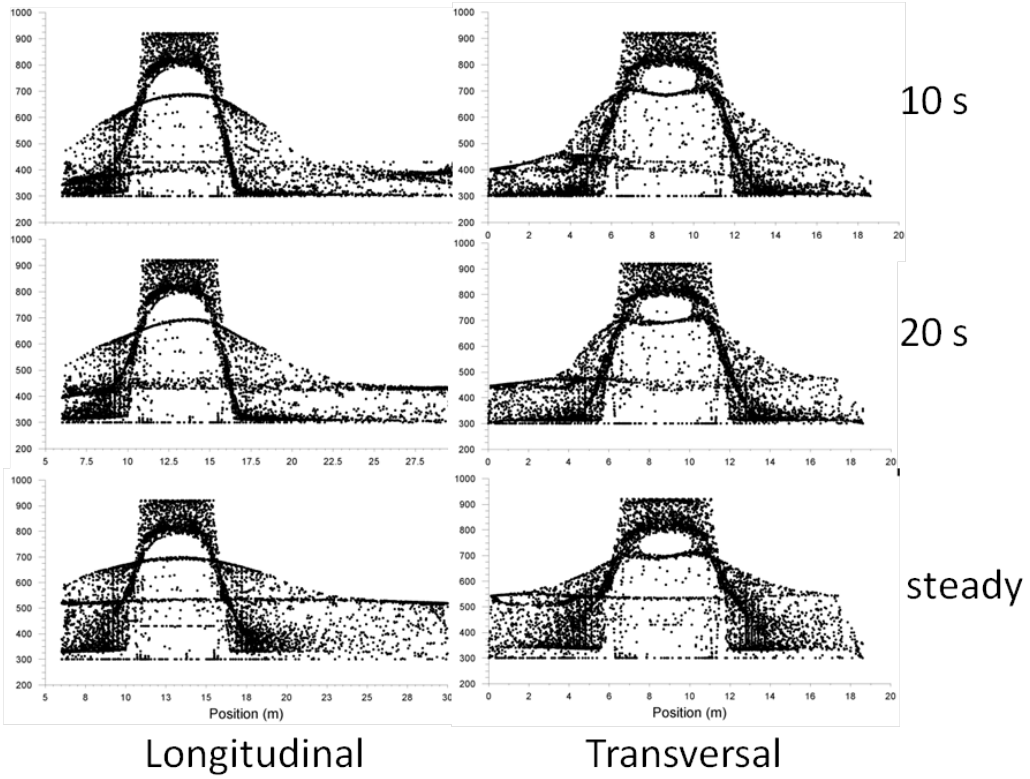

Figure 4.35: Temperature values on the longitudinal (left) and transversal (right) cross sections of the factory in case of steady and transient simulations, calculated with the standard κ-ε turbulence model. The y-axis is scaled in Kelvin.

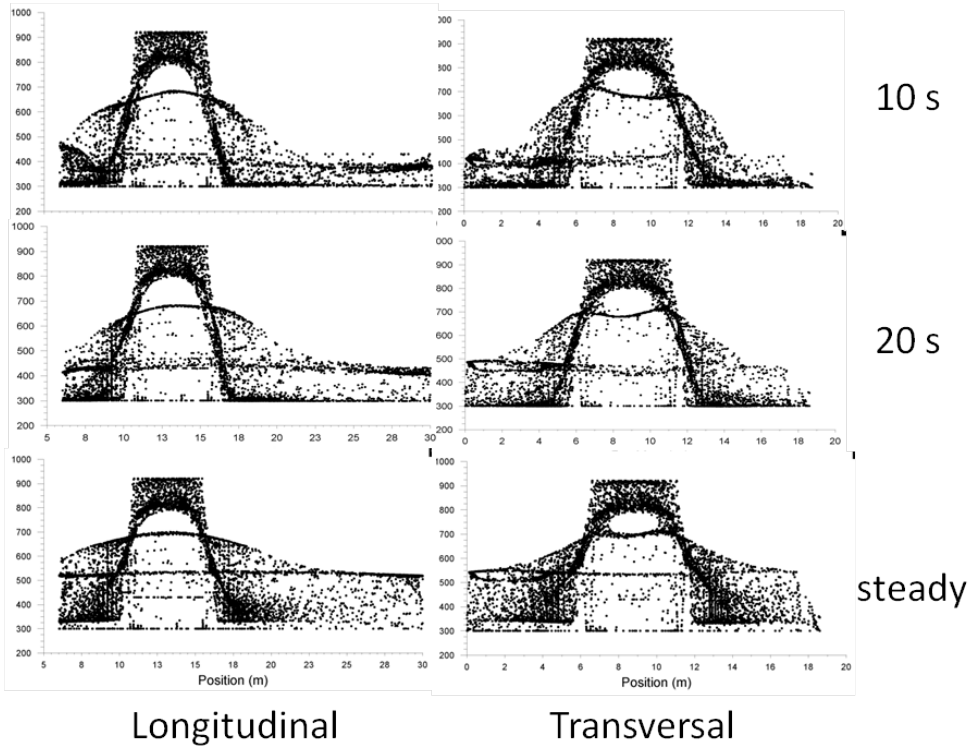

Figure 4.36: Temperature values on the longitudinal (left) and transversal (right) cross sections of the factory in case of steady and transient simulations, calculated with the LES turbulence model. The y-axis is scaled in Kelvin.

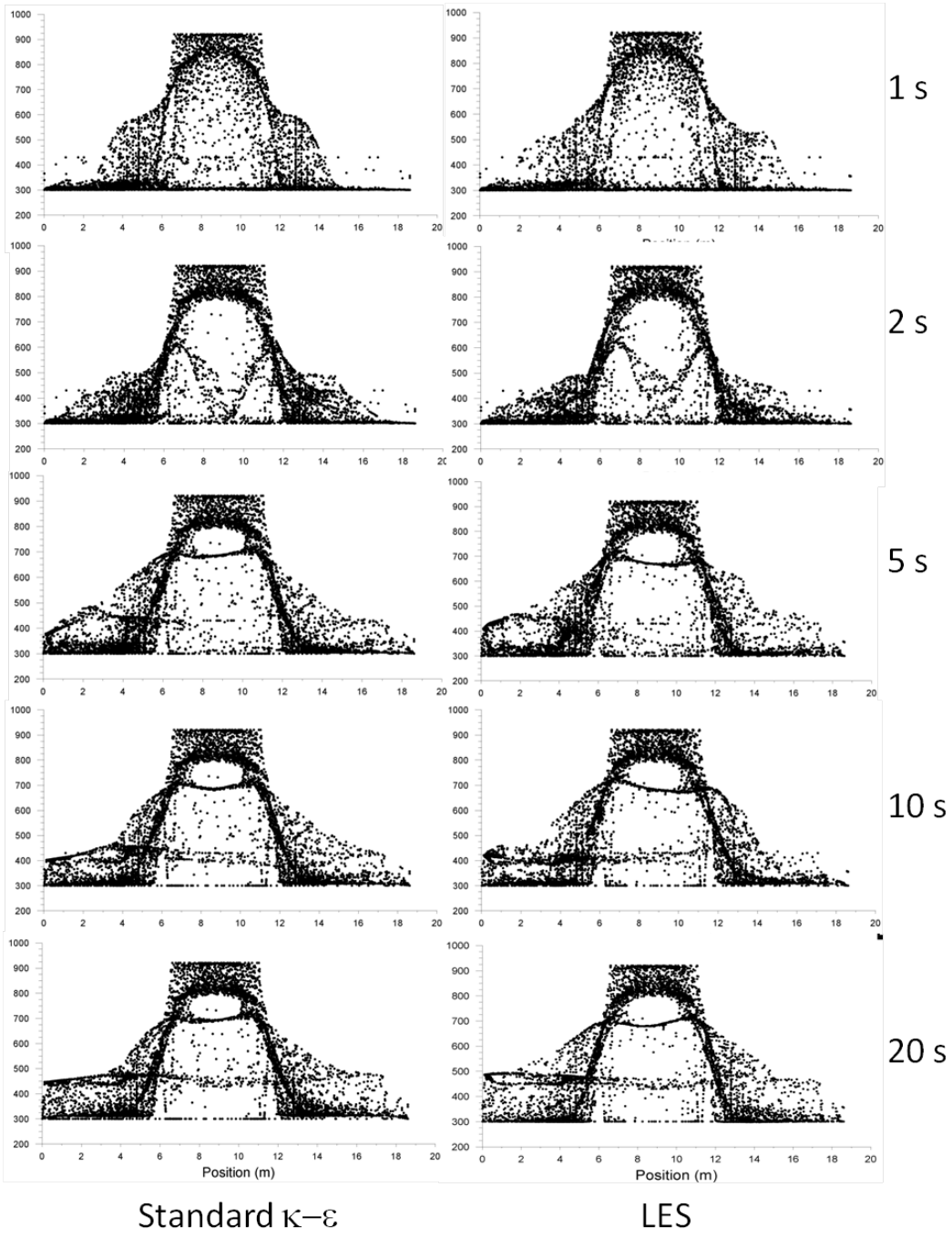

Figure 4.37: Temperature values on the transversal cross section of the factory. The y-axis is scaled in Kelvin.

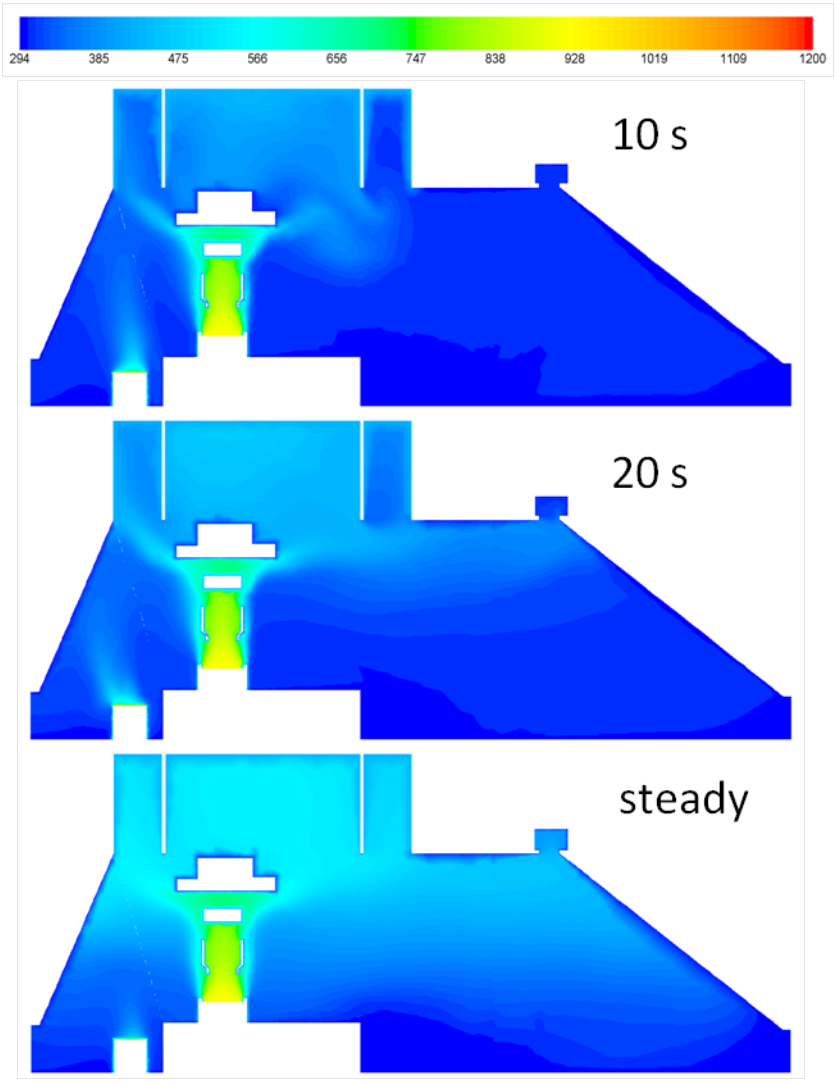

Figure 4.38: Calculated temperature distribution with the standard κ-ε turbulence model on the longitudinal cross section of the factory in case of steady and transient simulations. The colormap is scaled in Kelvin.

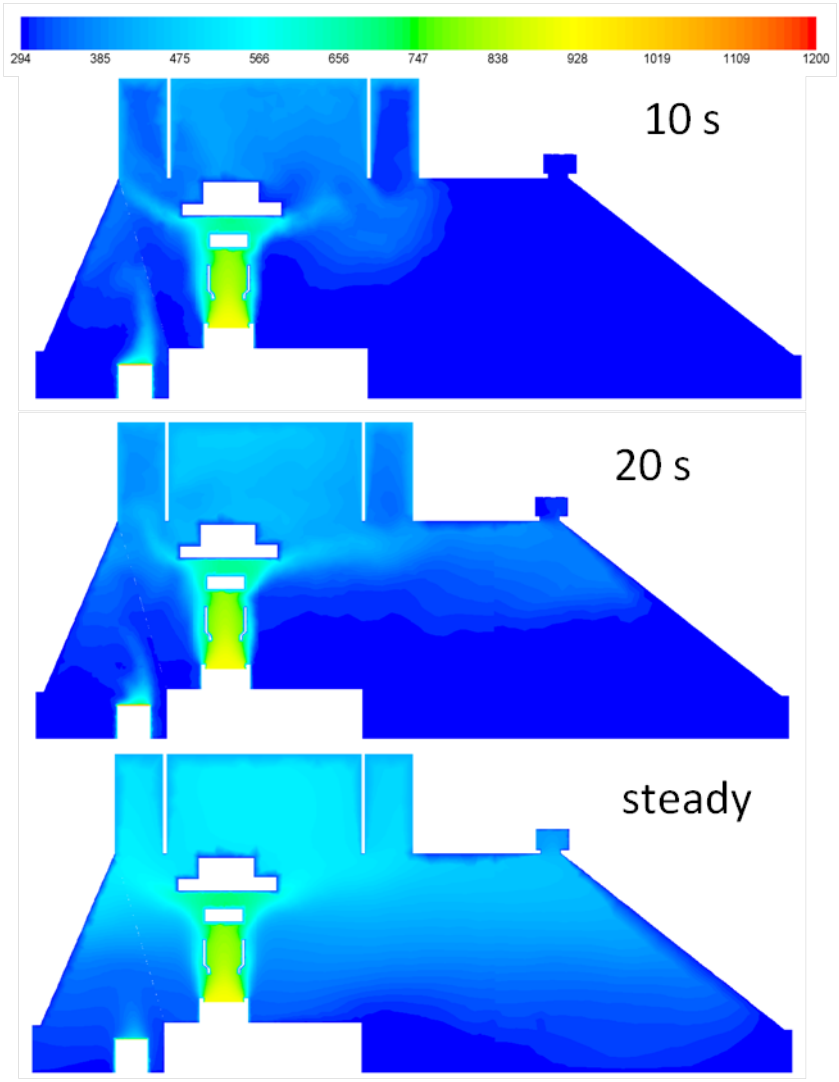

Figure 4.39: Calculated temperature distribution with the LES turbulence model on the longitudinal cross section of the factory in case of steady and transient simulations. The colormap is scaled in Kelvin.

The temperature at the outlets of the canopy hood can be compared to the measured data in the elbow (see Figure 3.14). The measured and calcu-

lated data for both steady and transient simulations can be seen in Table 4.5. It can be concluded, that the steady-state simulation with standard κ-ε turbulence model overpredicts the temperature at each outlet of the canopy hood, however provides the most accurate temperature values comparing to the measured data. In case of transient simulations with standard κ-ε and LES turbulence closures, the temperature values are significantly lower after both 10 and 20 seconds.

For transient simulations significantly higher computational cost is required, which is especially true for the more sophisticated LES turbulence model (typical CPU time was $\sim 48\,h$). The post-processing and data evaluation from transient simulations require demanding efforts compare to the steady-state simulations. The advantage of the application of transient simulation is the possibility to evaluate the unsteady fluid motions in the factory and the temporal fume storage in the canopy hood, however for practical engineering applications the steady-state simulation of the charging phase can provide the necessary information about the temperature distribution, recirculating and stagnating zones and the stream lines of the fumes that is a good indicator of the capturing ability of the evacuation system. In case of steady-state simulations, the over prediction of the temperature far from the furnace is a feasible risk, however, these results can be handled as a worst scenario.

The differences of the simulated and measured temperature values at the outlet can be induced by the inaccurate boundary conditions (furnace, doors).

Table 4.5: Comparison of measured and calculated temperatures at the outlets of the canopy hoods. SKE denotes the standard κ-ε turbulence model.

	Measured	Steady (SKE)	10 s (SKE)	20 s (SKE)	10 s (LES)	20 s (LES)
Out1	418 K	476 K	348 K	399 K	371 K	387 K
Out2	479 K	496 K	387 K	434 K	381 K	448 K
Out3	423 K	459 K	320 K	362 K	320 K	349 K

Furthermore, the walls of the studied factory contain countless small openings and gaps due to imperfect sealing, which sum up in a large extra opening but cannot be simulated due to discretization reasons.

4.2.3 Possible secondary caption enhancement considerations

The simulation of the secondary evacuation system revealed several points of the geometry that do not help the efficient way of capturing and withdrawing the hot fumes.
The inefficient nature of the additional evacuation system has been highlighted in section 4.2.1 and is clearly shown in Figure 4.23.
The deflection wall in the canopy hood generates turbulence and causes large pressure drop Figure 4.40. The harmful nature of the applied deflection wall is lying on its orientation; i.e., it is almost perpendicular to the flows. If the deflection wall was aligned to the flow motion (Figure 4.41 right), the pressure drop would be lower, while the recirculation of the fumes in the canopy was still suppressed and the fumes were conveyed directly to the outlets.
The outer tube system causes several efficiency losses due to its structure:

(i) the diameter of the conduit changes several times along the tube system. Both the reduction and the enlargement of the diameter (Figure 4.42)

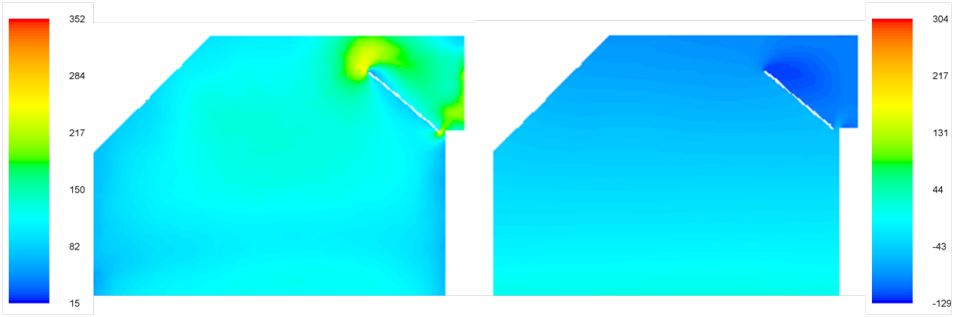

Figure 4.40: The turbulence intensity $[-]$ (left) and total pressure $[Pa]$ (right) in the transversal cross section of the factory at the Out3 of the canopy hood.

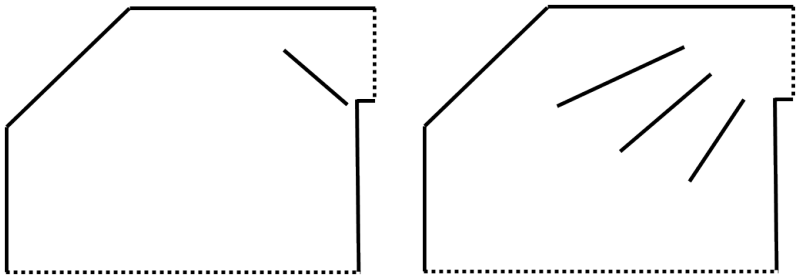

Figure 4.41: The original (left) and the proposed (right) deflection wall.

produce energy dissipation. When the fluid accelerates through a restriction the pressure decreases; the laminar boundary layer remains adherent to the walls and its thickness tends to decrease leading to energy losses.
Due to the enlargement, the fluid's motion decelerates and an adverse pressure gradient occurs leading to the detachment of the boundary layer and the separation of the stream from the wall that causes energy dissipation;

(ii) the hot fumes coming from the different sections of the canopy hood and from the additional evacuation system are merged in confluences (Figure 4.43). The velocities of the gases are different at each tube before merging, therefore the flow with higher velocity delivers a part of its kinetic energy to the slower one. This also leads to energy dissipation;

(iii) the fluid inside the tube system is subjected to change its direction in several bending and elbows where, due to the separated streams, energy

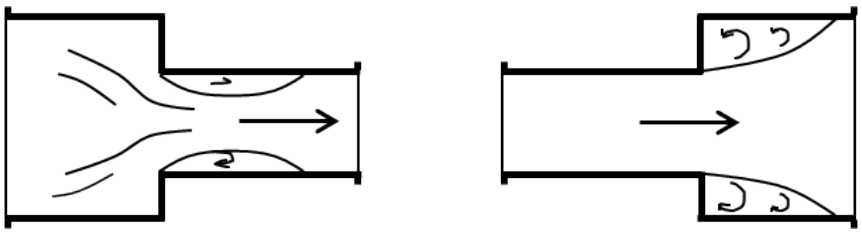

Figure 4.42: Schematic views of restriction (left) and enlargement (right) and their effect on the fluid motion.

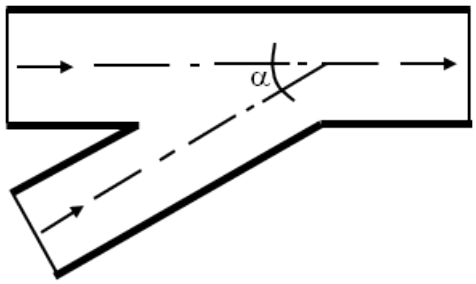

Figure 4.43: Schematic view of the confluence.

dissipation occurs.

To avoid separated flows, which always causes energy dissipation, the abrupt change of the direction must be avoided in elbows with possible reduction of the angle (α in Figure 4.44). Further solution to reduce the energy loss due to bending and elbows is to add series of thin, curved fins or even shaped profiles (Figure 4.45). The mounted fins can significantly reduce the agitation of the fluid motion downstream the elbow, resulting a laminar flow with uniform velocity distribution.

The outer tubes contain all the above mentioned geometries (restriction, en-

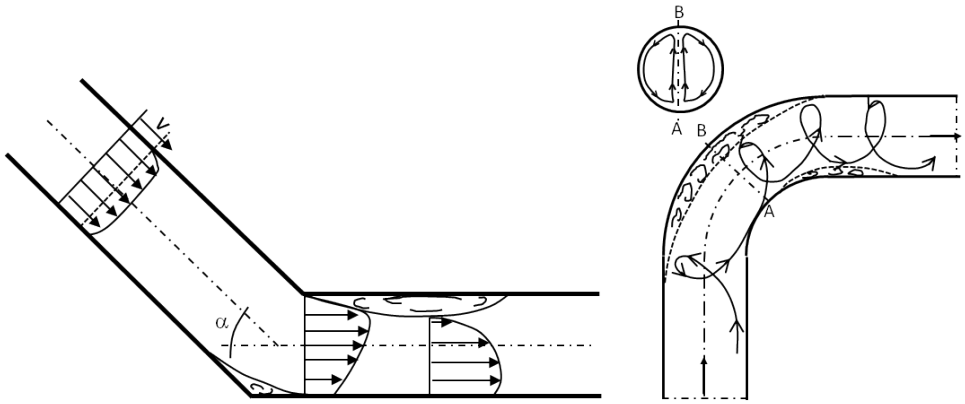

Figure 4.44: Schematic views of the bending and elbow and their effect on the fluid motion.

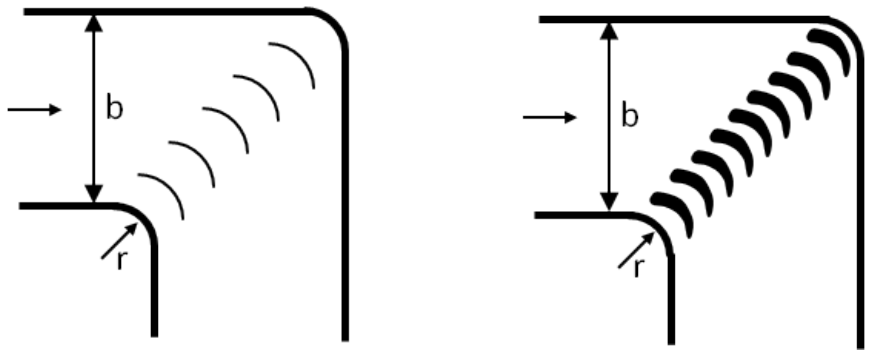

Figure 4.45: Possible fin configurations in the elbow.

largement, confluences and elbows) which together result in large pressure drop along the pipes. The T-junctions of the tree ducts, coming from the canopy hood, is a crucial point of energy loss. For reducing the energy dissipation the ducts should be inclined and the angle of connection was reduced (Figure 4.46). The efficiency was even higher if the velocity of the merging flows was equal.

The location of the enlargements in the main tube should be moved downstream from the confluences. Moreover, for less energy dissipation the width of the main tube should be enlarged corresponding to the confluencing pipes (Figure 4.46).

As a result, the pressure drop downstream the canopy hood's outlets is large (Figure 4.47).

Since the imposed power of the fan, to achieve the required volume discharge, is proportional to the primitive pressure drop the energy consumption of the secondary capture system is unnecessarily high.

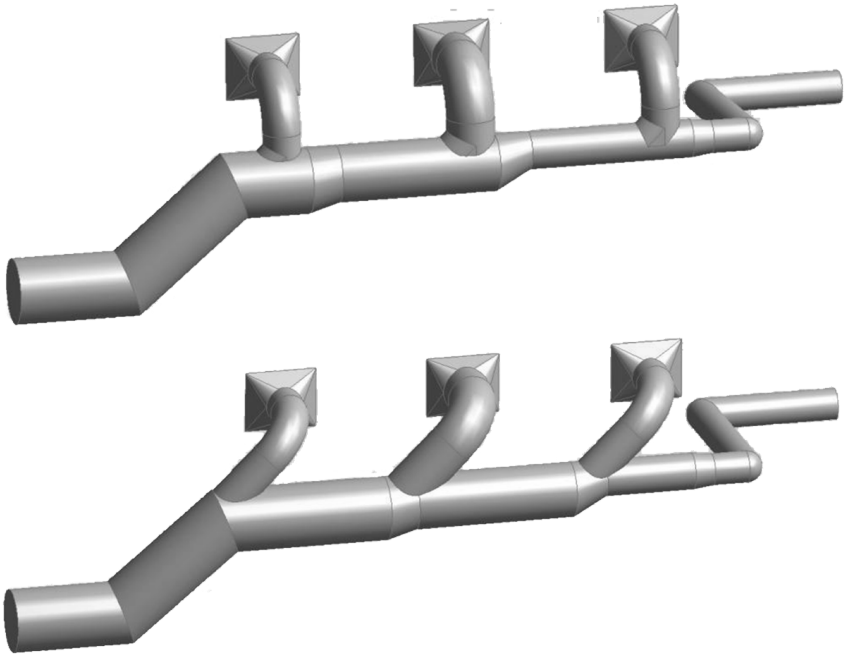

Figure 4.46: The original (upper) and the proposed (bottom) geometries of the tube connecting the canopy hood and the additional evacuation system to the fan.

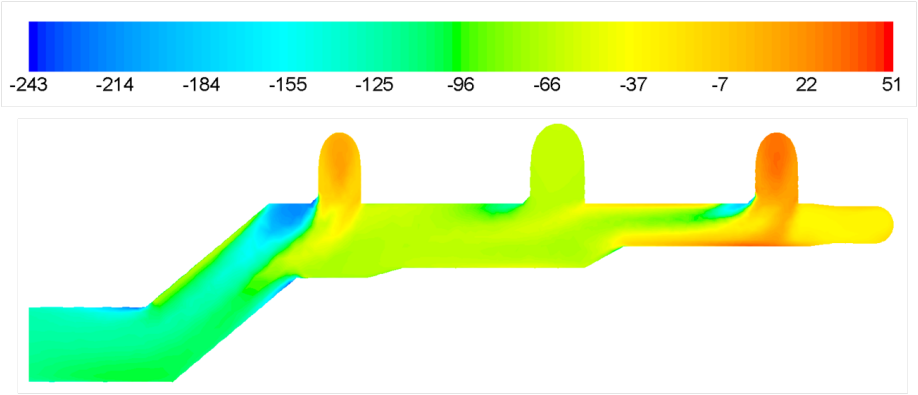

Figure 4.47: The total pressure $[Pa]$ distribution on the longitudinal cross section of the main tube.

Chapter 5

Conclusions

The requirements of steel production are often expected to increase during the life cycle of the factory; to treat the resulting increased fumes emissions, a sort of brute-force approach is followed by steelmaking practitioners, which is based on increasing both the fan power and the filter baghouse. This, in turn, has an impact on the size of the gap useful to merge ambient air with exhaust fumes; nowadays the gap size is chosen by trial and error. As a more efficient alternative, it is desirable to set up a CFD simulation model that is capable of capturing the essential thermal fluid dynamics features of fumes evacuation.

The main purpose of this work is to study the impact of the gap size on the fumes evacuation through the PCC. In spite of the great care lavished to obtain accurate (realistic) numerical simulations, the results presented in this study, strictly speaking, should still be appreciated from a qualitative point of view due to the lack of informations about the exact boundary conditions to be imposed. The present work focuses on exploring a variety of potentially feasible boundary conditions and on checking their impact on relevant variables, the final aim being to uncover a possible optimization of the whole evacuation process. Even though the present results are fairly linked to the

assumed boundary conditions and to the assumed PCC model geometry, yet we trust some conclusions can still be positively deduced. These are:
(i) the position of the reacting zone is at the very beginning of the PCC; as the opening coefficient reaches ζ exceeds 0.52, the conversion of hydrogen and carbon monoxide is complete;
(ii) there is not a unique value for the opening coefficient to optimize the process as a whole; rather the range $0.40 < \zeta < 0.52$ seems the most serviceable, depending on the relevant function of choice. The process of fumes evacuation needs an optimization analysis, which is beyond the reach of the present study;
(iii) the adopted PCC model geometry revealed a variety of inefficiencies; the most important improvement deals with the alignment of the two merging streams (the gap flow and the inlet flow), which allows for a remarkable 50 % reduction of the fan power;
(iv) although the 3D computational effort is huge, the potentiality of faster 2D simulation has been ascertained.

The aim of the secondary line's simulation was to predict the capturing and withdrawing efficiency of the canopy hood. The boundary conditions of the openings (doors and outlets) was imposed according to measured data and the boundary condition for representing the fire plume due to charging was based on literature data. The simulations of the secondary evacuation system and its conduits revealed that several parts call for modifications in order to decrease the primitive pressure drop and enhance the efficiency: the orientation of the deflection wall in the canopy hood, the low efficiency of the additional evacuation system and the enlargements, restriction and confluences in the conduits. All these weaknesses of the evacuation system's design leads to lower capturing ability.
The differences of the predicted temperature distribution and pressure field between steady-state and transient simulations were also shown and con-

cluded that, however, the temperature is over predicted using steady-state simulation, for practical engineering point of view the steady-state solver can provide sufficient information about the secondary evacuation system.

Bibliography

[1] Commission of the European Communities, European industry in a changing world - Updated sectorial overview, SEC(2009) 1111 final, Brussels, 2009.

[2] EC EAF, Technical Note on the Best Available Technologies to Reduce Emissions of Pollutants into the Air from Electric Arc Furnace Steel Production Plants, 1994.

[3] C. Prüm, C. Werner, J. Wirling, Reducing dioxin emissions in electric steel mills, MPT international, 1 (2005), 36–42.

[4] Eurofer, Compilation of open issues according to the Member state comments and the gaps of information on the review of the IS BREF draft, 2009.

[5] C. Ehrlich, G. Noll, W.-D. Kalkoff, G. Baumbach, A. Dreiseidler, PM10, PM2.5, PM1, Emissions from industrial plants - Results from measurement programmes in Germany, Atmospheric Environment, 41 (2007), 6236–6254.

[6] N. Perrin, C. Dworatzek, J. C. Vuillermoz, B. Daudin, S. D. Anderson, Continuous Fume Analysis at Vallourec Saint-Saulve, Electric Furnace Conference Proceedings, 49 (1991), 233–241.

[7] R. H. Perry, D. W. Green, J. O. Maloney, Perry's Chemical Engineers' Handbook, $7th$ edition, 1997, The McGraw-Hill Companies, Inc.

[8] A. J. Berthet, J-C. Grosjean, The 90s Electric Arc Furnace Steelmaking Route: The Leap Forward, Proceedings of the Sixth International Iron and Steel Congress, (1990), 180–189.

[9] C. Roederer, L. Gourtsoyannis Coordinated Study "Steel-Environment", European Commission, 1996.

[10] Eurofer, Review of the EAF chapter of the current BREF, Eurofer, 2007, 42.

[11] D. A. Surgeon, J. R. Tober, Maintenance of Secondary Electrical Power and Structural Systems for Electric Furnaces, Electric Furnace Conference Proceedings Warrendale: Iron and Steel Society, 53 (1995), 445–450.

[12] The Electric Arc Furnace −1990, Brussels, Belgium: International Iron and Steel Institute, (1990).

[13] G. Straffelini, A. Gabos, L. Labiscsak, D. Bodino, S. Adinolfi, F. Venturi, Coupled modelling of electric arc furnace and ladle furnace processes, Ironmaking and steelmaking 37 (2010), 181–186.

[14] C. Mapelli, S. Baragiola, Subscribed Content Evaluation of energy and exergy performances in EAF during melting and refining period, Ironmaking and steelmaking, 33 (2006), 379–388.

[15] R. J. Fruehan, The making, shaping and treating of steel, in: E.T. Turkdogan, R. J. Fruehan, Fundamentals of Iron and Steelmaking, Chapter 10, Electric Furnace Steelmaking, AISE Steel Foundation, Pittsburg PA, 1998, 132.

[16] J. H. Flux, Containment of melting shop roof emissions in electric arc furnace practice, Ironmaking and Steelmaking (Quarterly) 3 (1973), 121–133.

[17] J. G. Bekker, I. K. Craig, P. C. Pistorius, Modeling and Simulation of an Electric Arc Furnace Process, The Iron and Steel Institute of Japan International, 39 (1999), 23–32.

[18] M. Kirschen, V. Velikorodov, H. Pfeifer, Mathematical modelling of heat transfer in dedusting plants and comparison to off-gas measurements at electric arc furnaces, Energy, 31 (2006), 2926–2939.

[19] Ü. Camdali, M. Tunc, Steady State Heat Transfer of Ladle Furnace During Steel Production Process Journal of Iron and Steel Research, 13 (2006), 18–20.

[20] G. Bisio, G. Rubatto, R. Martini, Heat transfer, energy saving and pollution control in UHP electric-arc furnaces, Energy, 25 (2000), 1047–1066.

[21] Ü. Camdali, M. Tunc, F. Dikec, A thermodynamic analysis of a steel production step carried out in the ladle furnace, Applied Thermal Engineering, 21 (2001), 643–655.

[22] P. Gittler, R. Kickinger, S. Pirker, E. Fuhrmann, J. Lehner, J. Steins, Application of computational fluid dynamics in the development and improvement of steelmaking processes, Scandinavian Journal of Metallurgy, 29 (2000), 166–176.

[23] D. Mazudmar, J. W. Evans, Modelling of steelmaking processes, Boca Raton, FL, CRC Press., 2009.

[24] H. Laux, S. T. Johansen, H. Berg, O. S. Klevan, CFD analysis of the turbulent flow in ladles and the alloying process during tapping of steel furnaces, Scandinavian Journal of Metallurgy, 29 (2000), 71–80.

[25] S. Pirker, P. Gittler, H. Pirker, J. Lehner, CFD, a design tool for a new hot metal desulfurization technology, Applied Mathematical Modelling, 26 (2002), 337–350.

[26] S. T. Johansen, Multiphase flow modeling of metallurgical flows, Experimental Thermal and Fluid Science, 26 (2002), 739–745.

[27] A. Kharicha, A. Ludwig, M. Wu, Shape and stability of the slag/melt interface in a small dc ESR process, Materials Science and Engineering A, 413-414 (2005), 129–134.

[28] K. Chattopadhyay, M. Isac, R. I. L. Guthrie, Applications of Computational Fluid Dynamics (CFD) in iron- and steelmaking: Part 1, Ironmaking and Steelmaking, 37 (2010), 554–561.

[29] K. Chattopadhyay, M. Isac, R. I. L. Guthrie, Applications of Computational Fluid Dynamics (CFD) in iron- and steelmaking: Part 2, Ironmaking and Steelmaking, 37 (2010), 562–569.

[30] Q. Hou, Z. Zou, Comparison between Standard and Renormalization Group κ-ε Models in Numerical Simulation of Swirling Flow Tundish, ISIJ International 45 (2005), 325–330.

[31] A. Marcandalli, C. Mapelli, W. Nicodemi, A thermomechanical model for simulation of carbon steel solidification in mould in continuous casting, Ironmaking and Steelmaking, 30 (2003), 265–272.

[32] C. Mapelli, S. Semplici, Design of corners of mould in square billet casting, Ironmaking and Steelmaking, 30 (2003), 503–510.

[33] Y. Li, R. J. Fruehan, Computational Fluid-Dynamics Simulation of Postcombustion in the Electric-Arc Furnace, Metallurgical and Materials Transactions B, 34B (2003), 333–343.

[34] E. Chan, M. Riley, M. J. Thomson, E. J. Evenson, Nitrogen Oxides (NO_x) Formation and Control in an Electric Arc Furnace (EAF): Analysis with Measurements and Computational Fluid Dynamics (CFD) Modeling, ISIJ International 44 (2004), 429–438.

[35] L. F. Richardson, The approximate arithmetical solution by finite differences of physical problems involving differential equations, with an application to the stresses in a masonry dam., Philosophical Transactions of the Royal Society of London, Series A, 210 (1910), 307–357.

[36] R. Courant, K. Friedrichs, H. Lewy, Die partiellen differenzengleichungen der mathematischen Physik, Mathematische Annalen (Historical Archive), 100 (1928), 32–74.

[37] T. Steinhaus, S. Welch, R. Carvel, J. L. Torero, Large-Scale pool fires, Thermal Science Journal, 11 (2007), 101–118.

[38] N. L. Crauford, S. K. Liew, J. B. Moss, Experiemntal and numerical simulation of a buoyant fire, Combustion and Flame, 61 (1985), 63–77.

[39] K. C. Adiga, D. E. Ramaker, P. A. Tatem, F. W. Williams, Modeling pool-like gas flames of propane, Fire Safety Journal, 14 (1989), 241–251.

[40] F. Tamanini, Reaction rates, air entrainment and radiation in turbulent fire plumes, Combustion and Flame, 30 (1977), 85–101.

[41] H. J. You, G. M. Faeth, Turbulent combustion: buoyant axi-symmetric turbulent diffusion flames in still air, Combustion and Flame, 44 (1982), 261–275.

[42] M. S. Hossain, M. Rodi, A turbulence model for buoyant flows and its application to vertical buoyant jets, Turbulent jets & flames, New York: Pergamon Press, (1982), 121–178.

[43] S. Nam, R. G. Bill, Numerical simulation of thermal plumes, Journal Fire Safety, 21 (1993), 231–256.

[44] Y. Wang, P. Chatterjee, J. L. Ris, Large eddy simulation of fire plumes, Proceedings of the Combustion Institute, 33 (2011), 2473–2480.

[45] B.J. McCaffrey, Purely Buoyant Diffusion Flames: Some Experimental Results, NBSIR 79-1910, NIST, 1979.

[46] N. Stockwell, C. Zhang, T. Ishii, Y. Hino Numerical Simulations of Turbulent Non-premixed Combustion in a Regenerative Furnace, ISIJ International, 41 (2001), 1272–1281.

[47] N. Peters, Turbulent combustion, UK: Cambridge University Press, 2000.

[48] W. P. Jones, J. H. Whitelaw, Calculation methods for reacting turbulent flows: a review, Combustion and Flame, 48 (1982), 1–26.

[49] K. N. C. Bray, N. Peters, Laminar flamelets in turbulent flames, Turbulent reacting flows, New York: Academic Press, (1994), 63–113.

[50] B. F. Magnussen, B. H. Hjertager, On mathematical models of turbulent combustion with special emphasis on soot formation and combustion, International 16th Symposium on Combustion, The Combustion Institute, 1976.

[51] I. R. Gran, B. F. Magnussen, A numerical study of a bluff-body stabilized diffusion flame. Part 2. Influence of combustion modeling and finite-rate chemistry, Combustion Science and Technology, 119 (1996), 191–217.

[52] B. Chakraborty, P. J. Paul, H. S. Mukunda, valuation of combustion models for high speed H_2/air confined mixing layer using DNS data, Combustion and Flame, 121 (2000), 195–209.

[53] X. Han, X. Wei, U. Schnell, K. R. G. Hein, Detailed modeling of hybrid reburn/SNCR processes for NO_x reduction in coal-fired furnaces, Combustion and Flame, 132 (2003), 374–386.

[54] E. Giacomazzi, V. Battaglia, C. Bruno, The coupling of turbulence and chemistry in a premixed bluff-body flame as studied by LES, Combustion and Flame, 138 (2004), 320–335.

[55] S. G. Stefanidis, B. Merci, G. J. Heynderickx, G. B. Marin, CFD simulations of steam cracking furnaces using detailed combustion mechanisms, Computers and Chemical Engineering, 30 (2006), 635–649.

[56] A. Frassoldati, T. Faravelli, E. Ranzi, The ignition, combustion and flame structure of carbon monoxide/hydrogen mixtures. Note 1: Detailed kinetic modeling of syngas combustion also in presence of nitrogen compounds, International Journal of Hydrogen Energy, 32 (2007), 3471–3485.

[57] A. Cuoci, A. Frassoldati, G. Buzzi Ferraris, T. Faravelli, E. Ranzi, The ignition, combustion and flame structure of carbon monoxide/hydrogen mixtures. Note 2: Fluid dynamics and kinetic aspects of syngas combustion, International Journal of Hydrogen Energy, 32 (2007), 3486–3500.

[58] S. G. Davis, A. V. Joshi, H. Wang, F. Egolfopoulos, An optimized kinetic model of H_2/CO combustion, Proceedings of the Combustion Institute, 30 (2005), 1283–1292.

[59] Q. Reynolds, Thermal radiation modelling of DC smelting furnace freeboards, Minerals Engineering, 15 (2002), 993–1000.

[60] M. Ilbas, The effect of thermal radiation and radiation models on hydrogenhydrocarbon combustion modelling, International Journal of Hydrogen Energy, 30 (2005), 1113–1126.

[61] A. Habibi, B. Merci, G. J. Heynderickx, Impact of radiation models in CFD simulations of steam cracking furnaces, Computers and Chemical Engineering, 31 (2007), 1389–1406.

[62] S. Chandrasekhar, Radiative transfer, London: Oxford University Press, 1950.

[63] S. Rosseland, Theoretical astrophysics, Clarendon, London and New York: Oxford Univ. Press. 1936.

[64] R.Siegel, J. R. Howell, Thermal Radiation Heat Transfer, Hemisphere Publishing Corporation, Washington D. C., 1992.

[65] G. Krishnamoorthy, A new weighted-sum-of-gray-gases model for $CO_2 - H_2O$ gas mixtures, International Communications in Heat and Mass Transfer, 37 (2010), 1182–1186.

[66] M. Y. Kim, A heat transfer model for the analysis of transient heating of the slab in a direct-fired walking beam type reheating furnace, International Journal of Heat and Mass Transfer, 50 (2007), 3740–3748.

[67] J.C. Hewson, A.R. Kerstein, Stochastic simulation of transport and chemical kinetics in turbulent CO/H2/N2 flames, Combust Theory Modell, 5 (2001), 669–897.

[68] FLUENT User's Guide, Version 6.3, Fluent Inc., Centerra Resource Park, 10 Cavendish Court, Lebanon, NH 03766.

[69] B. F. Magnussen 19th AIAA aerospace science meeting, St. Louis, Missouri, (1981).

[70] R.G. Gilbert, K. Luther, J. Troe, Ber. Bunsenges, Phys. Chem., 87 (1983).

[71] T. Hara, S. Kato, Numerical simulation of thermal plumes in free space using the standard κ-ε model, Fire Safety Journal, 39 (2004), 105–129.

[72] A. Tewarson, Smoke Point Height and Fire Properties of Materials, National Institute of Standards and Technology, National Technical Information Service Springfield, VA 22161, USA 1988.

[73] I. B. Celik, U. Ghia, P. J. Roache, C. J. Freitas, H. Coleman, P. E. Raad, Procedure for Estimation and Reporting of Uncertainty Due to Discretization in CFD Applications, American Society of Mechanical Engineers Journal of Fluids Engineering, 130 (2008), 1–4.

[74] I. B. Celik, O. Karatekin, Numerical Experiments on Application of Richardson Extrapolation With Nonuniform Grids, American Society of Mechanical Engineers Journal of Fluids Engineering, 119 (1997), 584–590.

[75] J. H. Ferziger, M. Peric, Further discussion of numerical errors in CFD, International Journal of Numerical Methods Fluids, 23 (1996), 1263–1274.

[76] F. Trivellato, On the efficiency of turbulent mixing in rotating stirrers, Chemical Engineering and Processing, 50 (2011), 799–809.

[77] R. W. Bilger, Turbulent flows with nonpremixed reactants. Turbulent Reacting Flows, Eds., P. Libby and F. Williams, 44 (1980), 65–113.

[78] R. Hilbert, F. Tap, H. El-Rabii, D. Thévenin, Impact of detailed chemistry and transport models on turbulent combustion simulations, Progress in Energy and Combustion Science, 30 (2004), 61–117.

Appendix A

Appendix

Table A.1: Reaction rate constants are given for the form $k = A \cdot T^n \cdot e^{(-E_a/(RT))}$.

	Reaction	A [mol/1/s/K]	n	E_a [cal/mol]
1	$H + O_2 = OH + O$	$2.21 \cdot 10^{11}$	0	16650
2	$O + H_2 = OH + H$	$4.33 \cdot 10^{10}$	0	10000
3	$H + O_2 + [M] = HO_2 + [M]$	$4.65 \cdot 10^{9}$	-0.8	0
Low-pressure limit:		$7.00 \cdot 10^{11}$	0.4	0
Troe parameters: 0.5, 10^{-30}, 10^{30}, -1				
Third-body efficiencies: H_2O = 18.0, H_2 = 2.5, N_2 = 1.26, O_2 = 0.0, CO = 1.2, CO_2 = 2.4				
4	$H + O_2 + O_2 = HO_2 + O_2$	$8.90 \cdot 10^{08}$	0	-2822
5	$OH + HO_2 = H_2O + O_2$	$5.00 \cdot 10^{10}$	0	1000
6	$H + HO_2 = OH + OH$	$3.25 \cdot 10^{10}$	0	0
7	$O + HO_2 = O_2 + OH$	$3.25 \cdot 10^{10}$	0	0
8	$OH + OH = O + H_2O$	$7.36 \cdot 10^{09}$	0	1100
9	$H_2 + [M] = H + H + [M]$	$2.23 \cdot 10^{11}$	0	96081
Third-body efficiencies: $H_2O = 12.0, H_2 = 2.5, CO = 1.9, CO_2 = 3.8$				
10	$O_2 + [M] = O + O + [M]$	$1.55 \cdot 10^{11}$	0	115120
Third-body efficiencies: $H_2O = 12.0, H_2 = 2.5, CO = 1.9, CO_2 = 3.8$				
11	$H + OH + [M] = H_2O + [M]$	$4.50 \cdot 10^{16}$	-2	0
Third-body efficiencies: $H_2O = 16.0, H_2 = 2.0, CO_2 = 1.9$				
12	$H + HO_2 = H_2 + O_2$	$2.50 \cdot 10^{10}$	0	700
13	$HO_2 + HO_2 = H_2O_2 + O_2$	$2.11 \cdot 10^{09}$	0	0
14	$OH + OH + [M] = H_2O_2 + [M]$	$7.40 \cdot 10^{10}$	-0.37	0
Low-pressure limit:		$2.30 \cdot 10^{12}$	-0.9	-1700
Troe parameters: $0.7346, 94.00, 1756, 5182$				
Third-body efficiencies: $H_2O = 6.0, H_2 = 2.0, CO = 1.5, CO_2 = 2.0$				

15	$O + OH + [M] = HO_2 + [M]$	$1.00 \cdot 10^{10}$	0	0
Third-body efficiencies: $H_2O = 1.0, H_2 = 1.0, N_2 = 1.0, O_2 = 0.0,$ $CO = 1.0, CO_2 = 1.0$				
16	$O_2 + CO = CO_2 + O$	$2.53 \cdot 10^{9}$	0	47700
17	$O_2 + HCO = HO_2 + CO$	$1.00 \cdot 10^{12}$	0	0
18	$CO + O + [M] = CO2 + [M]$	$9.64 \cdot 10^{11}$	0	3800
Low-pressure limit:		$2.07 \cdot 10^{20}$	-3.34	7610
Troe parameters: $1, 1, 1, 1$				
Third-body efficiencies: $H_2O = 12.0, H_2 = 2.0, CO = 1.5, CO_2 = 2.0$				
19	$CO + OH = CO_2 + H$	$9.60 \cdot 10^{08}$	0.14	7352
		$7.32 \cdot 10^{07}$	0.03	-16
20	$CO + HO_2 = CO_2 + OH$	$3.01 \cdot 10^{10}$	0	23000
21	$CO + H_2O = CO_2 + H_2$	$2.00 \cdot 10^{08}$	0	38000
22	$HCO + [M] = CO + H + [M]$	$1.20 \cdot 10^{14}$	-1	17000
Third-body efficiencies: $H_2O = 5.0, H_2 = 1.9, CO = 1.5, CO_2 = 3.0$				
23	$HCO + O = CO_2 + H$	$3.00 \cdot 10^{10}$	0	0
24	$HCO + H = H_2 + CO$	$1.00 \cdot 10^{11}$	0	0
25	$HCO + OH = H_2O + CO$	$5.00 \cdot 10^{10}$	0	0
26	$HCO + HO_2 = H_2O_2 + CO$	$4.00 \cdot 10^{08}$	0	0
27	$HCO + HO2 \rightarrow H + OH + CO2$	$3.00 \cdot 10^{10}$	0	0
28	$H + H_2O = H_2 + OH$	$4.00 \cdot 10^{07}$	1	19000
29	$H_2O_2 + H = H_2O + OH$	$2.41 \cdot 10^{10}$	0	3970
30	$H_2O_2 + H = H_2 + HO_2$	$6.03 \cdot 10^{10}$	0	7950
31	$H + H_2 \rightarrow H_2 + H$	$3.369 \cdot 10^{04}$	2.0	7658.60
32	$OH + H_2O \rightarrow H_2O + OH$	$3.994 \cdot 10^{03}$	2.0	2223.39
33	$HO_2 + H_2O \rightarrow H_2O_2 + OH$	$5.388 \cdot 10^{03}$	2.0	28780.05
34	$OH + H_2O_2 \rightarrow H_2O + HO_2$	$3.195 \cdot 10^{06}$	2.0	-4169.95
35	$O + H2O2 \rightarrow OH + HO2$	$1.083 \cdot 10^{03}$	2.0	-1657.32
36	$HO_2 + H_2O_2 \rightarrow H_2O_2 + HO_2$	$4.310 \cdot 10^{01}$	2.0	5529.49

Table A.2: Thermodynamical data of the considered species in the detailed reaction mechanism. The units are $cal/(molK)$ for S and c_p and $kcal/mol$ for ΔH_f.

Species	ΔH_f	S	$c_p\,(300\,K)$	$c_p\,(1000\,K)$	$c_p\,(2000\,K)$
N_2	0	45.816	6.949	7.830	8.601
H_2	0	31.256	6.902	7.209	8.183
O_2	0	49.050	7.010	8.350	9.032
H_2O	−57.800	45.154	7.999	9.875	12.224
H_2O_2	−32.530	55.725	10.416	15.213	17.878
OH	8.910	43.978	6.947	7.341	8.213
H	52.099	27.422	4.968	4.968	4.968
O	59.560	38.500	5.232	4.999	4.976
HO_2	3.000	54.809	8.349	11.380	13.321
CO	−26.420	−26.406	47.259	6.950	7.948
CO_2	−94.061	−94.010	51.140	8.910	12.993
HCO	10.401	10.395	53.716	8.245	11.521